

# University of St Andrews



Full metadata for this thesis is available in  
St Andrews Research Repository  
at:

<http://research-repository.st-andrews.ac.uk/>

This thesis is protected by original copyright

INFRARED CHARACTERISATION OF  
SEMICONDUCTORS

Antony M. Thorley



TR A1121

To Carron

I would like to thank Professor Stradling, the staff of St. Andrews University and the employees of Hughes Microelectronics Limited for all their assistance.

Declaration

I Antony M Thorley hereby certify that this thesis has been composed by myself, that it is a record of my own work, and that it has not been accepted in partial or complete fulfilment of any other degree of professional qualification.

.....

signature

.....

date

I was admitted to the Faculty Science of the University of St. Andrews under Ordinance General N<sup>o</sup>. 12 in October 1981 and as a candidate for the Degree of Ph.D. in October 1981.

.....

signature

.....

date

I hereby certify that the candidate has fulfilled the conditions of the Resolution and Regulations appropriate to the Degree of Ph.D.

.....

supervisors signature

.....

date

### Copyright

In submitting this thesis to the University of St. Andrews I understand that I am giving permission for it to be made available for use in accordance with the regulations of the University Library for the time being in force, subject to any copyright vested in the work not being affected thereby. I also understand that the title and abstract will be published, and that a copy of the work may be made and supplied to any bona fide library or research worker.

This work was funded under a Science and Engineering Research Council Combined Award in Science and Engineering. The participating company was Hughes Microelectronics Limited, Glenrothes, Fife and my industrial supervisor was Jim West.

## ABSTRACT

A theoretical and experimental investigation of the optical properties of ion-implanted silicon over the wavelength range  $2\ \mu\text{m}$  to  $3\ \text{cm}$  has been performed. Twelve samples were supplied by Hughes Microelectronics Ltd. and a further two from Plessey Research Caswell. In the near infrared (short wavelength region) plasma edge features are seen for implants of  $10^{15}\text{ions} / \text{cm}^2$  and above. The feature shape is sensitive to the donor implant distribution and this allows contactless characterisation through the use of a computer model developed in chapters 1 and 2. In the far infrared interference fringes are seen with modulation close to theory and the total transmission is sensitive to implant dose. Millimeter quasi optical results are in close agreement with the theory. The near infrared is limited to doses of  $10^{15}\text{ions} / \text{cm}^2$  and above for implant distribution measurements, whilst at centimeter wavelengths a 4 x difference between the transmission at  $10^{15}\text{ions} / \text{cm}^2$  and zero dose should allow an implant as low as  $2 \times 10^{14}\text{ions} / \text{cm}^2$  to be identified. At centimeter wavelengths the absolute fit between theory and experiment is not as good as in the millimeter and shorter wavelengths due to standing waves in the experimental arrangement. The possibility exists for tuning out these reflections with matching stubs and, with appropriate modeling, achieving even higher sensitivity in transmission to implant doses below  $2 \times 10^{14}\text{ions} / \text{cm}^2$ .

Level crossing effects in Zeeman split donor states in GaAs were investigated. No conclusive evidence for these was found within the limits of sensitivity of the experiments indicating that any amplitude is below 10% of the main transition intensity.

## CONTENTS

Figures	1
Introduction	4
Ion-implantation	
Chapter 1	
Previous Work and Background	
Introduction	6
Previous Work	6
Summary	11
The Focus of this Thesis	12
Background	13
Damage and Annealing	13
Solubility	14
Mobility vs. Carrier Concentration	14
Chapter 2	
Reflectivity Theory	
Introduction	15
Thin Film Reflectivity	15
Free Electron Model	21
Electron Mobility	24
Electron Effective Mass	25
Chapter 3	
Computer Programme Predictions	26
Chapter 4	
Experimental Techniques	
2 $\mu\text{m}$ to 8 $\mu\text{m}$	33
Calibration	34
Sample Preparation	34
Further Near Infrared Experiments	37
12.5 $\mu\text{m}$ to 1 mm Techniques	37
Discrete Far-infrared Measurements	39
Millimeter Wave Measurements	40
Centimeter Wave Measurements	40
Sheet Resistivity	41

## CONTENTS

### Chapter 5

#### Experimental Results

2 $\mu\text{m}$ to 8 $\mu\text{m}$ Results	42
Results for Arsenic Implanted Silicon from Plessey	45
12.5 $\mu\text{m}$ to 1 mm Results	46
Discrete Far-Infrared Measurement Results	50
Millimeter Wave Results	52
Centimeter Wave Results	53
Sheet Resistivity Results	55

### Chapter 6

#### Discussion and Conclusions

Optimisation errors	56
Discussion	59
Conclusions	63
Further Work	64

## FIGURES

### CHAPTER 2

Figure 1 - Implant concentration vs depth

Figure 2 - Simple boundary

Figure 3 - Single film on an infinite substrate

Figure 4 - Two films on an infinite substrate

Figure 5 - An assembly of n films on an infinite substrate

Figure 6 - Reflectivity vs wavelength a)  $w_p = 3 \mu m$ ,  $\tau = 1,6 \times 10^{-13}$  secs

b)  $w_p = 3 \mu m$ ,  $\tau = 1,6 \times 10^{-14}$  secs

c)  $w_p = 3 \mu m$ ,  $\tau = 4,8 \times 10^{-15}$  secs

d)  $w_p = 3 \mu m$ ,  $\tau = 1,6 \times 10^{-15}$  secs

Figure 7 Electron mobility vs concentration

### CHAPTER 3

Figure 8 - Computer predictions reflectivity vs angle

Figure 9 - Computer predictions reflectivity vs implant concentration

Figure 10 - Computer predictions reflectivity vs scattering time

Figure 11 - Computer predictions reflectivity vs implant depth

Figure 12 - Computer predictions reflectivity vs implant mean

Figure 13 - Computer predictions reflectivity vs implant spread

Figure 14 - Computer predictions reflectivity vs implant conc 1-10  $\mu m$

Figure 15 - Computer predictions transmission vs implant conc 1-10  $\mu m$

Figure 16 - Computer predictions absorption vs implant conc 1-10  $\mu m$

Figure 17 - Computer predictions reflectivity vs implant conc 100-10  $cm^{-1}$

Figure 18 - Computer predictions transmission vs implant conc 100-10  $cm^{-1}$

Figure 19 - Computer predictions absorption vs implant conc 100-10  $cm^{-1}$

Figure 20 - Computer predictions reflectivity vs implant conc 10-1,0  $cm^{-1}$

Figure 21 - Computer predictions transmission vs implant conc 10-1,0  $cm^{-1}$

Figure 22 - Computer predictions absorption vs implant conc 10-1,0  $cm^{-1}$

Figure 23 - Computer predictions reflectivity vs implant conc 1,0-0,1  $cm^{-1}$

Figure 24 - Computer predictions transmission vs implant conc 1,0-0,1  $cm^{-1}$

Figure 25 - Computer predictions absorption vs implant conc 1,0-0,1  $cm^{-1}$

Figure 26 - Computer predictions reflectivity vs implant conc 0,1-0,01  $cm^{-1}$

Figure 27 - Computer predictions transmission vs implant conc 0,1-0,01  $cm^{-1}$

Figure 28 - Computer predictions absorption vs implant conc 0,1-0,01  $cm^{-1}$

## FIGURES

### CHAPTER 4

Figure 29 - Grating spectrometer experimental setup

Figure 30 - Grating spectrometer calibration curves

Figure 31 - FIR spectrometer experimental setup

Figure 32 - FIR Laser experimental setup

Figure 33 - mm wave experimental setup

Figure 34 - cm wave experimental setup

### CHAPTER 5

Figure 35 - Grating spectrometer results sheet 11

Figure 36 - Grating spectrometer results sheet 12

Figure 37 - Grating spectrometer ratioed results cr23 to cr26

Figure 38 - Grating spectrometer a) average + theory  $10^{15}$

b) average + theory  $3 \times 10^{15}$

c) average + theory  $5 \times 10^{15}$

Figure 39 - Grating spectrometer a) average + theory  $10^{16}$

b) average + theory  $7.5 \times 10^{15}$

Figure 40 - Grating spectrometer ion-concentration vs depth

Figure 41 - Grating spectrometer good fit to  $10^{16}$  with cutoff

Figure 42 - Arsenic implant average + theory MS061/TP4

Figure 43 - Arsenic implant average + theory MS038/1

Figure 44 - Arsenic implant ion-concentration vs depth a) MS061/TP4 b) MS038/1

Figure 45 - Arsenic implant ion-concentration vs depth actual & theory

Figure 46 - FIR spectrometer results a) background transmission

b) un-implanted silicon trans.

c) ratio of a) and b)

Figure 47 - FIR Laser results typical sheet

Figure 48 - mm wave experimental results typical sheet

### CHAPTER 6

Figure 49 - Reflectivity vs. implant distribution a)  $10^{16}$  b)  $5 \times 10^{15}$

c)  $3 \times 10^{15}$  d)  $10^{15}$

Figure 50 - Implant distributions for figure 49

## FIGURES

Figure 51 - a) Reflectivity vs. 'cutoff' concentration b) Concentration vs. depth

Figure 52 - Plessey sample reflectivities vs distribution a) MS061/TP4

b) MS038/1

c) and d) electron concentrations vs. depth for a) and b)

### CHAPTER 7

Figure 53 - Aldrich-Greene curves relative to 1s level

Figure 54 - Zinc - Blend structure

Figure 55 - GaAs band diagram

Figure 56 - First Brillouin zone for GaAs

Figure 57 - Hydrogenic wavefunction amplitude vs. radius 1s, 2s & 2p

Figure 58 - Simple energy level diagram of central cell splitting

Figure 59 - RR98B showing central cell splitting

Figure 60 - Landau splitting of the conduction and valence bands

Figure 61 - Sample arrangement for photoconductivity

Figure 62 - Faraday orientation (Electron orbits normal to e/m radiation)

Figure 63 - Voigt orientation (Electron orbits parallel to e/m radiation)

### CHAPTER 8

Figure 64 - Level crossings equipment layout

Figure 65 - R-137 0 Tesla run 402

Figure 66 - Typical R-137 spectra run 540

Figure 67 - a) Po/P- 1 + 1.6 Tesla runs 533 + 540

b) Po/P- 1.3 + 2 Tesla runs 563 + 570

Figure 68 - P+/P- 1 + 2 Tesla 1.0 + 1.6 & 1.3 + 2.0 runs 533 + 540 & 563 + 570

Figure 69 - R-137 1s + 2p<sub>+</sub> a) @ 1.5 Tesla to show the effects of

b) @ 1.6 Tesla sampling on peak height.

Figure 70 - Typical R-137 spectra with reduced 1s + 2p<sub>+</sub> run 563

Figure 71 - Typical RR98B spectra at 2.0 Tesla run 844

Figure 72 - RR98B 0 Tesla run 846

Figure 73 - Typical Stillman No.1 spectra run 1064 at 2.0 Tesla

Figure 74 - Bolometer spectrum 20 + 80 cm<sup>-1</sup> with overlaid sine wave

## INTRODUCTION

### INTRODUCTION

Ion-implantation has numerous advantages over diffusion for semiconductor doping:

- i) Accurate control of the ion-beam current, duration and energy allows a precisely known impurity concentration to be implanted to a known depth.
- ii) Multiple implants and the channeling of ions parallel to substrate atomic planes allows the implant profile with depth to be controlled as well.
- iii) The impurity does not have to be soluble in the substrate and solubility limits can be exceeded.
- iv) The implant process is very pure, an ion-implanter incorporates a mass spectrometer to single out the implant ion and reject all others.
- v) Scanning the ion-beam across a substrate allows large areas to be uniformly and reproducibly implanted.
- vi) Ion-implantation takes place at low temperatures  $< 200^{\circ}\text{C}$  this reduces processing problems and allows more convenient masks to be used for device fabrication e.g. Aluminium or photoresist.
- vii) Ion-implantation can be used through a capping layer.
- viii) The implanted impurities at the mask edge show far less ( $\approx 100x$  less) sideways distribution. This is negated to some extent by the subsequent annealing.

All these advantages make ion-implantation attractive to the semiconductor industry as an accurate, reproducible and versatile doping technique.

Analysis of ion-implanted wafers is currently carried out by progressively removing the wafer surface and probing the new surface's electrical characteristics or by secondary

## INTRODUCTION

ion mass spectrometry (SIMS) analyses. These are destructive and expensive ( $\approx$  £1000 per wafer) or time consuming.

The main work presented in this thesis involves the use of optical techniques to contactlessly and non-destructively probe the ion-implanted surface of a semiconductor to provide the same information as the destructive technique only more cheaply and, potentially, more rapidly.

The second section, chapters 4 and 5, of the work presented, covers the application of photoconductive methods to the analysis of level crossings in GaAs.

At 4.2 K the majority of electrons from shallow donors in GaAs are 'frozen' into the ground state energy level around the donor impurities. Incident optical radiation of the correct frequency excites these electrons into higher energy levels. Under the application of a magnetic field these are Zeeman split. Calculations by Aldrich and Green [31] show that, at certain magnetic fields, different inter-state transitions have the same energy, and the possibility exists of these two states interacting. Investigation of the photoconductive intensities for observable transitions could provide the opportunity to view forbidden transitions and thus corroborate the theoretical calculations.

## CHAPTER 1

### PREVIOUS WORK

#### Introduction

The following section reviews some of the work, published over a thirty year period, on the use of infrared reflectivity as a means to probe and characterise doped semiconductors. The summary highlights the trends and some of the obstacles as well as explaining the aims of this thesis in comparison with the work that has already been carried out.

#### Previous work

In 1957 Spitzer and Fan [1] published a paper in which the reflectivity of bulk n and p doped silicon, germanium and indium antimonide as well as n-type gallium arsenide was compared to theoretical plots. The experiments were carried out in the 5  $\mu\text{m}$  to 35  $\mu\text{m}$  region. The comparison enabled the carrier effective mass to be determined and this was compared with values obtained using other methods. Agreement was found for n- and p-type silicon, n-type germanium and p-type indium antimonide. The samples consisted of bulk doped crystals polished on both sides to allow accurate reflectivity and transmission results to be obtained.

Edwards and Maker [2] in 1962 used infrared reflectivity to plot carrier concentration inhomogeneity in wafers of indium arsenide. The carrier concentration only varied by a few percent over the wafer and thus  $m^*$  and  $\tau$  (the effective mass and the scattering time) could be taken as constant. The change in the carrier concentration showed up as a change in the wavelength of the plasma reflectivity minimum. Their work used single crystal samples. The technique provided a non-destructive and rapid way of analysing the wafer uniformity.

## CHAPTER 1

Howarth and Gilbert [3] in 1962 following the method of Spitzer and Fan [1] studied a range of bulk doped silicon samples in order to establish the variation in effective mass with carrier concentration. This paper is discussed in detail in chapter two page 25

Murray, Rivera and Hoss [4] in 1965 used polished bulk samples of p-doped gallium arsenide and looked at the differential change of reflectivity with frequency. They found that the classical Drude model explained the experimentally observed shift in reflectivity minimum vs. carrier concentration. Intervalence band transitions and the reststrahlen played no part in the wavelength range they investigated, 3  $\mu\text{m}$  to 12  $\mu\text{m}$ .

Gardener, Kappallo and Gordon [5] in 1966 compared infrared reflectivities of doped silicon samples with samples of known impurity concentrations. They could then determine non-destructively the surface concentrations ranging from  $5 \times 10^{19} \text{ cm}^{-3}$  to  $5 \times 10^{20} \text{ cm}^{-3}$ . In these experiments the main source of error was in locating the plasma minima. The samples in this study were prepared by diffusion.

Subashiev and Kukharskii [6] in 1967 theoretically analysed the reflectivity of a semiconductor where the dielectric constant was assumed to vary arbitrarily with depth. They concluded that a comparison between experiment and theory would make it possible to determine the surface carrier concentration, the carrier mobility and the rate of change of carrier concentration with depth in the surface region.

Schumann [7] in 1970 gathered together the data on plasma minima vs. doping concentration in bulk samples for various semiconductors including silicon. These results show that the

## CHAPTER 1

wavelength of minimum reflectivity gives a reliable guide to the bulk impurity concentration.

Palik, Holm and Gibson [8] in 1977 looked at thin, doped films on gallium arsenide substrates. The films were grown either by liquid phase epitaxy, vapour phase epitaxy or by molecular beam epitaxy. The reflectivity measurements were backed up by capacitance-voltage, van der Pauw, Hall and resistivity measurements to determine the film carrier concentration and mobility. Cleave and stain techniques were used to measure the film thicknesses. A multilayer approach was used to mathematically analyse the results. Spectra were taken of both surfaces of the doped samples. Both the film and substrate had to be polished. Data from each of the techniques was compared. Infrared results were taken from 8  $\mu\text{m}$  to 50  $\mu\text{m}$ . No fits were made at the longer wavelengths because of interference effects. Problems with non-uniformities in film thickness and the limited penetration depth for high dopant concentration were given for any discrepancies between the reflectivity results and other measurements. The paper shows calculations which show that for reasonable accuracy at a film thickness of 0.3  $\mu\text{m}$  the carrier concentration had to be at least  $3 \times 10^{16}$  electrons/ $\text{cm}^3$ .

Wagner and Schaefer [9] in 1978 looked at thermally annealed arsenic implanted silicon. The implant doses were between  $3 \times 10^{14}$  ions/ $\text{cm}^2$  and  $2 \times 10^{16}$  ions/ $\text{cm}^2$  at an energy of 50 KeV. The samples were polished on both sides. Transmittance was used to look at the total dose while reflectance was used for the surface concentration. A multilayer model was employed and matched to the experimental data. The implanted ions distribution was derived as a function of depth. Extended annealing reduced the surface concentration, as the implant diffused into the substrate, with a consequent shift in the plasma minimum. The results were in close agreement with conventional measuring techniques

## CHAPTER 1

for dose, surface concentration and sheet resistivity. Accurate fits were limited to doses greater than  $10^{15}$  ions/cm<sup>2</sup>. Below this concentration the reflectivity data became too featureless to fit accurately.

Palik and Holm [10] in 1979 produced a comprehensive review of semiconductor optical characterisation. In section B of the review, reflection scanning at the plasma edge uses free carrier absorption to give an x-y plot of wafer carrier density. For wafers with lower carrier densities, less than  $3 \times 10^{18}$  cm<sup>-3</sup>, the scanning wavelength needs to be greater than 15  $\mu$ m. The spot size is limited by diffraction and therefore the spatial resolution of carrier inhomogeneities is reduced at the longer wavelengths.

Engstrom [11] in 1980 studied boron implanted and laser annealed silicon between 2.5  $\mu$ m and 20  $\mu$ m, using reflectivity and transmission. Engstrom found that the Drude model gave the correct optical constants for heavily doped p-type silicon when used in a multilayer model.

Wagner, Schaefer and Kempf [12] in 1981 compared different techniques available for characterising arsenic implanted silicon wafers. The techniques used were four point probe, bevel and stain, secondary ion mass spectroscopy, spreading resistance, incremental sheet resistance and infrared transmittance and reflectivity. The wafers used were front and back polished. The infrared methods were most reliable for surface concentration and sheet resistivity but not for implant depth. For implant depth the shape of the profile assumed for the analysis had considerable importance. Certainly with the high dose implants used in these experiments the solubility limit of arsenic in silicon was exceeded and the simple Gaussian fit to the carrier concentration should no longer be valid. Results to be presented in chapters 3, 5 and 6 for the most heavily doped

## CHAPTER 1

samples again show similar sensitivity to the details of the implant profile.

Pickering [13] in 1982 looked at indium phosphide layers grown by vapour phase epitaxy in the 14  $\mu\text{m}$  to 330  $\mu\text{m}$  region. The layers grown were between 3  $\mu\text{m}$  and 15  $\mu\text{m}$  thick. Comparisons were made with Hall measurements and electrochemical profiles. Theoretical and experimental curves were matched and results derived for carrier density and mobility. As the layer carrier density dropped so did the accuracy of the infrared results due to the increased penetration depth of the radiation. The model used was a single layer on a substrate. This was extended for use with a buried layer. More complex structures would require a multilayer approach, but this leads to more fitting variables.

Pawlik [14] in 1982 derived exact equations for the reflectivity and transmission of ion-implanted laser annealed silicon. He concluded that for rapid and precise measurement of dopant profiles accurate values of the optical constants must be known.

Barter and Lux [15] in 1983 looked at reflectivity spectra of p doped silicon between 5  $\mu\text{m}$  and 40  $\mu\text{m}$ . The samples were either prepared by diffusion or ion-implantation. They used a multilayer theory and derived their optical constants from a Kramers-Kronig analysis of the reflectivity data from various heavily doped bulk silicon samples. Two equations were assumed for the scattering time covering concentration ranges from  $2 \times 10^{16}$  to  $9 \times 10^{18}$  electrons/ $\text{cm}^3$  and  $9 \times 10^{18}$  to  $10^{21}$  electrons/ $\text{cm}^3$ . These equations are mis-matched at  $9 \times 10^{18}$  electrons/ $\text{cm}^3$ . They found that the Drude theory works well up to 10  $\mu\text{m}$  and that the reflectivity results show up subtle changes in the implant distribution with depth. Their infrared results matched closely results from anodic oxidation followed by four point probe measurements.

## CHAPTER 1

Demakopoulou, Siapkas, Zheleva and Kushev [16] in 1985 reported theoretical calculations showing that the use of interference effects can magnify the plasma edge contribution from thin films and thus give more accurate results.

In 1986 [17] they reported theoretical calculations on uniformly doped epitaxial layers on a transparent substrate. The interference effects allow weakly absorbing films to be studied.

Campisano, Rimini, Borghesi, Guizzetti, Nosenzo and Stella [18] in 1987 studied the infrared reflectivity of heavily doped ion-implanted and laser annealed silicon. Their results for  $\tau$  and  $m^*$  vs. concentration match those used in chapter two pages 24 and 25.

### Summary

Work has progressed with time from bulk doped materials through epitaxial films to ion-implanted layers. The theories developed accordingly from simple analysis of bulk materials to a single layer on a substrate to multiple layers on a substrate. Some of the problems associated with the use of infrared studies of semiconductors are:

There is a trade off between film thickness and carrier concentration. i.e. the thinner a film is, the higher the carrier concentration has to be to affect the reflectivity noticeably.

The measurement of an implanted profile requires that the radiation penetrates deep enough into the sample. If the surface layer has too high a reflectivity this will not happen.

Samples used for transmission and reflectivity measurements require surface flatness sufficient for the wavelengths being used. Results presented in chapter 5

## CHAPTER 1

page 43/44 and 46 show diffuse scattering in the near infrared and coherent scattering in the far-infrared.

### The Focus of this Thesis

The papers reviewed at the beginning of this chapter show that infrared reflectivity and transmission can be used to characterise ion-implanted silicon wafers. Most of the papers use samples polished on both sides to allow near infrared transmission and substrate reflectivity results to be studied simultaneously.

My own work was industrially sponsored and used wafers as processed at Hughes Microelectronics Ltd. These are polished on the implanted side but un-polished on the substrate side. A polished rear surface is needed to run transmission experiments in the near infrared to give total dose information. Increasing the wavelength range of the investigations (to include near-, mid- and far-infrared as well as millimeter and centimeter) the requirement for polishing the wafers rear surface is removed. The longer wavelengths are not scattered by the wafers rear surface, and they have a greater penetration depth which allows very high implant doses to be measured in transmission. The interference fringes observed in the far-infrared help to multiply the contribution of the lower dose implants [16, 17] and extend the sensitivity to dose.

Whilst the accurate derivation of all of the ion-implanted characteristics from contactless and non-destructive techniques is desirable it is not the most important aim. In a production environment reproducibility is vital. Any technique which allows rapid assessment of implant uniformity and consistency is useful. Optical methods covered in this thesis allow the comparison of a wafer with a standard. Deviations in the reflection and transmission characteristics can be interpreted to give the implant distribution

## CHAPTER 1

variations. This allows corrective action to be taken by the manufacturer.

### Background [19]

Ion-implantation involves firing dopant ions at a host semiconductor substrate with sufficient energy for them to penetrate the surface. This causes disruption in the host lattice. Defects and vacancies form and these have to be annealed out.

The annealing time and temperature depends on the type and extent of the damage caused. The crystal quality of the annealed semiconductor also depends on the extent of the original damage.

### Damage and Annealing in Silicon [19]

Individual and interstitial vacancies are caused by a host atom being struck by an ion and displaced from its lattice site. The vacancies anneal at very low temperatures, between 70 K and 150 K.

Double vacancies occur when neighbouring host atoms are displaced. These vacancies anneal at temperatures around 550 K.

Vacancy clusters occur as the implanted dose is increased. These transform into dislocations at temperatures between 200 K and 300 K.

Phosphorus implants above a dose of  $6 \times 10^{14}$  ions/cm<sup>2</sup> cause the entire surface of the silicon wafer to become amorphous.

Back scattering measurements with 1 MeV to 5 MeV protons indicate that most of the damage is annealed out by 1000°C. Dislocation lines and loops only anneal at temperatures greater than 1000°C. The process for amorphous layers is totally different. The layer recrystallises from the undamaged substrate in a quasi epitaxial manner. This occurs at lower

## CHAPTER 1

temperatures than above, around 500°C to 650°C. The implanted ions are fully activated by this process as well.

Problems occur for partially amorphised surface layers. These can start to recrystallise in many places simultaneously, and this leads to a high density of dislocations. Thus the annealing temperature must then be taken above 1000°C to remove the damage and activate all of the implanted ions.

For the doses used in most of my work the silicon wafers surface would be totally amorphous. This means that the subsequent anneal would proceed smoothly.

### Solubility [20]

The limit on the maximum carrier concentration that a semiconductor can be implanted with is set by the solubility of the dopant in the host semiconductor.

For phosphorus in silicon at the annealing temperatures used of 950°C (chapter 4 pages 35 and 36) the solubility limit is at least  $8 \times 10^{20}$  atoms/cm<sup>3</sup>. The limit for arsenic is about  $1.1 \times 10^{21}$  atoms/cm<sup>3</sup>. The accuracy of the above data is to within  $\pm 20\%$ . At doses approaching the solubility limit the implanted layer will be amorphous before annealing and thus will fully anneal at a lower temperature than for smaller doses, see previous section on annealing (page 13).

### Mobility vs. carrier concentration

Results collected by Mayer, Ericksson and Davis [21] show that the mobilities of carriers in ion-implanted and annealed layers in silicon follow the values for bulk silicon with the same carrier concentrations.

## CHAPTER 2

### REFLECTIVITY THEORY

#### Introduction

One theoretical method for treating the optical characteristics of an ion-implanted wafer involves a multiple thin film approach. The implanted layer, with arbitrary doping as a function of depth, is treated as an assembly of uniformly doped layers (Figure 1). The substrate is treated as a final uniformly doped layer. The optical properties of this structure are then calculated using a matrix method described later.

The theoretical implant profile can be adjusted, allowing reflectivity or transmission curves to be fitted to the experimental data. Once the best fit is found, the calculated profile should match the real implant giving the implant depth, activated dose, sheet resistivity and surface concentration - all evaluated non-destructively.

The refractive index for each of the layers is calculated from a free electron model as described later.

#### Thin Film Reflectivity e.g.[22]

Solving Maxwell's equations (c.g.s. units):

$$\text{curl } \mathbf{H} = 4\pi\mathbf{J}/c + 1/c \delta\mathbf{D}/\delta t \quad 1$$

$$\text{curl } \mathbf{E} = -1/c \delta\mathbf{B}/\delta t \quad 2$$

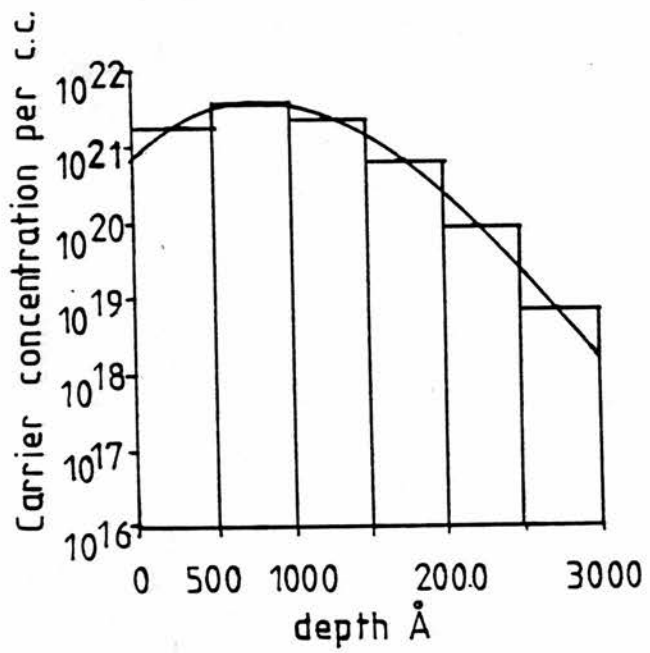


Figure 1

Implant concentration vs.  
depth.

Actual and model.

CHAPTER 2

$$\mathbf{D} = \epsilon \mathbf{E} \quad 3$$

$$\text{div } \mathbf{D} = 4\pi\rho \quad 4$$

$$\mathbf{E} = \mu \mathbf{H} \quad 5$$

$$\text{div } \mathbf{E} = 0 \quad 6$$

$$\mathbf{J} = \sigma \mathbf{E} \quad 7$$

where  $\mathbf{E}$  is the electric vector,  $\mathbf{H}$  is the magnetic vector,  $\mathbf{J}$  is the electric current density,  $\mathbf{D}$  is the electric displacement,  $\mathbf{E}$  is the magnetic induction,  $\rho$  is the electric charge density,  $\sigma$  is the conductivity,  $\mu$  is the magnetic permeability,  $\epsilon$  is the dielectric constant and  $t$  is time.

If there is no space charge in the medium then  $\text{div } \mathbf{D} = 0$ , and solving for  $\mathbf{E}$ ,

$$\nabla^2 \cdot \mathbf{E} = \epsilon\mu/c^2 \cdot \delta^2 \mathbf{E} / \delta t^2 + 4\pi\sigma\mu/c^2 \cdot \delta \mathbf{E} / \delta t \quad 8$$

A plane wave solution of the form

$$\mathbf{E} = \mathbf{E}_0 e^{i\omega(t - x/v)} \quad 9$$

requires that

$$c^2/v^2 = \epsilon\mu - 4\pi\sigma\mu/\omega \quad 10$$

writing  $c^2/v^2 = N^2$  implies  $N$  is of the form

$$N = c/v = n - ik \quad 11$$

with

$$n^2 - k^2 = \epsilon\mu \quad 12$$

and

$$2nk = 4\pi\sigma\mu/\omega \quad 13$$

## CHAPTER 2

When the plane wave, described by equation 9, impinges on a simple boundary (Figure 2), the wave is split into two components: the reflected wave and the transmitted wave. Solving for the phase factors at the boundary, where the tangential components of  $\underline{E}$  and  $\underline{H}$  are continuous gives

$$\omega_i = \omega_r = \omega_t \quad \text{i.e. no frequency change at the boundary}$$

$$\delta_r = \delta_t \quad \text{i.e. no phase change at the boundary}$$

$$N_0 \sin \theta_0 = N_1 \sin \theta_t \quad (\text{Snells law})$$

$$\theta_0 = \theta_r \quad (\text{angle of incidence} = \text{angle of reflection})$$

Continuing the analysis, the energy reflection can be derived and is given by

$$R = rr^* \quad \text{with } r = (q_0 - q_1) / (q_0 + q_1) \quad 14$$

where

$$q_r = N_r / \cos \theta_r \quad \text{for transverse magnetic waves}$$

and

$$q_r = N_r \cos \theta_r \quad \text{for transverse electric waves}$$

To extend the analysis to a thin film (film thickness less than a few wavelengths [21,p17]) on an infinite substrate (figure 3) first consider boundary 'b' where there is no -ve going wave. Thus the waves in the adjacent film,  $N_1$ , can be summed into one resultant +ve going wave and one resultant -ve going wave.

At the same time and at a point with the same x- and y-coordinates, the situation at boundary 'a' differs only by a

Figure 2

Simple boundary

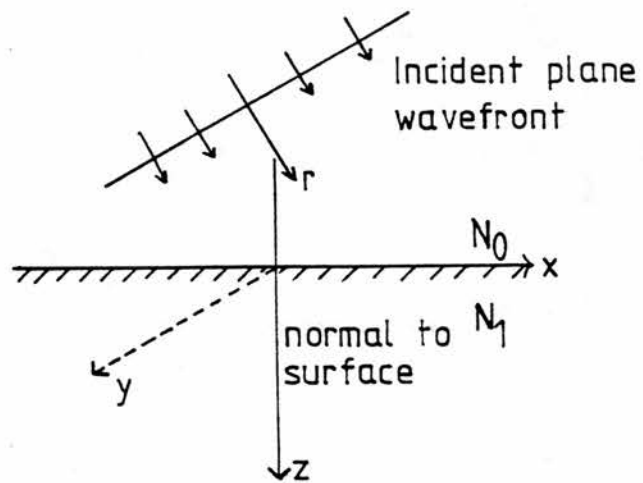
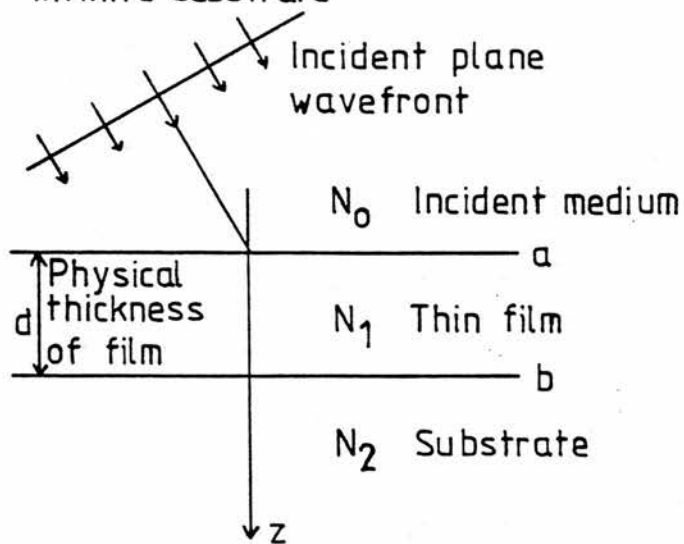


Figure 3

Single thin film on an infinite substrate



CHAPTER 2

phase factor which effectively shifts the z-coordinate from 0 to -d. The phase of the +ve going wave will be multiplied by  $e^{i\delta}$  where

$$\delta = (2\pi N_1/\lambda) \cdot \cos\theta_1 \cdot d \quad 15$$

while the -ve going wave will be multiplied by  $e^{-i\delta}$ . Using these conditions it is possible to show that

$$\mathbf{k} \times \mathbf{E}_a = \mathbf{k} \times \mathbf{E}_b \cdot \cos\delta_1 + (1/q_1)\mathbf{H}_b \cdot i\sin\delta_1 \quad 16$$

and

$$\mathbf{H}_a = q_1 \mathbf{k} \times \mathbf{E}_b \cdot i\sin\delta_1 + \mathbf{H}_b \cdot \cos\delta_1 \quad 17$$

This can be written in matrix notation as

$$\begin{bmatrix} \mathbf{k} \times \mathbf{E}_a \\ \mathbf{H}_a \end{bmatrix} = \begin{bmatrix} \cos\delta_1 & (i\sin\delta_1)/q_1 \\ iq_1\sin\delta_1 & \cos\delta_1 \end{bmatrix} \begin{bmatrix} \mathbf{k} \times \mathbf{E}_b \\ \mathbf{H}_b \end{bmatrix} \quad 18$$

where

$$\delta = (2\pi N/\lambda) \cdot d \cdot \cos\theta \text{ and } q = N \cdot \cos\theta \text{ (s-waves)}$$

$$\text{or } q = N/\cos\theta \text{ (p-waves)}$$

The admittance of the assembly, Y, is given by

$$Y = \mathbf{H}_a / (\mathbf{k} \times \mathbf{E}_a) \quad 19$$

and equation 14 can be written as

$$R = rr^* \text{ with } r = (q_0 - Y)/(q_0 + Y) \quad 20$$

CHAPTER 2

Finally, the reflectance of an assembly of thin films can be found by adding another film to the previous single film (Figure 4); the final interface is denoted by c.

The characteristic matrix of the film nearest the substrate, from equation 18, is,

$$\begin{bmatrix} \cos\delta_2 & (i\sin\delta_2)/q_2 \\ iq_2\sin\delta_2 & \cos\delta_2 \end{bmatrix} \quad 21$$

Applying the previous result, equation 18, for one thin film gives

$$\begin{bmatrix} k \times E_a \\ H_a \end{bmatrix} = \begin{bmatrix} \cos\delta_1 & (i\sin\delta_1)/q_1 \\ iq_1\sin\delta_1 & \cos\delta_1 \end{bmatrix} \begin{bmatrix} \cos\delta_2 & (i\sin\delta_2)/q_2 \\ iq_2\sin\delta_2 & \cos\delta_2 \end{bmatrix} \begin{bmatrix} k \times E_c \\ H_c \end{bmatrix}$$

Extending this treatment to the general case of n layers (Figure 5), gives the characteristic matrix as the product of the individual matrices taken in the correct order,

$$\begin{bmatrix} B \\ C \end{bmatrix} = \prod_{r=1}^n \begin{bmatrix} \cos\delta_r & (i\sin\delta_r)/q_r \\ iq_r\sin\delta_r & \cos\delta_r \end{bmatrix} \begin{bmatrix} 1 \\ q_{n+1} \end{bmatrix} \quad 22$$

where

$$\delta_r = 2\pi N_r d_r \cos\theta_r / \lambda$$

$$q_r = N_r \cos\theta_r \quad \text{for TE waves}$$

$$q_r = N_r / \cos\theta_r \quad \text{for TM waves}$$

The total thickness of the films is likely to be less than a few wavelengths. Experimentally, for the treatment of

Figure 4

Two layer model

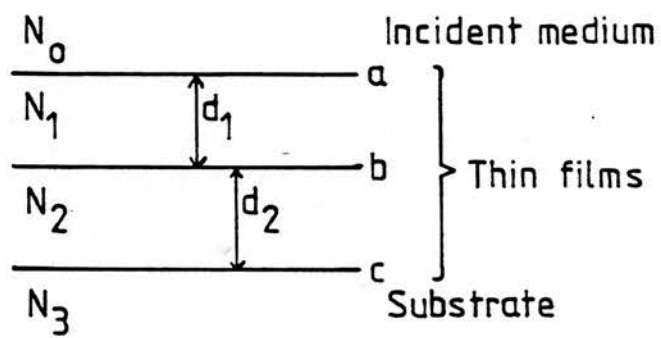
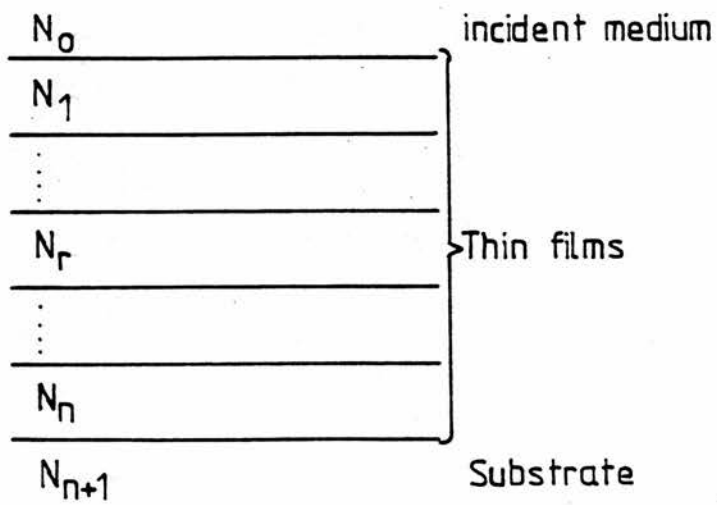


Figure 5

Assembly of n layers



## CHAPTER 2

an ion-implanted silicon wafer (about 350  $\mu\text{m}$  thick) in the 2  $\mu\text{m}$  to 10  $\mu\text{m}$  wavelength region, interference effects can be neglected. This is due to the relatively poor collimation and limited resolution of the blazed grating spectrometer along with the diffuse reflection from the unpolished rear surface of the wafer. In contrast the rear of the wafer acts as a coherent reflector in the far-infrared and strong interference fringes are seen.

For a given angle of incidence,  $\theta_0$ , the values of,  $\theta_r$ , can be found from Snell's law

$$N_0 \sin \theta_0 = N_r \sin \theta_r \quad 23$$

$$\text{and } Y = C/B \quad 24$$

The transmittance of the thin film assembly can be calculated by considering the energy flux. The transmittance is

$$T = q_{n+1} (1 - R) / \text{Real part}(BC^*) \quad 25$$

The absorption, A, of the structure is connected to R and T by

$$1 = R + T + A \quad 26$$

## CHAPTER 2

### Free Electron Model e.g.[23,24]

The previous expression for the characteristic matrix of a multilayer structure (equation 22) requires knowledge of the refractive indices of each layer. For an annealed ion-implanted wafer the surface has a high concentration of free electrons which can be treated as a plasma. The refractive index as a function of electron concentration can be calculated from this as follows.

An electron in a time varying electric field,  $\epsilon$ , changes its momentum in a time,  $\delta t$ , by

$$\delta(m^*v) = -e\epsilon\delta t' = \text{Force} \quad 27$$

If the scattering process can be characterised by a momentum relaxation time,  $\tau$ , then

$$\delta(m^*v)_t = \delta(m^*v)_{t_0} \cdot \exp(-(t_0 - t')/\tau) \quad 28$$

and substituting equation 27 for  $\delta(m^*v)_t$  gives

$$m^*v = \int_{-\infty}^t -e\epsilon\delta t' \exp(-(t_0 - t')/\tau) \quad 29$$

For an electromagnetic wave  $\epsilon(t') = \epsilon_0 \exp(-i\omega t')$  this gives the variation of electron velocity with time as

$$v(t) = (-e\epsilon(t)/m^*) (\tau/(1 + i\omega\tau)) \quad 30$$

The conductivity is defined as

$$\sigma = -Ne v / \epsilon(t) = \sigma_1 + i\sigma_2 \quad 31$$

## CHAPTER 2

Substituting equation 30 for  $v$  gives

$$\sigma_1 = (Ne^2\tau/m^*) (1/(1 + \omega^2\tau^2)) \quad 32$$

and

$$\sigma_2 = (Ne^2\tau/m^*) (\omega\tau/(1 + \omega^2\tau^2)) \quad 33$$

The D.C. conductivity,  $\sigma_0$ , is given by

$$\sigma_0 = Ne^2\tau/m^* \quad 34$$

The dielectric constant,  $\epsilon(\omega) = \epsilon_L - \epsilon_1 + i\epsilon_2$  35

where from equations 11, 12, 13 and 35 the conductivity contributions,  $\epsilon_1$  and  $\epsilon_2$ , are given by

$$\epsilon_1 = 4\pi\sigma_2/\omega \quad 36 \quad \text{and} \quad \epsilon_2 = 4\pi\sigma_1/\omega \quad 37$$

and  $\epsilon_L$  is the lattice dielectric constant appropriate for the wavelength range of measurement = 11.8 for silicon. The change in  $\epsilon_L$  when  $\omega = \omega_{LO}$  is zero because silicon is homopolar and has no first order dipole fields, therefore there is no interaction with optic phonons. In a polar material  $\epsilon_L \approx \epsilon_\infty$  for  $\omega < \omega_{LO}$  and  $\epsilon_L \approx \epsilon_\infty$  for  $\omega > \omega_{LO}$ .

Substituting the above relations for  $\sigma_1$ ,  $\sigma_2$  and  $\sigma_0$ , equations 32, 33 and 34 into equations 36 and 37 gives

$$\epsilon_1 = 4\pi\tau\sigma_0/(1 + \omega^2\tau^2) \quad 38$$

and

$$\epsilon_2 = 4\pi\sigma_0/(\omega(1 + \omega^2\tau^2)) \quad 39$$

## CHAPTER 2

From  $\epsilon(\omega)$ , equation 35, the complex refractive index can be found using equations 12 and 13,

$$n^2 - k^2 = \epsilon_L - \epsilon_1 \quad 40 \quad \text{and} \quad 2nk = \epsilon_2 \quad 41$$

If the electron concentration, the effective mass and the scattering time are known for the sample concerned, the complex refractive index for that material is completely determined. The effective mass is essentially a constant for the material concerned and the carrier concentration and scattering time can be determined by curve fitting the observed dependence of the refractive index on frequency.

Rearranging equations 38 & 39 and defining the plasma frequency,  $\omega_p$ , as

$$\omega_p^2 = 4\pi Ne^2/\epsilon_L m^* \text{ (cgs)} = Ne^2/\epsilon_0 \epsilon_L m^* \text{ (SI)} \quad 42$$

gives

$$\epsilon_1 = \epsilon_L \omega_p^2 \tau^2 / (1 + \omega^2 \tau^2) \quad 43$$

and

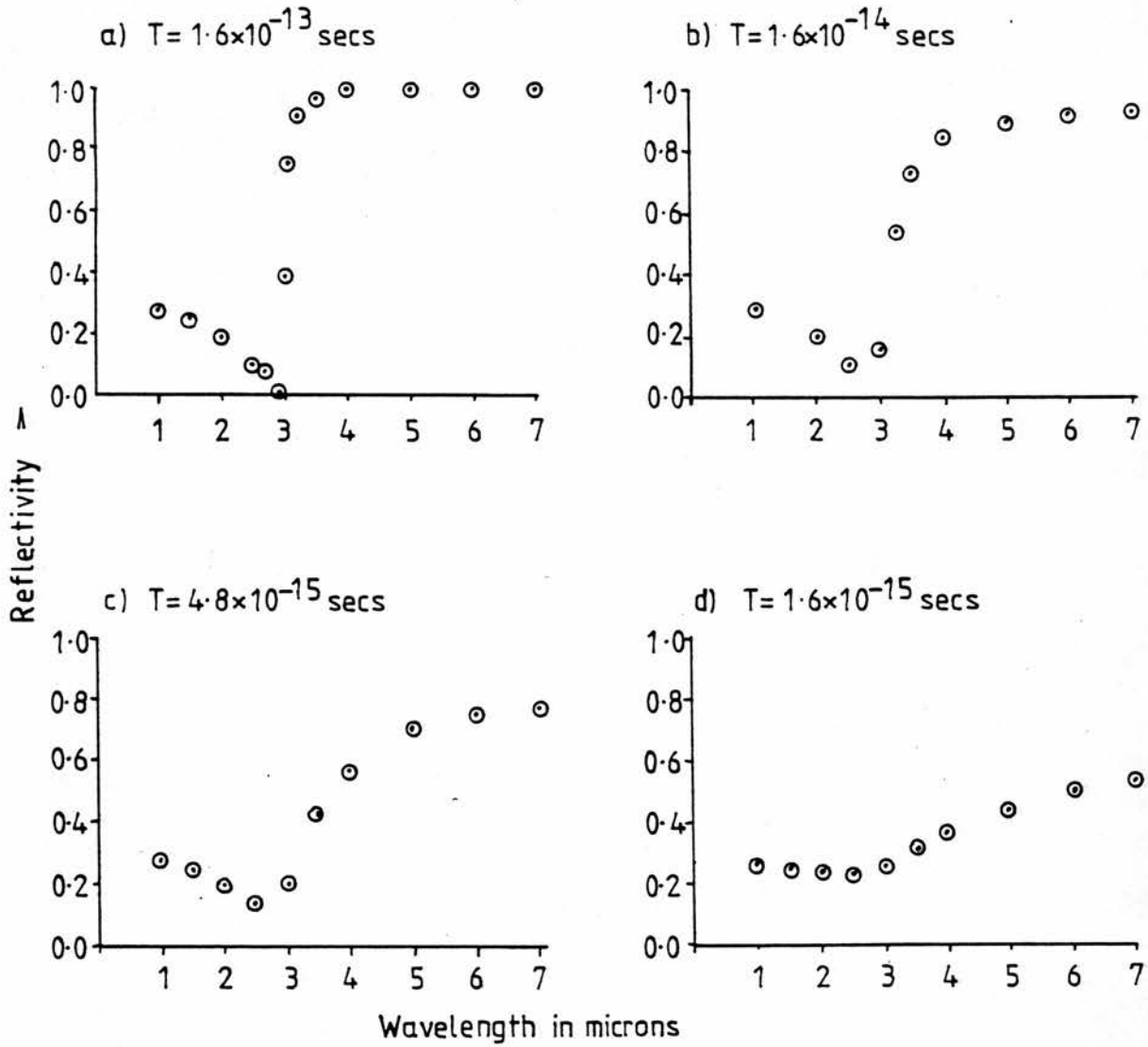
$$\epsilon_2 = \epsilon_L \omega_p^2 \tau / (\omega(1 + \omega^2 \tau^2)) \quad 44$$

As an example of the reflectance effects, characterised by free electron absorption (which can be analysed without the use of time consuming thin film equations), consider figure 6. Here a bulk sample of silicon with an electron concentration of  $3.5 \times 10^{19} \text{ cm}^{-3}$  was analysed and the reflectivity is plotted as a function of wavelength for four values of relaxation time.

The minimum in reflectivity occurs when the refractive index matches that of the incident medium. The large increase in reflectivity is caused by  $n$ , the real part of the refractive index falling below one. For lower values of the

Figure 6

Plots of reflectivity vs. wavelength for four relaxation times with the plasma wavelength = 3 microns



## CHAPTER 2

scattering time,  $\tau$  ( $4.8$  &  $1.6 \times 10^{-15}$  secs),  $n$  does not fall below one and the change in reflectivity is not as dramatic. It is clear from these figures that the position of the minimum in the reflectivity is essentially independent of the mobility and hence can be used to determine the carrier concentration rather directly.

When viewing the experimental data presented in chapter 4 the same reflectivity vs. wavelength structure is seen and the theory described above is used to model this.

By using the multilayer theory described earlier to determine the implant profile, and the free carrier absorption theory to provide the refractive index, the electrical characteristics can be contactlessly probed by optical means.

For  $N = 10^{22} \text{ cm}^{-3}$ ,  $\mu = 70 \text{ cm}^2/\text{Vs}$  and  $m^* = 0.3 m_0$  (as appropriate for heavily doped silicon). The plasma frequency lies in the near infrared at  $\nu = 4.3 \times 10^{13} \text{ Hz}$ ,  $\lambda = 6 \text{ }\mu\text{m}$ .

### Electron Mobility

Figure 7 shows the data used at Hughes Microelectronics Ltd. in Glenrothes as well as a plot of the two formula used at Plessey for mobility vs. donor concentration in silicon. As indicated in chapter one reference [21] the bulk and thin film mobilities vs. carrier concentration are believed to be the same.

For  $N < 10^{20} \text{ cm}^{-3}$

$$\mu = [\mu_1 / (1 + (N/N_r)^\alpha)] + \mu_0 - \beta N \quad 45$$

$$\beta = 1.4 \times 10^{-19} \text{ cm}^{-1} \text{V}^{-1} \text{s}^{-1}$$

$$\mu_0 = 86.5 \text{ cm}^2 \text{V}^{-1} \text{s}^{-1}$$

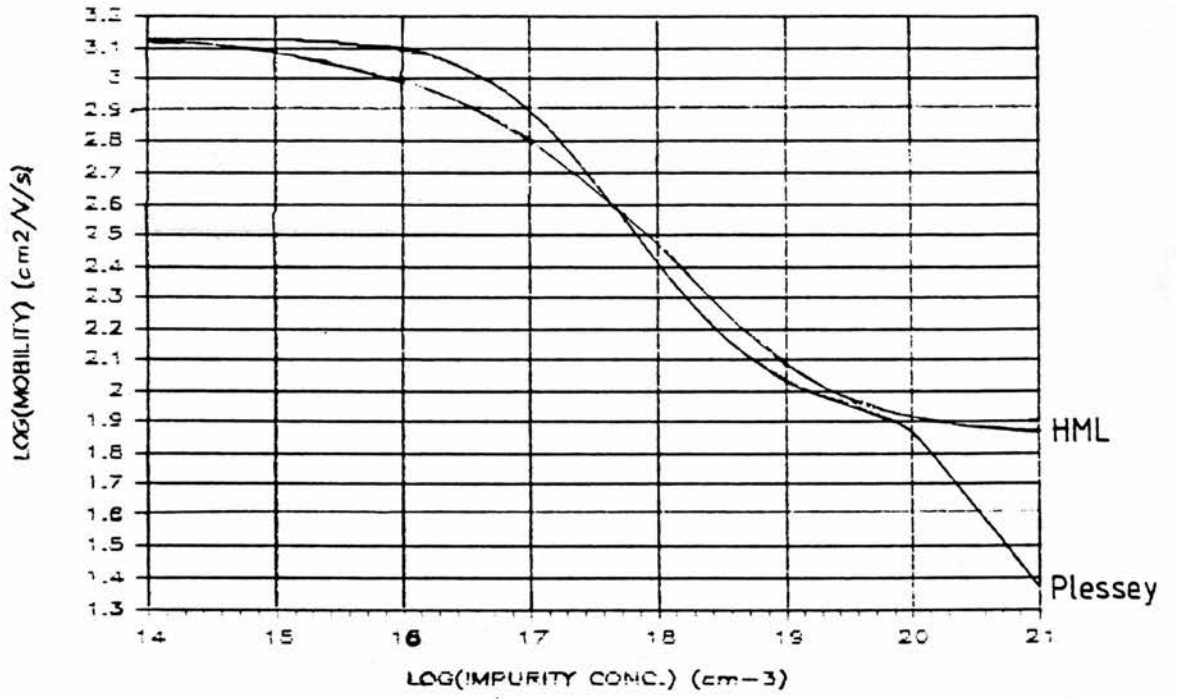
$$\mu_1 = 1268 \text{ cm}^2 \text{V}^{-1} \text{s}^{-1}$$

$$\alpha = 0.91$$

$$N_r = 1.3 \times 10^{17} \text{ cm}^{-3}$$

Figure 7

### ELECTRON MOBILITY VS CONC.



$$\text{For } N > 10^{20} \text{ cm}^{-3}$$

$$\mu = 7.5 \times 10^{11} / N^{1/2}$$

46

These curves are in close agreement with values quoted by W.G. Spitzer and H.Y. Fan [11], Marek Pawlik [14] and H.I. Ralph and G. Simpson [25].

The mobility figures are used in the theoretical calculations of chapter 3 (appendix A) to derive the scattering time,  $\tau$ . Formulas 45 and 46 are empirical relationships for D.C. mobilities measured at thermal energies (about 0.025 eV). Many authors assume that the scattering time derived from D.C. Hall and conductivity measurements is applicable in A.C. formulae at infrared energies (up to 0.6 eV). However there is considerable evidence that D.C. and A.C. scattering times can differ very substantially, particularly in the cases where impurity scattering is dominant or when the measuring frequency is comparable with the phonon frequencies involved (e.g. Stradling and Zhukov [26]). In the case of ionised impurity scattering, the predominant small-angle scattering and the effects of screening are very much modified by the presence of a magnetic field or at high frequencies. However, at photon energies close to the band gap, most authors find that the damping of the electron motion is fairly well described by the D.C. parameters.

#### Electron Effective Mass.

Work by Howarth and Gilbert [3] indicates that the effective mass in silicon varies by less than 10% over the concentration range  $10^{19}$  to  $2 \times 10^{20}$  electrons  $\text{cm}^{-3}$ . Stradling and Zhukov [26] found a 10% non-parabolicity change in the density-of-states mass at an energy of  $\approx 40$  meV. A Fermi energy of this order corresponds to a carrier concentration of  $10^{20} \text{ cm}^{-3}$  and so this result agrees with that of Howarth and Gilbert. Their work uses bulk doped silicon characterised by Hall and resistivity measurements. The reflectivity in the  $2 \mu\text{m}$  to  $20 \mu\text{m}$  region was measured. Then, using the procedure adopted by Spitzer and Fan [11], the effective mass was calculated. Because uniformly doped bulk material was studied, the plasma frequency is simply related to the effective mass, equation 42. The impurity concentrations used in chapter 3 to model ion-implanted layers corresponds to an effective mass, as measured by Howarth and Gilbert, of  $0.3 m_0 \pm 0.03 m_0$ . Thus the value assumed for  $m^*$  in the following work is  $0.3 m_0$ .

## CHAPTER 3

### COMPUTER PROGRAMME PREDICTIONS

To apply the theory in chapter two to the prediction of reflectivity, transmission and absorption vs. wavelength (or frequency) in an ion-implanted silicon wafer involves considerable calculation. The BASIC programme listed in Appendix A carries out these calculations.

The programme is organised in the following way:

Data is initialised with typical values to reduce the changes that have to be introduced later to model real implant conditions. Data changes are accomplished through the use of three menus.

The first menu covers data known about the sample: implant dose, background impurity concentration, implant depth, the radiation (light) incident angle and wafer thickness. Implant depth is, to some extent, a variable, dependent on implant energy, crystal orientation, oxide layer thickness and ion type. Approximate ranges for phosphorus ions accelerated into silicon are known [27] (see also table 14 chapter 6 page 62), assuming no channelling takes place. All the experimental implants took place at the same implant energy.

In the calculation a boundary is assumed between the region where the conductivity is varying as a function of depth and a substrate region of background doping. The implant depth is defined as the position of the boundary between these two regions.

The second menu covers calculation details: the number of layers that the ion-implanted region is to be split into, the resolution (or number of points to calculate) to cover the wavelength range, the mean peak position of the Gaussian distribution of implanted ion concentration with depth, the

## CHAPTER 3

standard deviation of the implanted ions with depth, whether to use a fitting parameter or a formula (chapter 2 equation 45 and 46) for the scattering time and finally whether the rear surface of the sample should be included in the calculation. As described earlier (Chapter 2 page 20), the grating spectrometers resolution and collimation was insufficient to show interference effects due to the silicon wafer surfaces. Also the back surface was a diffuse reflector in the near infrared. The programme is not limited in this way, so in the near infrared an infinite substrate was assumed to reproduce the experimental situation (because the rear surface of the silicon wafer is unpolished and in the near infrared reflects diffusely thus the power returning from the rear of the wafer is very small and can be neglected. This also leads to poor results in transmission in the near infrared. As the incident wavelength increases the diffuse scattering caused by the rear surface is reduced). In the far-infrared and microwave regions interference effects are seen in the experimental results as the reflections from the rear of the wafer interact coherently (Figure 43) and a parallel sided sample is assumed for these calculations.

The third menu covers the calculation limits; whether to use a linear wavelength or frequency scale and the wavelength calculation limits.

A DO LOOP now calculates the electron concentration for each layer. The assumption of a Gaussian distribution of ions with depth, where the mean and standard deviation of the distribution are given in the second menu, allows the number of ions for each layer to be found. The number of ions, assuming 100% activation, is equal to the number of electrons, which divided by the layer thickness gives the mean electron density.

### CHAPTER 3

The next DO LOOP uses the above electron densities for each wavelength, finds the complex refractive index (Chapter 2 equations 43 and 44) and forms the characteristic matrix for each layer (Chapter 2 equation 21); then combining these individual characteristic matrices gives the characteristic matrix for the assembly of layers at one wavelength (Chapter 2 equation 22). If a rear surface is to be incorporated in the calculation this is treated as a final, much thicker, layer and gives the characteristic matrix for the wafer. From the characteristic matrix the reflectivity, transmission and absorption at one wavelength are calculated (Chapter 2 equations 20, 25 and 26).

This process is repeated for each of the wavelengths from the minimum to the maximum values with the number of points given by the resolution set in menu two, and the point spacing linear in wavelength or frequency depending on the selection in menu three.

A final menu is now used to display and/or plot this data. Since the display of results is system specific the programme listing in appendix A only stores and prints them.

The following figures (8 to 16) show the effect on reflectivity of varying one parameter whilst keeping the others fixed.

The constant values assumed in this sequence are:

Implant dose	$5 \times 10^{15}$ ions/cm <sup>2</sup>
Background concentration	$10^{14}$ electrons/cm <sup>3</sup>
Implant depth	2500 Å
Incident angle	45°
Wafer thickness	365 µm
Number of layers	20
Number of points	50
Gaussian peak depth	549 Å
Gaussian standard deviation	417 Å
Scattering time	$1.5 \times 10^{-15}$ seconds

Figures 8, 9 and 10  
 Reflectivity vs. Angle  
 Implant Dose  
 Scattering Time

Figure 9 Reflectivity vs. Implant Dose  
 Optical characteristics of ion implanted Silicon

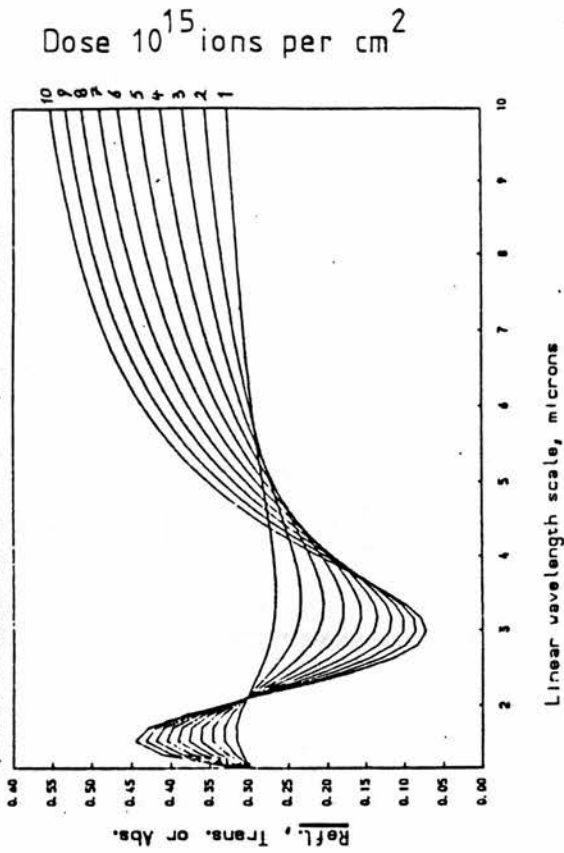


Figure 8 Reflectivity vs. Angle 45° and 90° to the surface  
 Optical characteristics of ion implanted Silicon

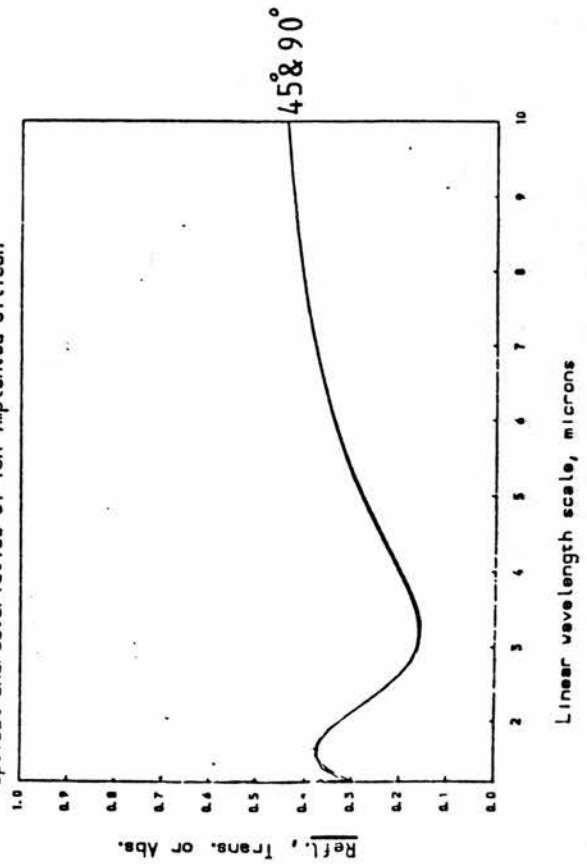
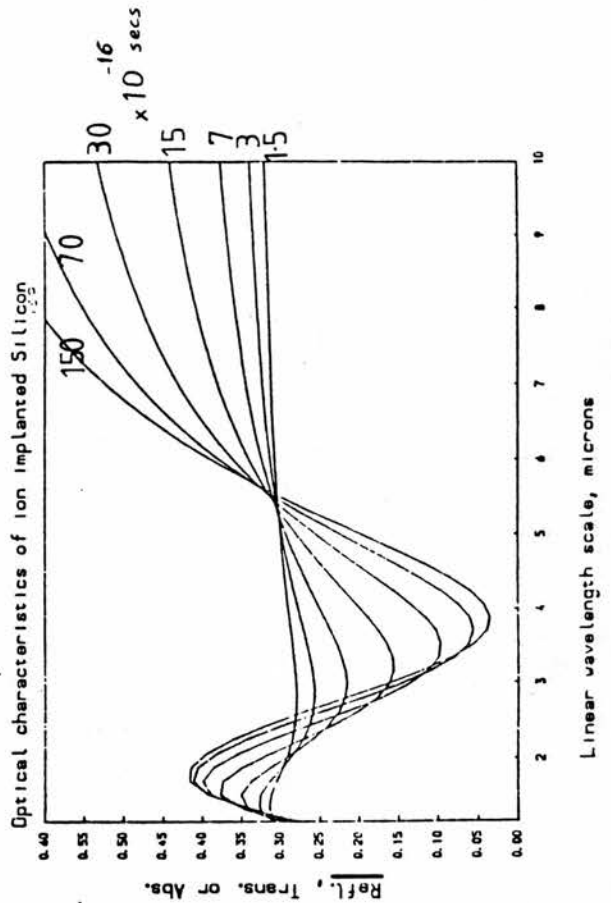


Figure 10 Reflectivity vs. Scattering Time



## CHAPTER 3

An infinite substrate is assumed because the rear surface of the silicon wafers is unpolished and in the visible and near infrared reflects diffusely. The calculation covers the 1  $\mu\text{m}$  to 10  $\mu\text{m}$  region.

Varying the background concentration has no effect on the reflectivity unless it approaches the lower implant concentration levels of  $4 \times 10^{19}$  electrons/ $\text{cm}^3$ . All the samples used had a background electron concentration over 10,000 times below this level.

The wafer thickness for all the wafers used in the experiments was determined from the interference fringe spacing (see figure 46 c) to be about 365  $\mu\text{m}$ .

Above five, the calculation became insensitive to the number of layers used to approximate the Gaussian distribution.

Figure 8 shows the variation in reflectivity for incident angles of 90° and 45° (normal and 45° to the wafer surface). The curves are typical for the above values, the reflectivity levelling off at wavelengths below 1  $\mu\text{m}$  to 0.3 (from  $((n - 1)/(n + 1))^2 = 0.3$  for silicon), a plasma minimum at about 3  $\mu\text{m}$  and a rising reflectivity at longer wavelengths because the surface layer of electrons is absorbing at infrared frequencies.

Figure 9 shows the variation of reflectivity with implant ion concentration from  $10^{15}$  to  $10^{16}$  ions/ $\text{cm}^2$ . As the number of implanted ions increases the modulation in reflectivity increases.

The scattering time could be treated as a variable or derived from an experimental formula as discussed in the section on electron mobility (Chapter 2 equations 45 and 46). If it was treated as a variable, then changes in the scattering time had a somewhat different effect on the reflectivity to the changes in implant dose, figure 10.

## CHAPTER 3

Figures 11, 12 and 13 show the effect of the implant depth and distribution:-

Figure 11: A deeper implant at constant dose shifts the minima in reflectivity to longer wavelengths and reduces its modulation.

Figure 12: The mean position of the distribution assumed for the calculation takes into account the oxide layer on the wafer. This has the effect of shifting the Gaussian peak closer to the silicon/SiO<sub>2</sub> interface. Although the oxide will in practice reduce the total number of ions contributing electrons, (those stopped in the oxide do not contribute,) the new ion distribution does bring the peak electron concentration closer to the silicon surface. This causes a more abrupt change in the refractive index and appears to increase the plasma frequency.

Figure 13: Changing the standard deviation of the ion-implant seems to have little effect on the reflectivity minima, but it does affect the modulation in reflectivity (figure 13). The closer grouped implant (curve 1 figure 13), gives a lower reflectivity at 3.3  $\mu\text{m}$  and a higher reflectivity at 9  $\mu\text{m}$  than the wider spread implants (curves 2 and 3 figure 13).

Figures 11 to 13 show that the shape of the reflectivity curve is sensitive to the shape of the implant profile. A more detailed study of the relationship between implant profile and reflectivity vs. wavelength is carried out in chapter 6 pages 56 to 59.

The behaviour of the calculated reflectivity (R), transmission (T) and absorption (defined as  $1 - R - T$ ) in the 1  $\mu\text{m}$  to 10  $\mu\text{m}$  region for the five different implants investigated are shown in figures 14, 15 and 16.

The number of points act to define the spectrum resolution vs. wavelength. For some of the plots with many

Figure 11 The Effect of Implant Depth On Reflectivity  
Computer Predictions

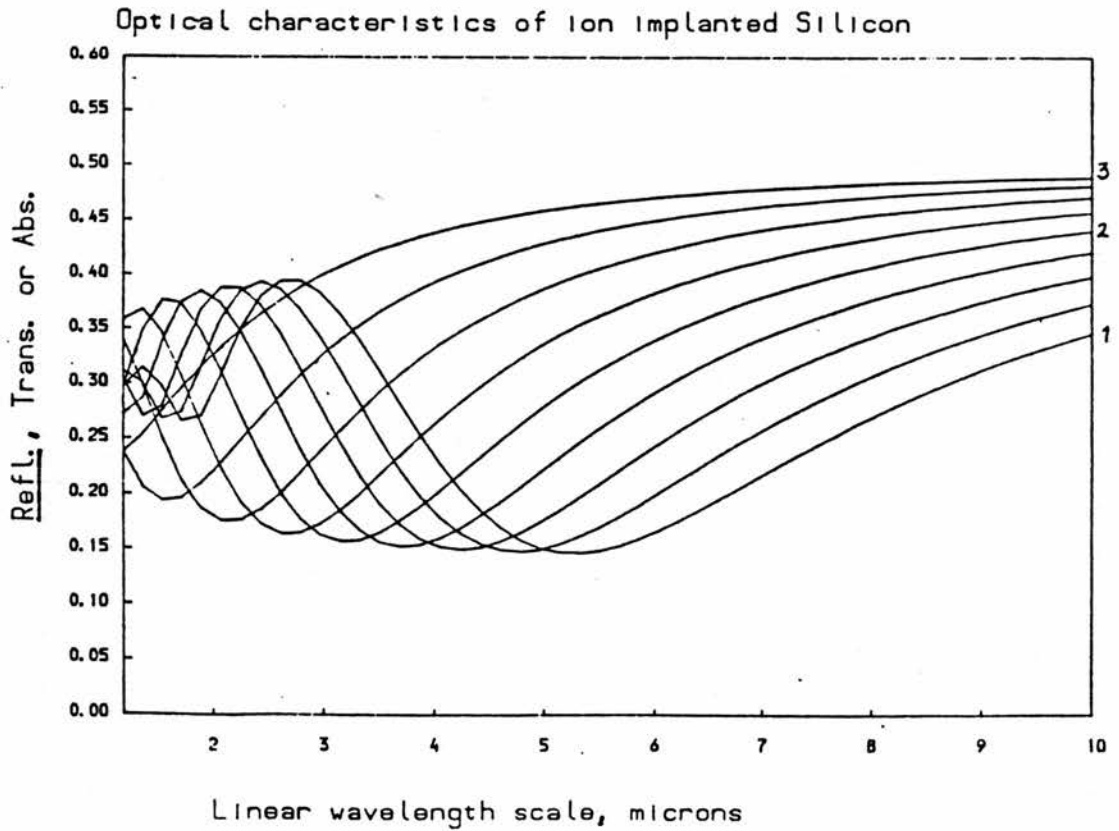
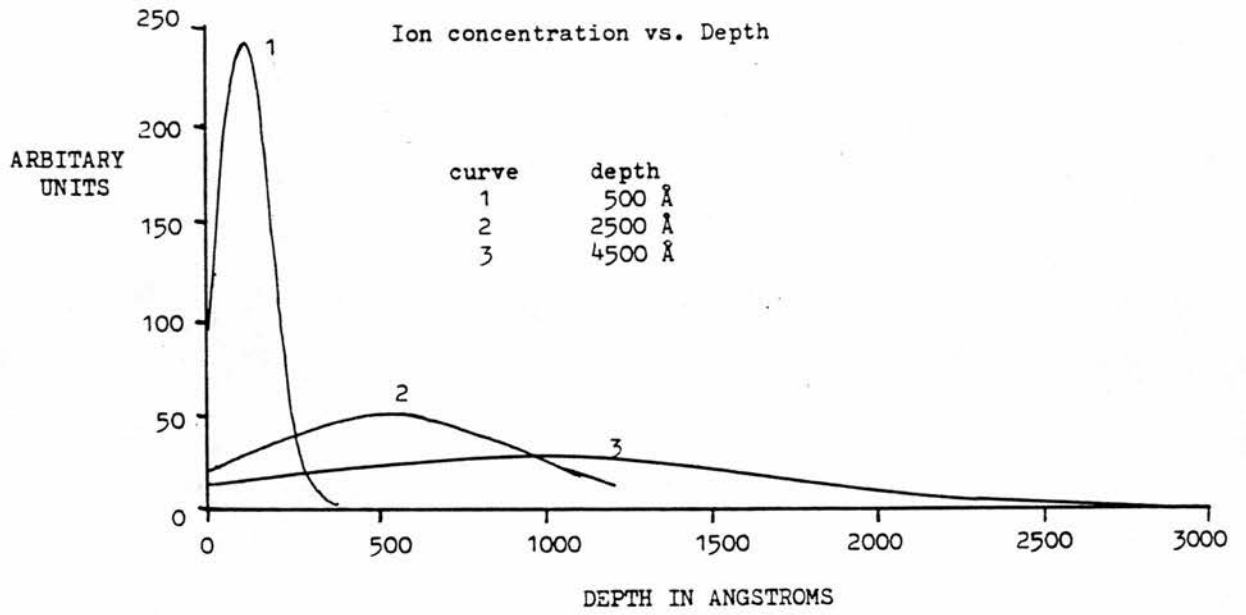


Figure 12 The effect of implant peak mean position on reflectivity  
Computer predictions

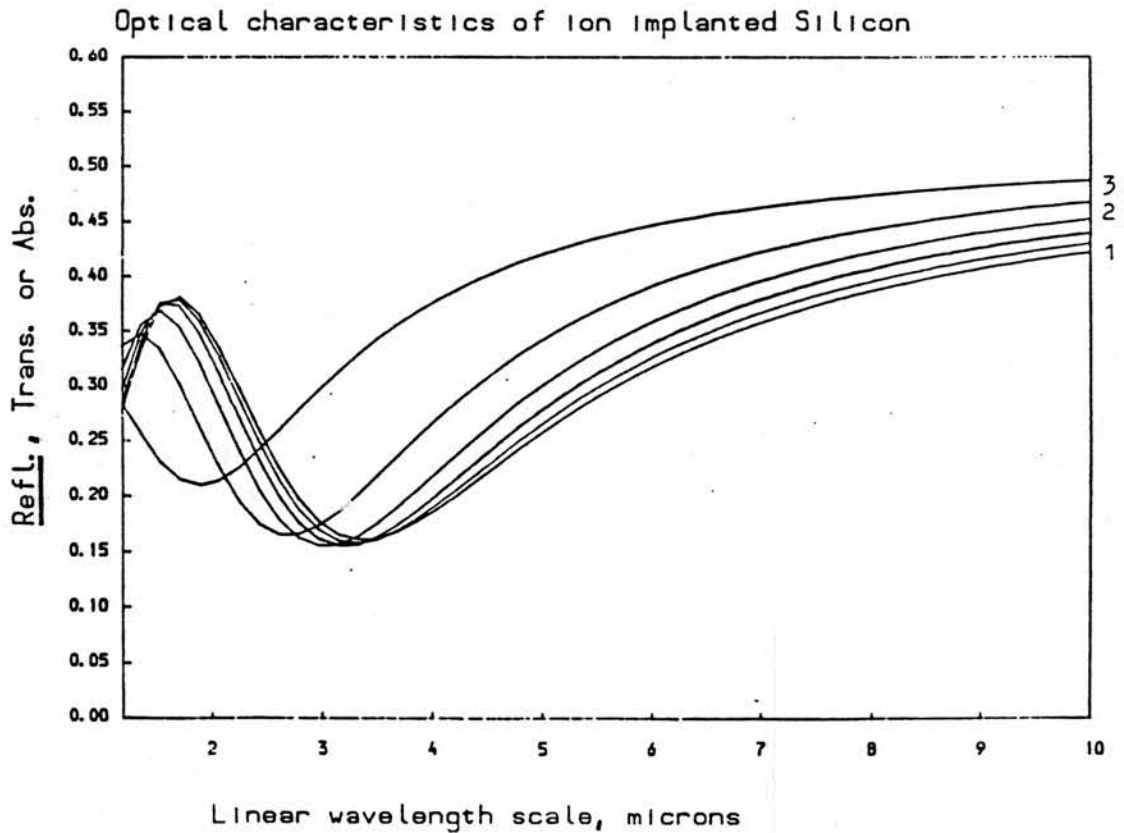
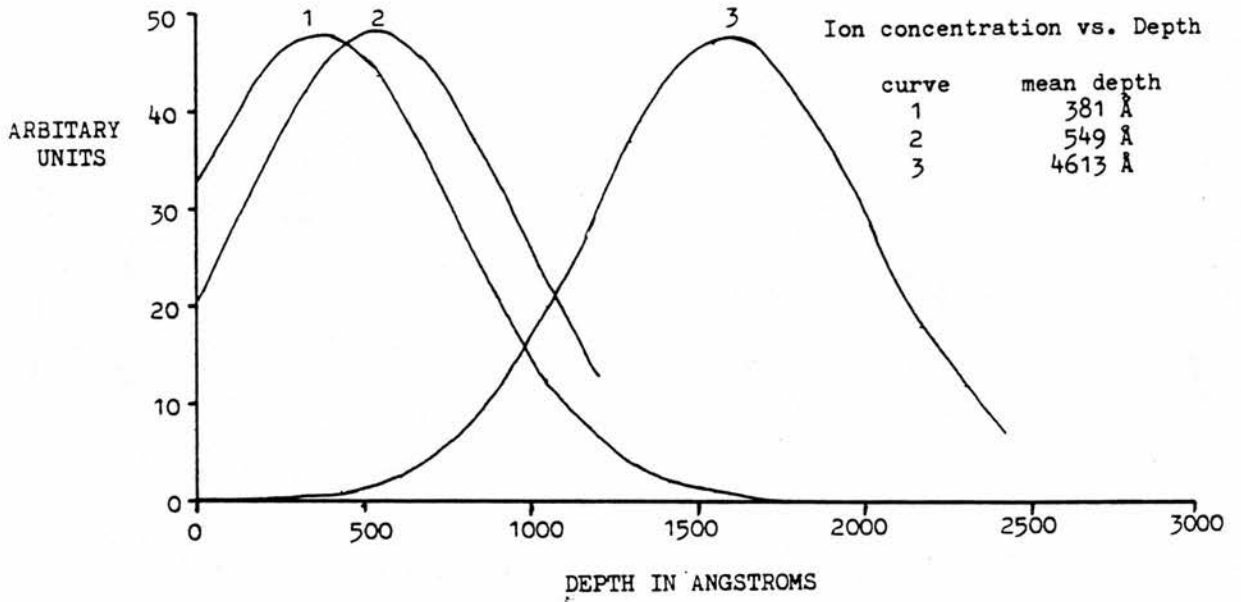
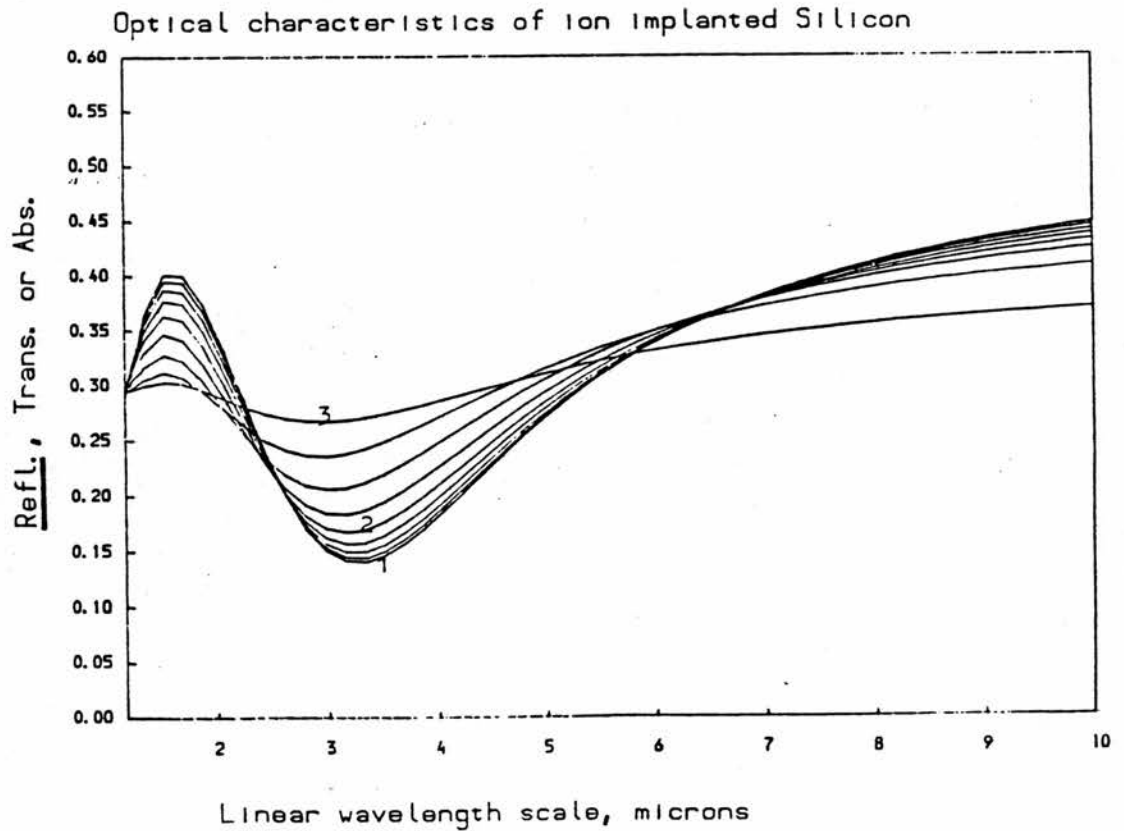
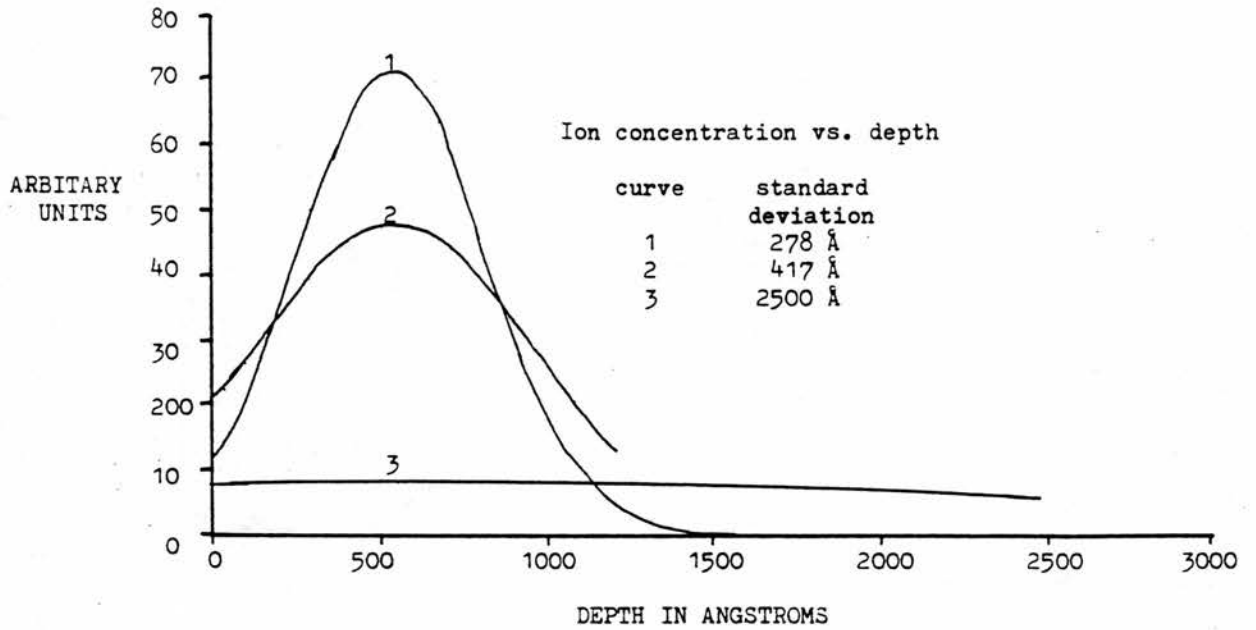


Figure 13 The effect of implant spread on Reflectivity  
Computer predictions



Figures 14, 15, and 16  
Theoretical Plots of Reflectivity, Transmission  
and Absorption for the five implants investigated

Figure 16 Absorption  
Optical characteristics of ion implanted Silicon

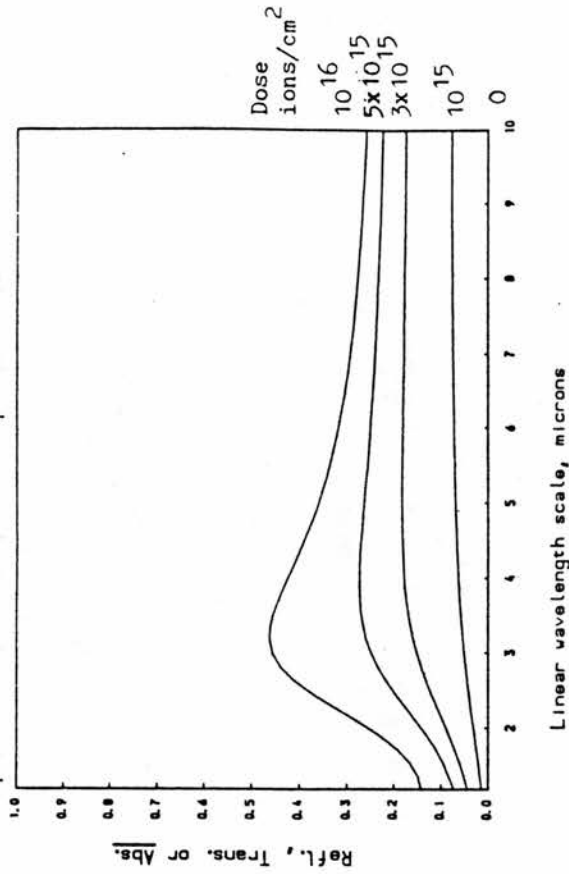


Figure 14 Reflectivity  
Optical characteristics of ion implanted Silicon

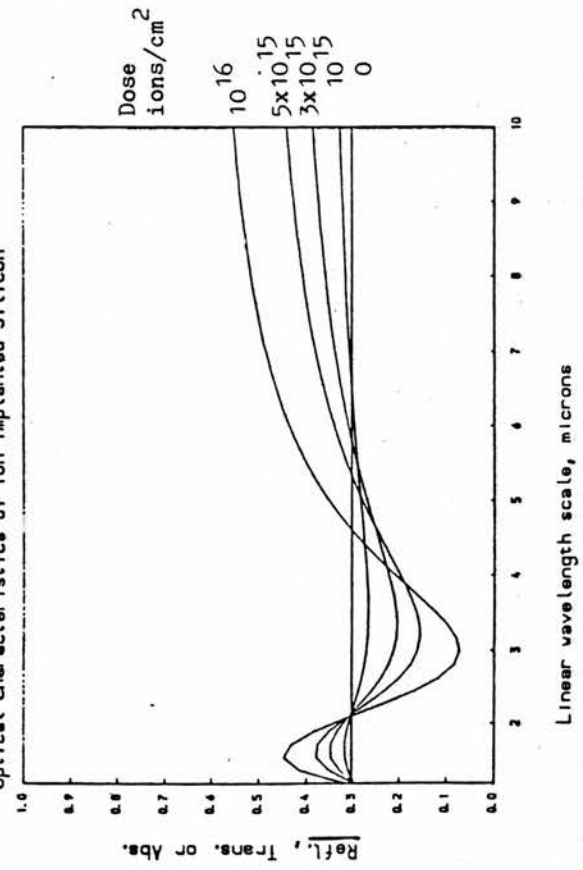
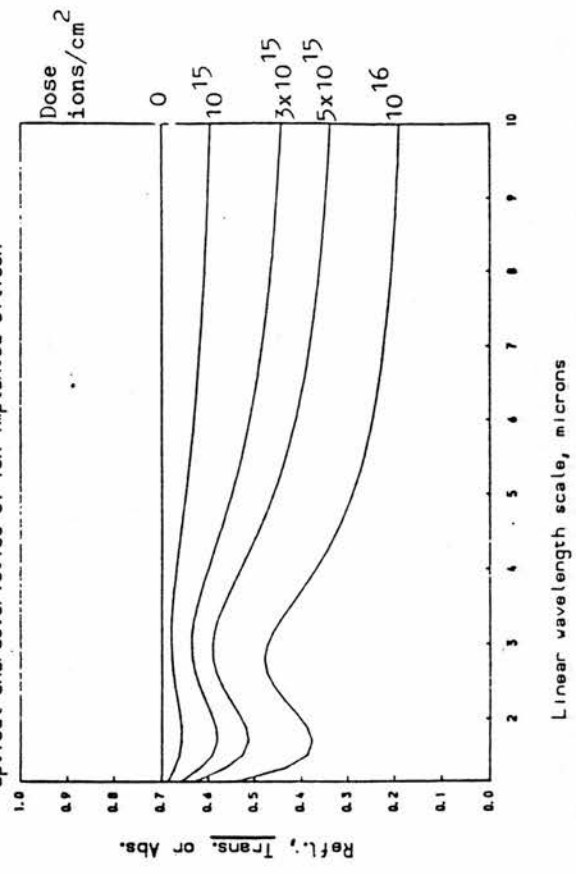


Figure 15 Transmission  
Optical characteristics of ion implanted Silicon



## CHAPTER 3

interference fringes, e.g. Figure 17, the resolution has to be increased accordingly.

Figures 8 to 16 cover the results of the calculations in the 1  $\mu\text{m}$  to 10  $\mu\text{m}$  region. Above 10  $\mu\text{m}$  in the mid- and far-infrared as well as the microwave regions, interference fringes were resolved by the experimental arrangements used (Chapter 4). The calculation takes these into account as described in the paragraph split between page 27 and 28 by treating the wafer as multiple layers, as before, to model the implant with the remainder of the wafer treated as a final much thicker unimplanted layer rather than an infinite substrate.

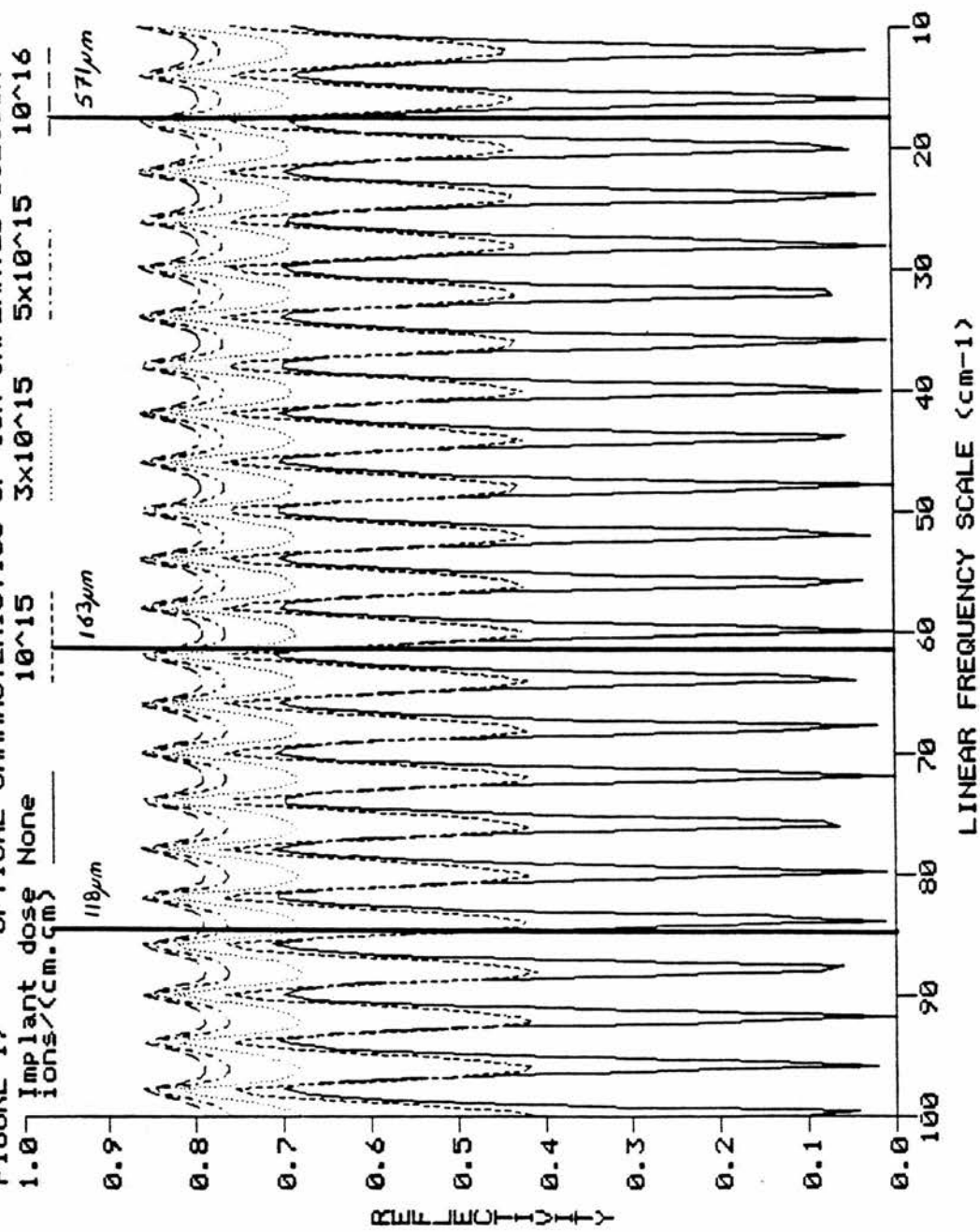
Using the same methods as for the near infrared, the calculations can be extended into the far-infrared and microwave region. The implant depth and distribution has very little effect on the optical properties of the wafer from 100  $\text{cm}^{-1}$  to 0.01  $\text{cm}^{-1}$ , the important parameter is activated dose. To allow direct comparison of the following theoretical results with the experimental results in chapter 5 a cut-off implant concentration is assumed. This is described in detail in chapter five page 50. Also the discrete wavelengths and the microwave frequencies used experimentally are marked on the following figures where appropriate.

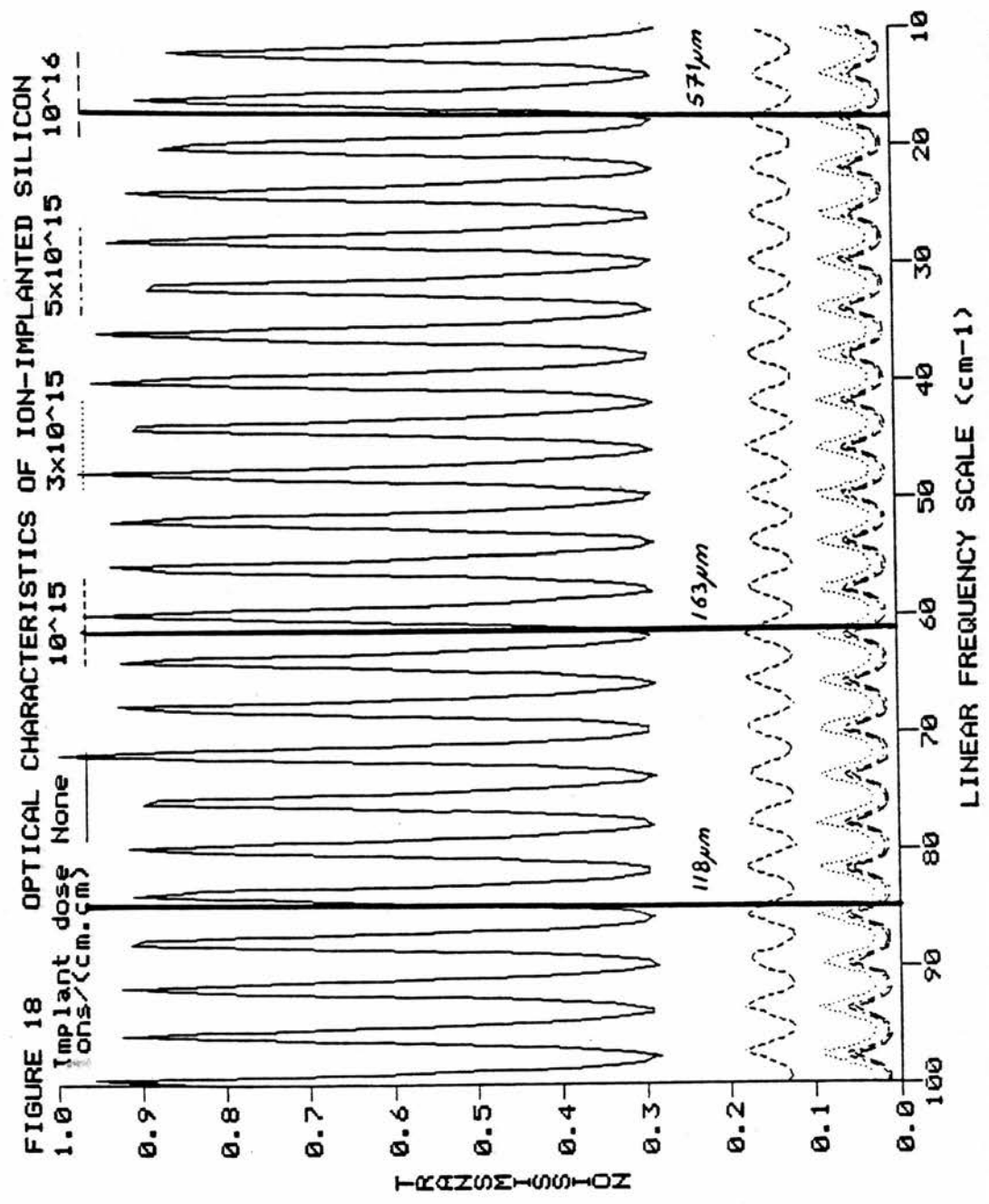
Between 100  $\text{cm}^{-1}$  and 10  $\text{cm}^{-1}$  (figures 17, 18 and 19), the optical characteristics show a periodic variation due to Fabry-Pérot interference.

Figures 20, 21 and 22 show a similar variation for the 10  $\text{cm}^{-1}$  to 1  $\text{cm}^{-1}$  frequency region as for the 100  $\text{cm}^{-1}$  to 10  $\text{cm}^{-1}$  region, however, because only two interference fringes are shown compared to 23 in figures 17, 18 and 19, it is easier to study the 10  $\text{cm}^{-1}$  to 1  $\text{cm}^{-1}$  region.

Figure 22 shows the increase in absorption with doping from un-implanted to  $10^{15}$  ions per  $\text{cm}^2$ . However an increased dose together with the high surface conductivity allows the

FIGURE 17 OPTICAL CHARACTERISTICS OF ION-IMPLANTED SILICON





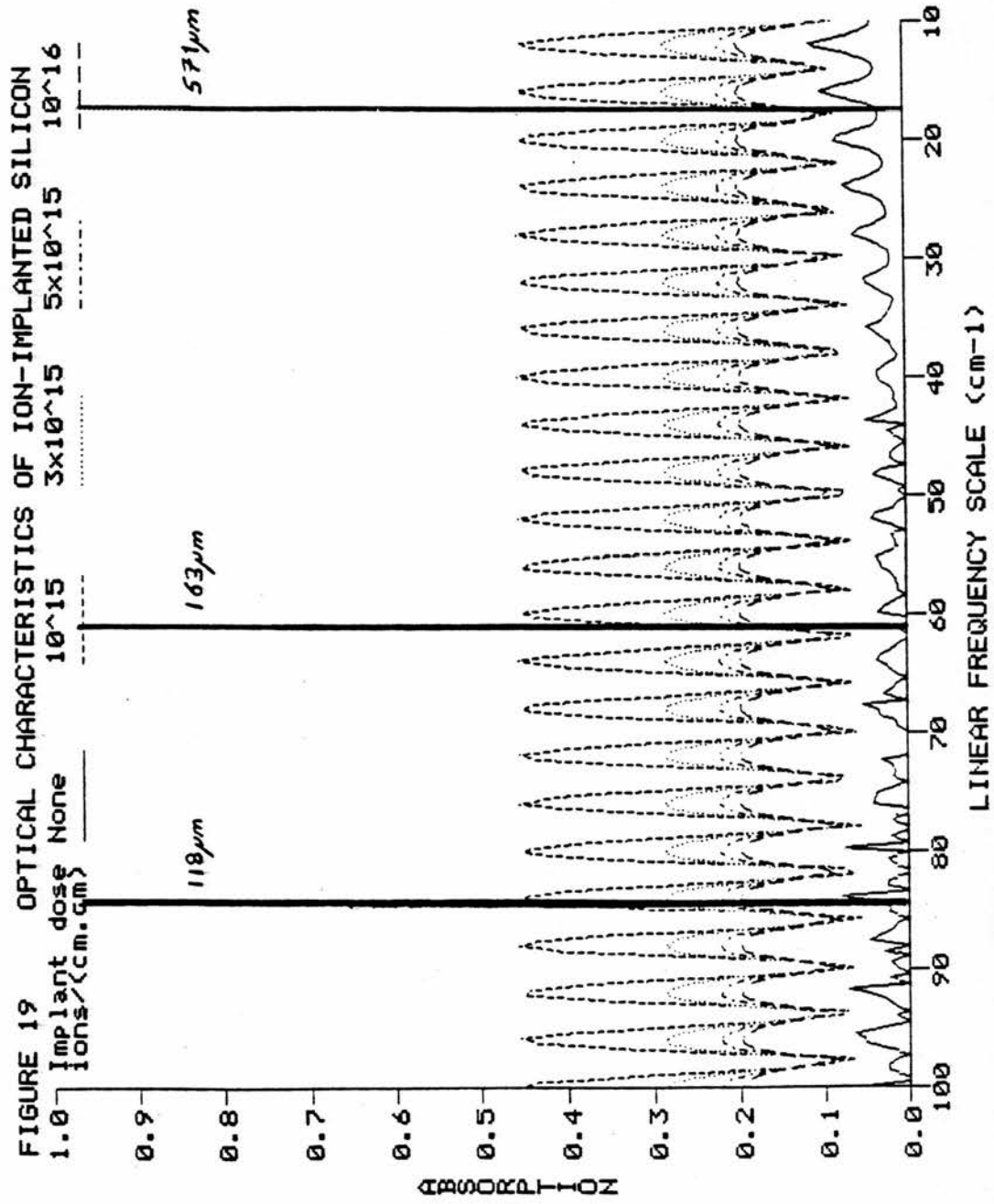


FIGURE 20 OPTICAL CHARACTERISTICS OF ION-IMPLANTED SILICON

Implant dose None  $10^{15}$   $3 \times 10^{15}$   $5 \times 10^{15}$   $10^{16}$   
 ions/(cm.cm) \_\_\_\_\_

95 GHz

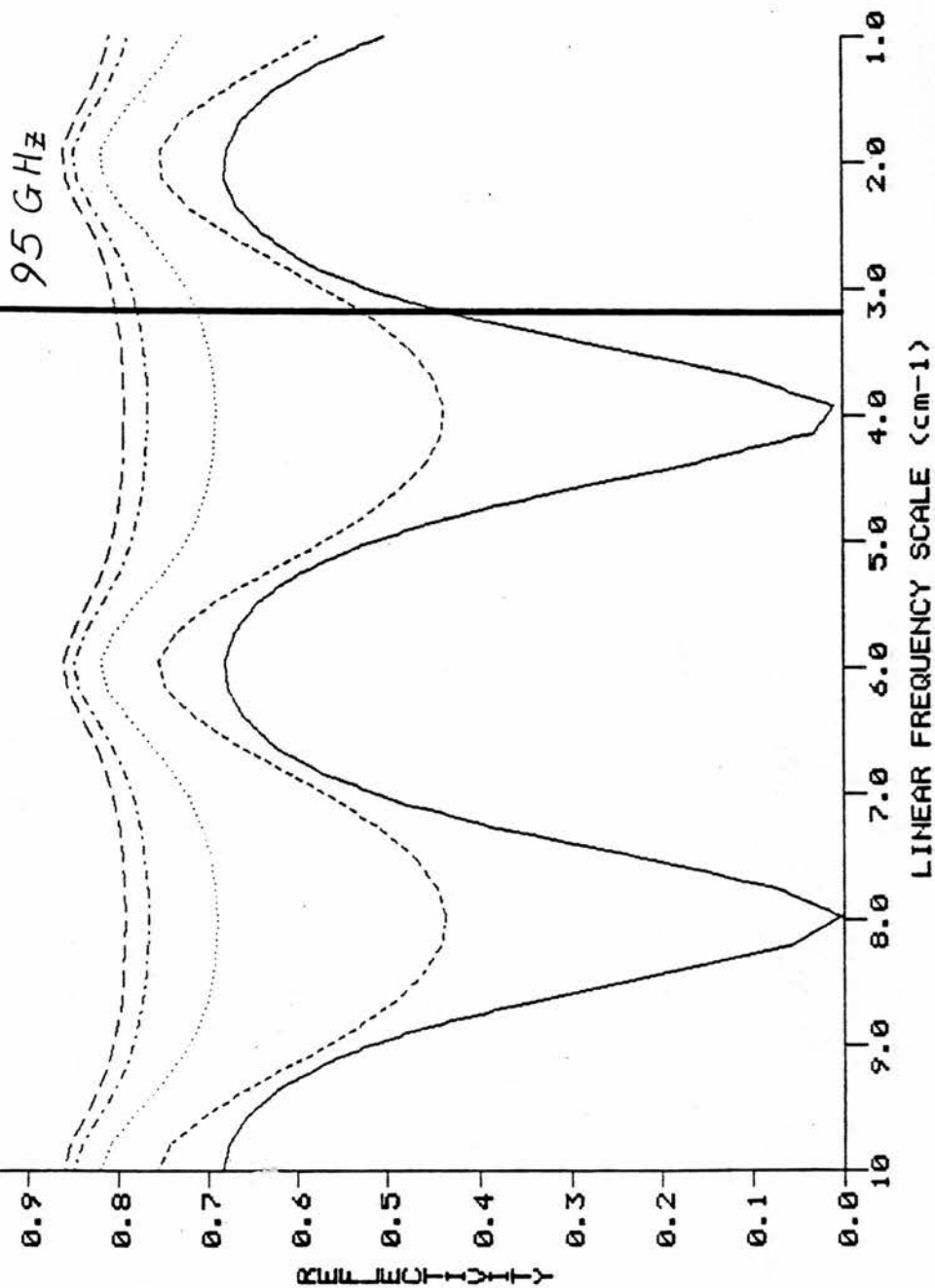


FIGURE 21 OPTICAL CHARACTERISTICS OF ION-IMPLANTED SILICON

Implant dose ions/(cm.cm)	None	$10^{15}$	$3 \times 10^{15}$	$5 \times 10^{15}$	$10^{16}$
Line Style	—	---	.....	----	----

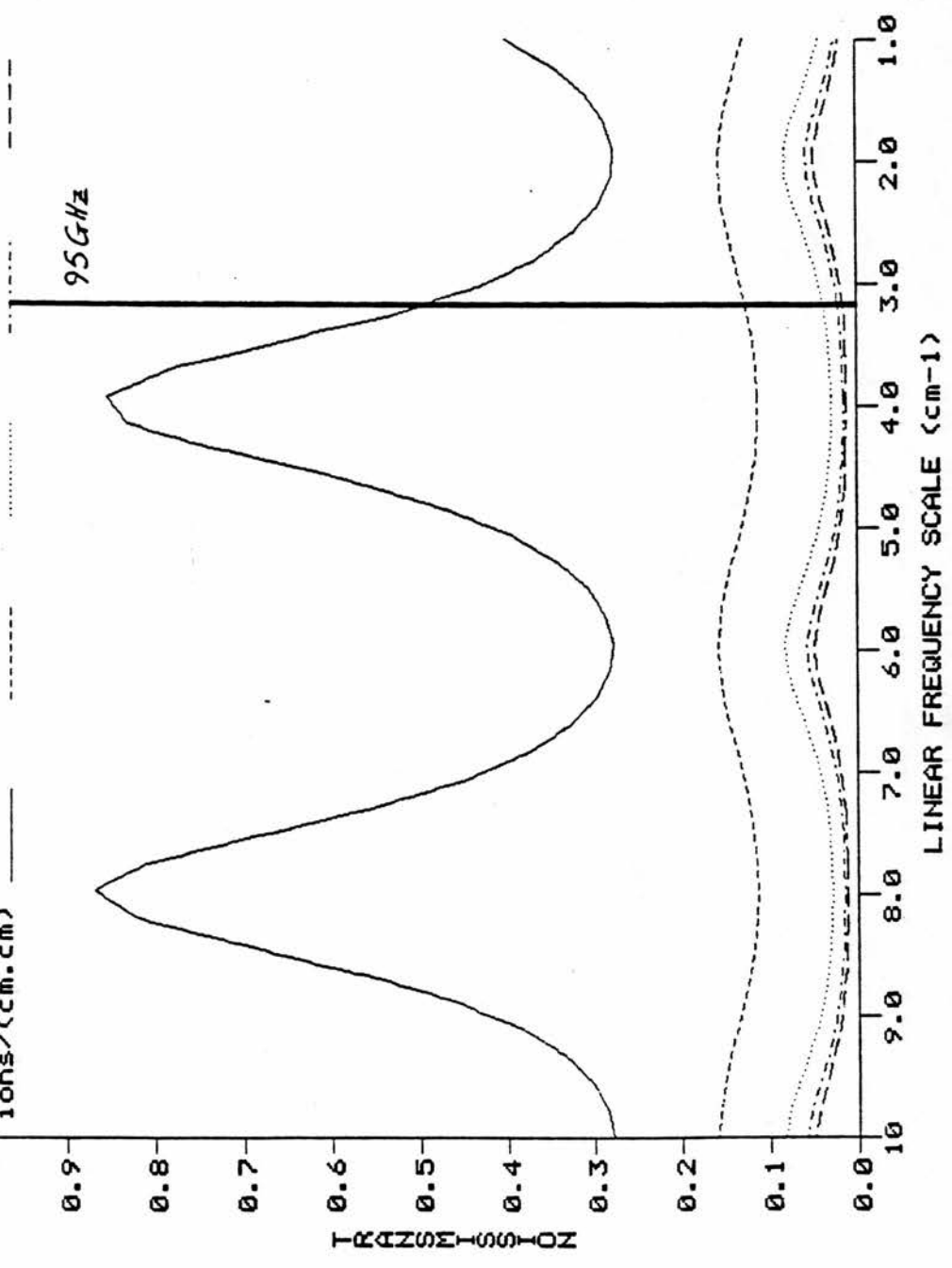
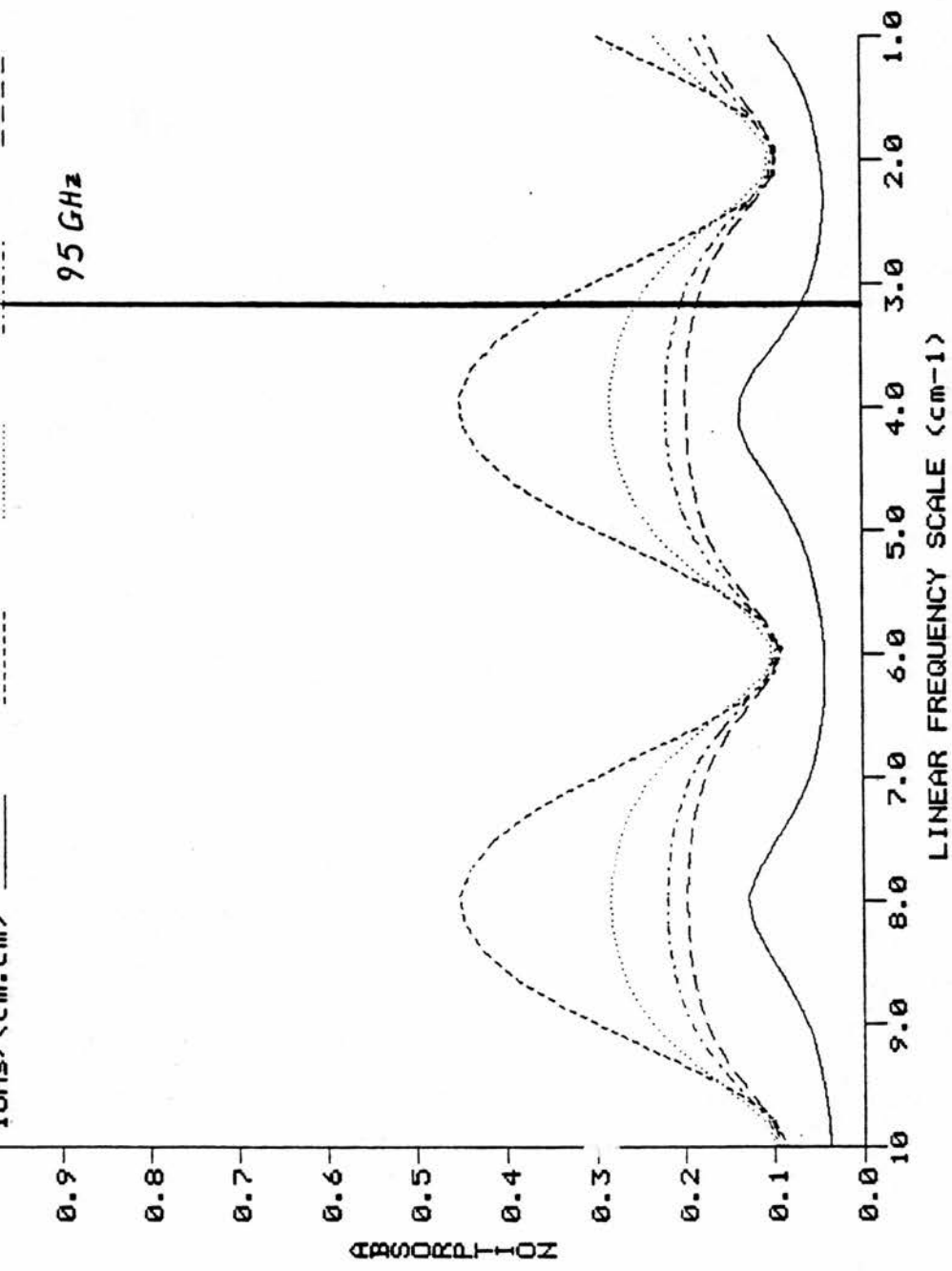


FIGURE 22 OPTICAL CHARACTERISTICS OF ION-IMPLANTED SILICON  
 Implant dose None  $10^{15}$   $3 \times 10^{15}$   $5 \times 10^{15}$   $10^{16}$   
 ions/(cm<sup>2</sup>)



## CHAPTER 3

reflectivity to continue to increase (figure 20) causing the net absorption to fall. The increasing then decreasing absorption and the increasing reflectance with dose shows as a phase change in the transmission spectra (figure 21), with high dose (greater than  $10^{15}$  ions per  $\text{cm}^2$ ) giving modulation in transmission  $180^\circ$  out of phase with the lower dose implants.

Between  $1 \text{ cm}^{-1}$  to  $0.1 \text{ cm}^{-1}$ ,  $1 \text{ cm}$  to  $10 \text{ cm}$  wavelength (figures 23, 24 and 25), one is on the long wavelength side of the 'last' interference fringe and the optical characteristics are approaching their low frequency values. The calculation in the  $10 \text{ cm}$  to  $1 \text{ m}$  region shows that the ion-implanted layer still has a considerable effect, but this is unchanging with frequency (figures 26, 27 and 28).

From these calculations it appears that in the  $1 \mu\text{m}$  to  $10 \mu\text{m}$  region, reflectivity and transmission provide the best contactless probe to determine implanted ion distribution.

Measurement in the far-infrared and microwave region provides an accurate assessment of the total implanted ion dose. Using a reflectivity trough (figure 17) or a transmission peak (figure 18), sensitivity over implant doses less than  $3 \times 10^{15}$  ions per  $\text{cm}^2$  is achieved. A reflectivity trough will also provide more accuracy in the higher implant dose region. As seen in other work [15,16], the interference fringes enhance the effects of changes in optical properties.

The millimeter and centimeter regions will provide the low dose discrimination (down to  $10^{14}$  implanted ions/ $\text{cm}^2$ ). Figure 24 at  $0.33 \text{ cm}^{-1}$  shows a change in transmission from 11% to 0% as the implant dose changes from  $10^{15}$  ions/ $\text{cm}^2$  to unimplanted.

The criteria used to determine which measurements will be most sensitive in distinguishing implant dose involves looking at the percentage changes in reflectance or transmission - the larger the percentage change, the higher the accuracy.

FIGURE 23 OPTICAL CHARACTERISTICS OF ION-IMPLANTED SILICON  
 Implant dose None  $10^{15}$   $3 \times 10^{15}$   $5 \times 10^{15}$   $10^{16}$   
 ions/(cm.cm)

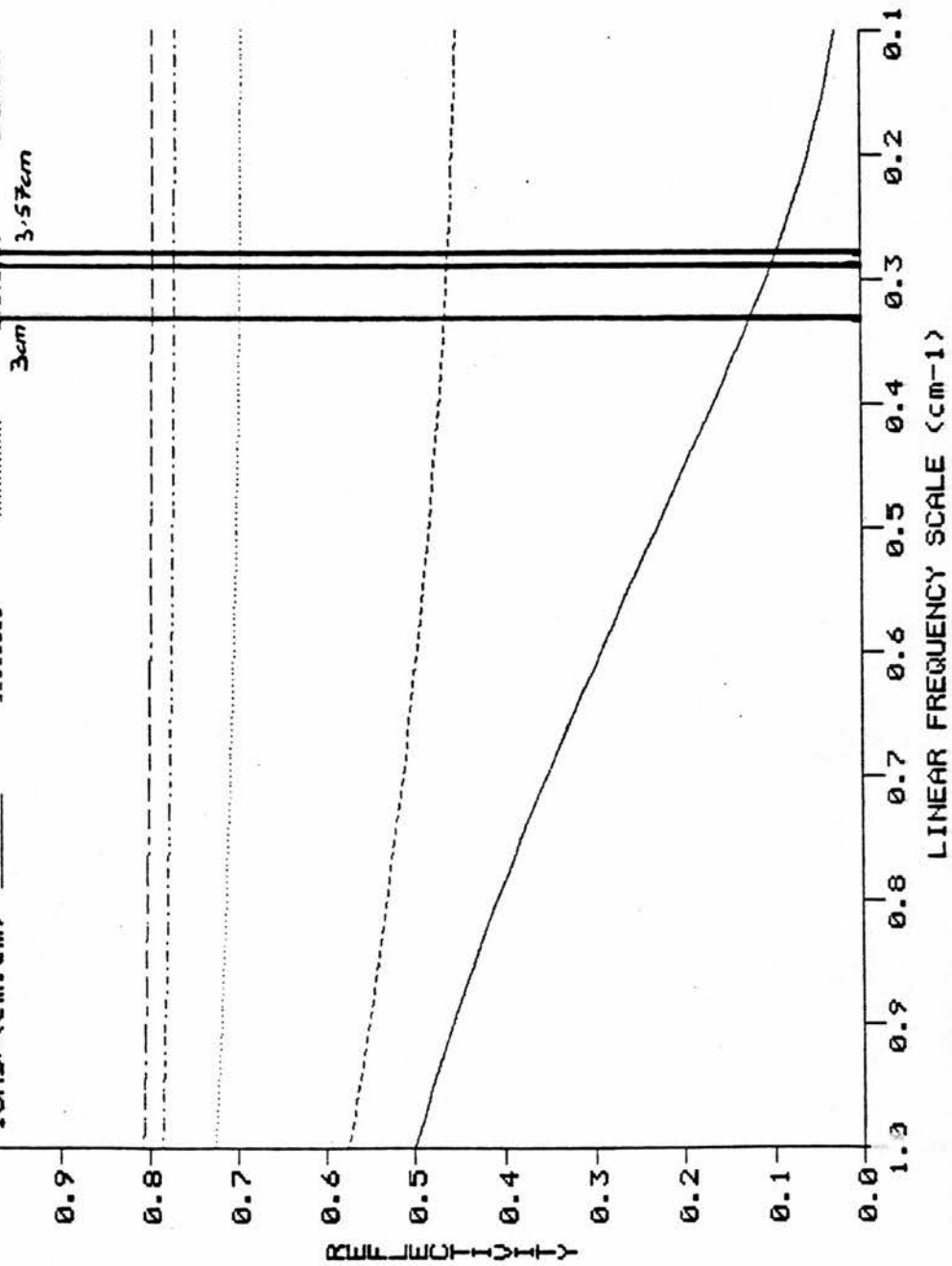


FIGURE 24 OPTICAL CHARACTERISTICS OF ION-IMPLANTED SILICON

Implant dose None  $10^{15}$   $3 \times 10^{15}$   $5 \times 10^{15}$   $10^{16}$  ions/(cm.cm)

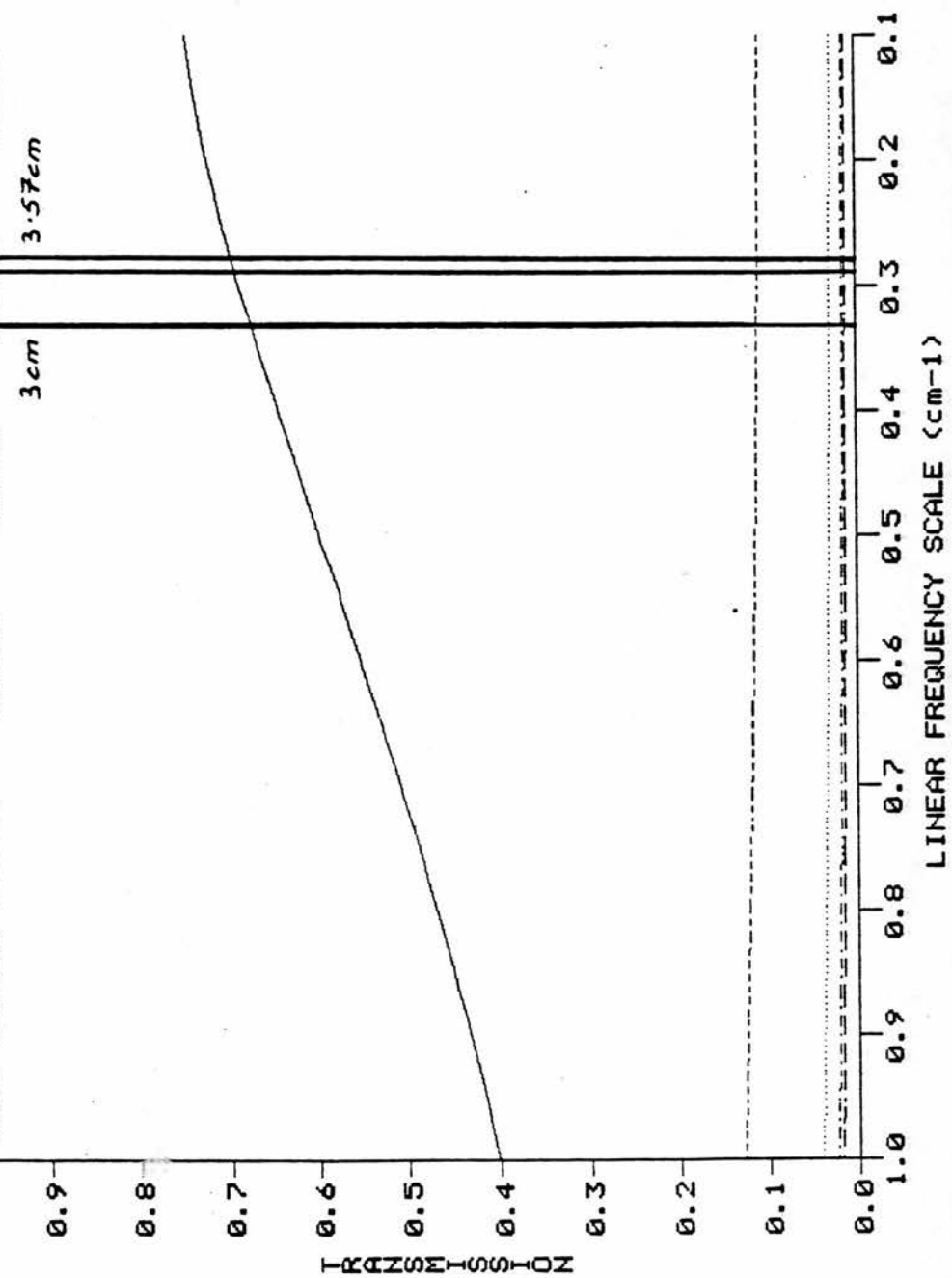


FIGURE 25 OPTICAL CHARACTERISTICS OF ION-IMPLANTED SILICON  
 1.0 Implant dose None  
 ions/(cm.cm) \_\_\_\_\_

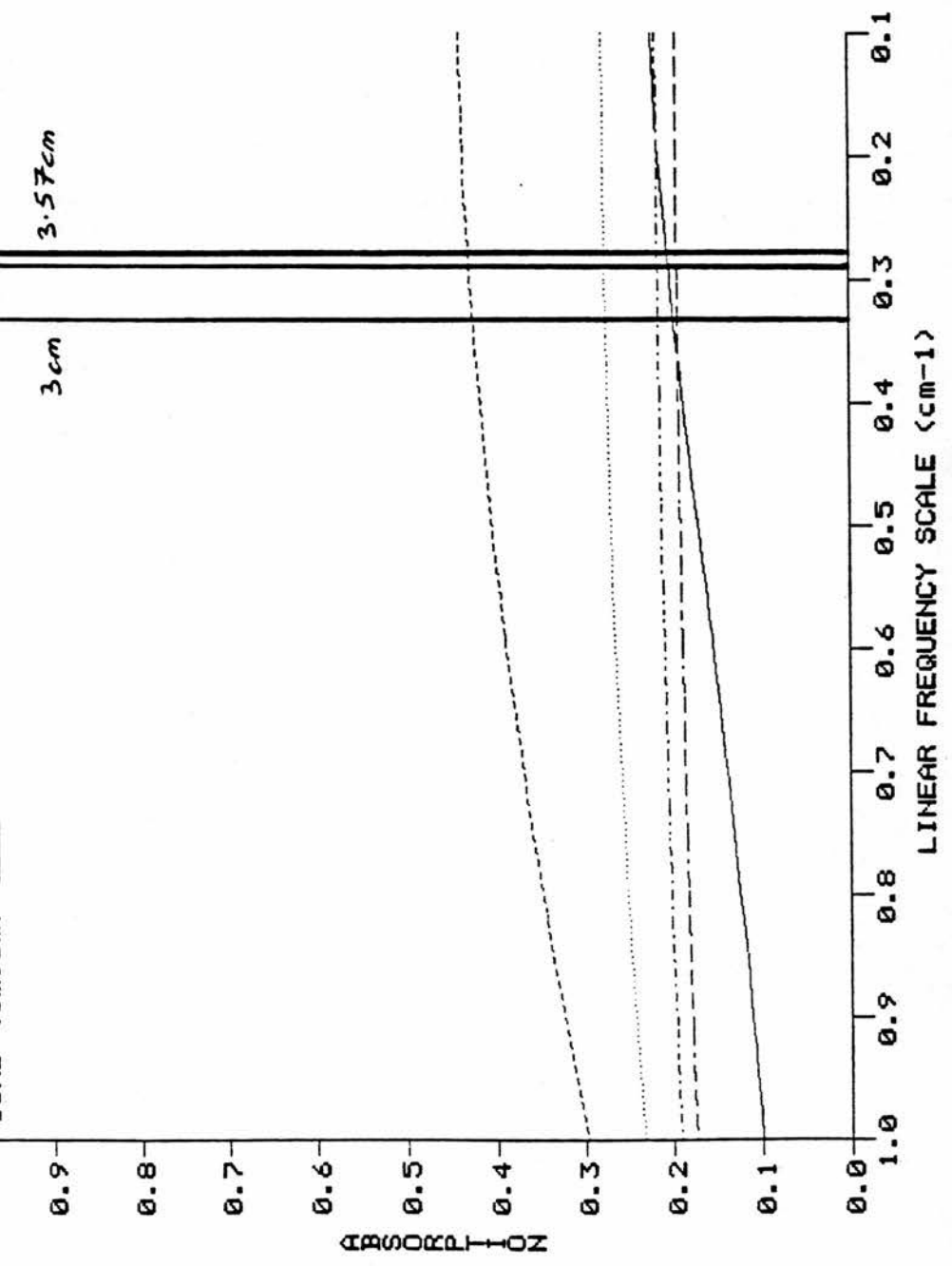


FIGURE 26 OPTICAL CHARACTERISTICS OF ION-IMPLANTED SILICON

Implant dose ions/cm <sup>2</sup>	None	10 <sup>15</sup>	3x10 <sup>15</sup>	5x10 <sup>15</sup>	10 <sup>16</sup>
Line Style	—	- - - - -	.....	- - - - -	- - - - -

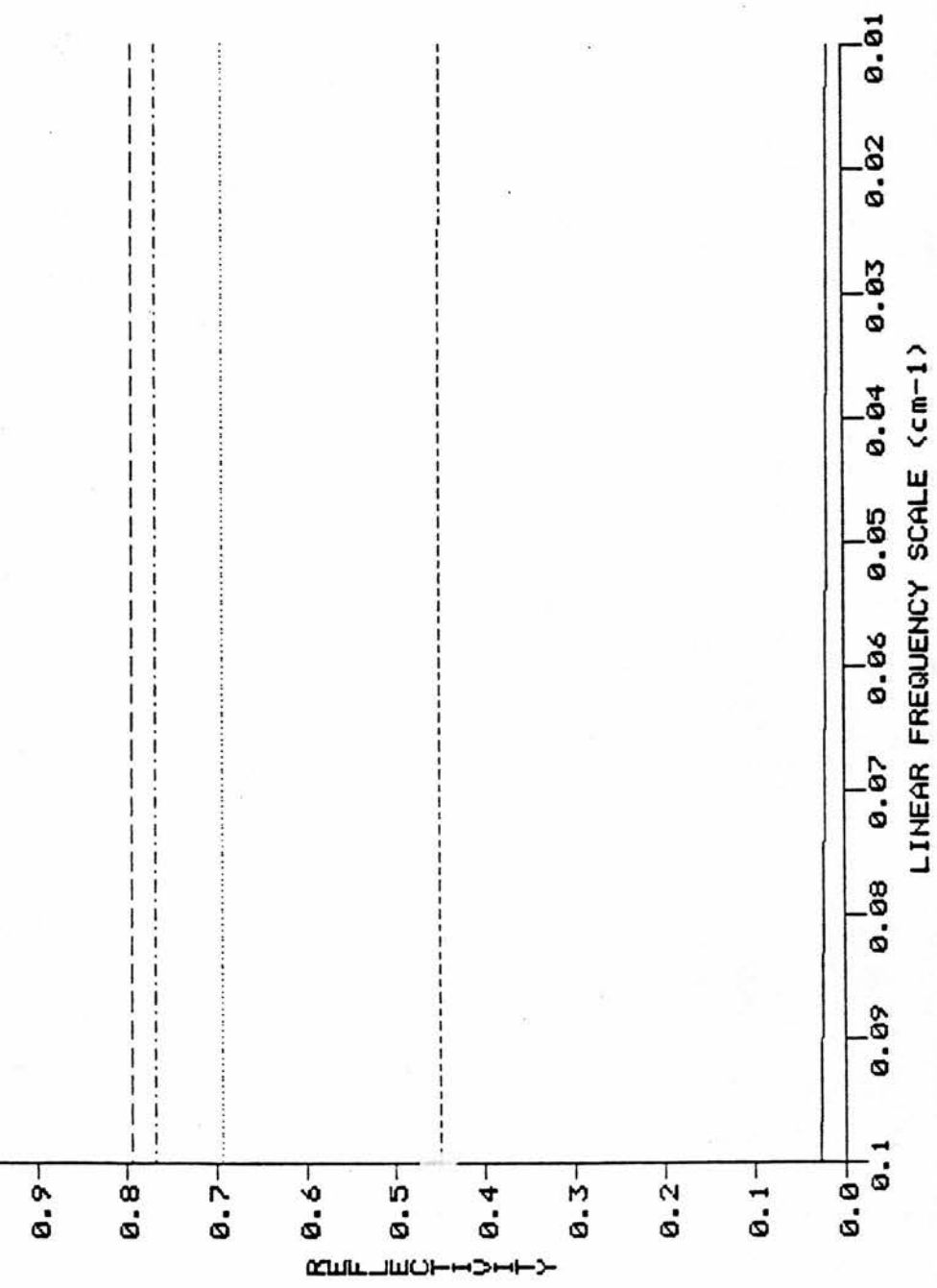


FIGURE 27 OPTICAL CHARACTERISTICS OF ION-IMPLANTED SILICON

Implant dose None  $10^{15}$   $3 \times 10^{15}$   $5 \times 10^{15}$   $10^{16}$   
 ions/(cm.cm) \_\_\_\_\_

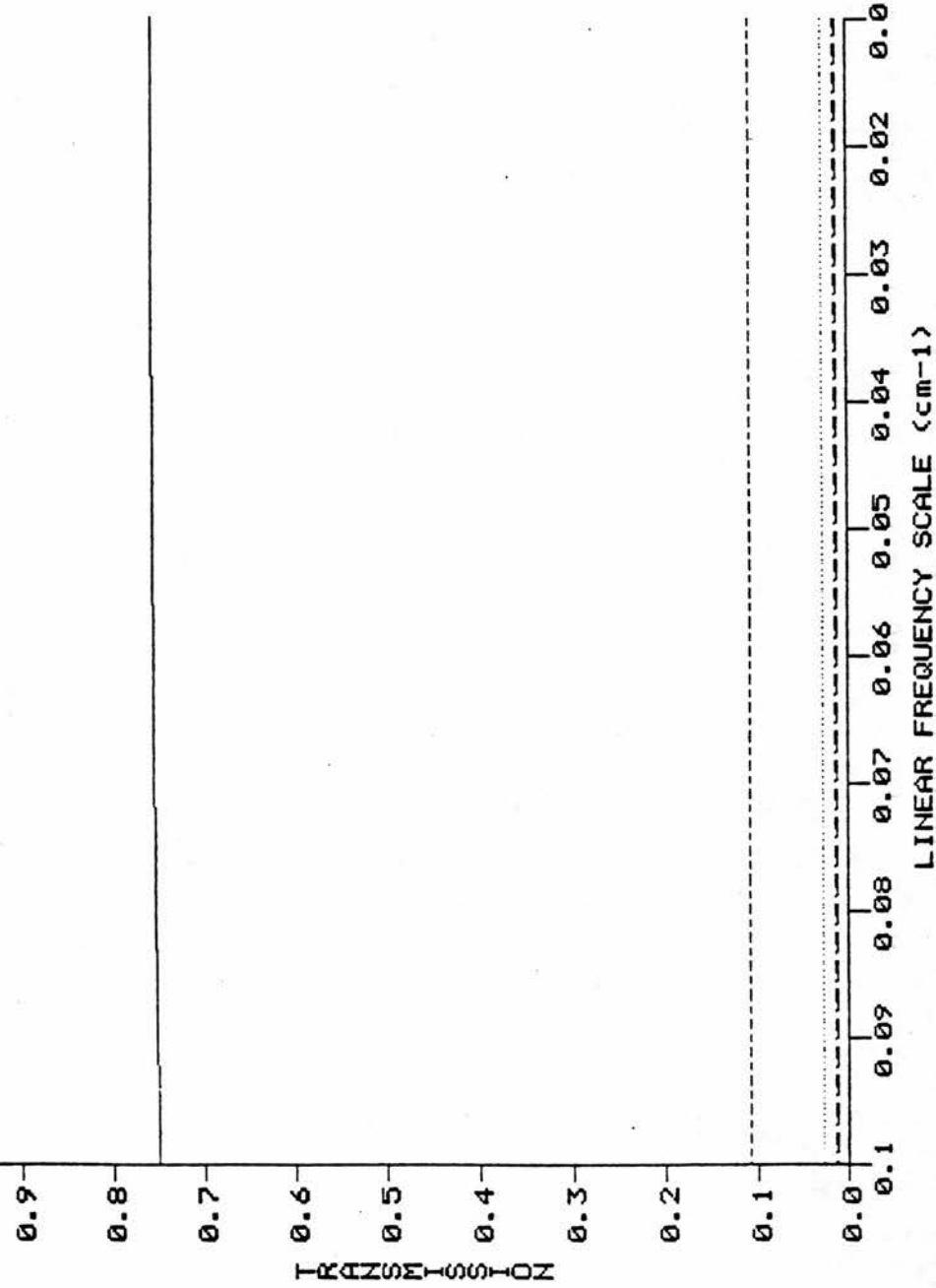
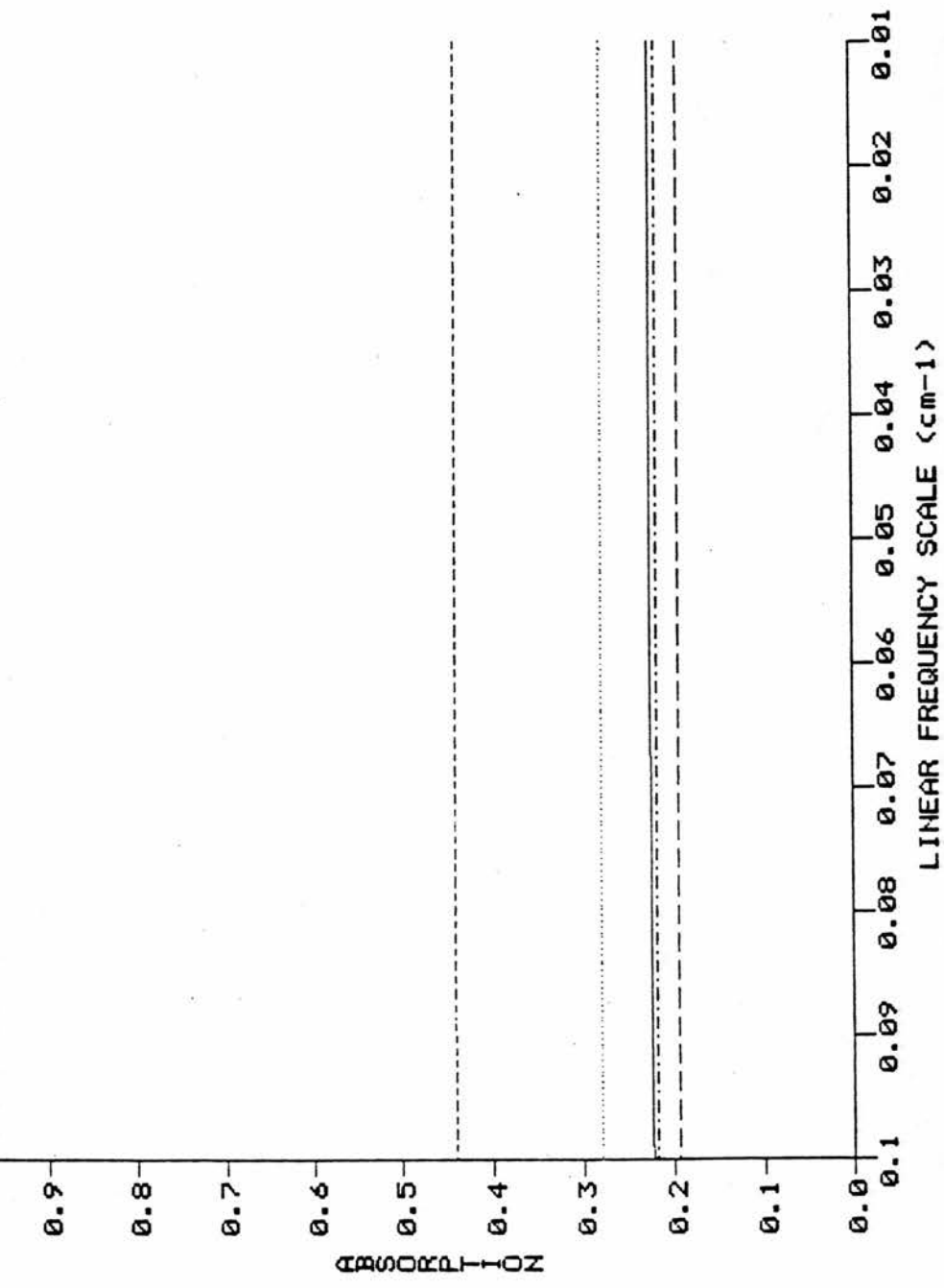


FIGURE 28 OPTICAL CHARACTERISTICS OF ION-IMPLANTED SILICON

Implant dose ions/cm <sup>2</sup>	None	10 <sup>15</sup>	3x10 <sup>15</sup>	5x10 <sup>15</sup>	10 <sup>16</sup>
Line Style	_____	-----	.....	-----	-----



EXPERIMENTAL TECHNIQUES

Five different techniques were used to cover the reflective and transmissive properties of the ion-implanted silicon wafers over the spectral region  $2 \mu\text{m}$  to  $3.5 \text{ cm}$ .

The ultimate aim of these experiments is to allow the contactless characterisation of ion-implanted silicon by measuring the optical properties throughout the infrared, far-infrared and microwave region of the spectrum. Then to fit a predicted curve, using the computational techniques developed in Chapters 2 and 3 to the experimental data, using the implant profile as the fitting variable.

 $2 \mu\text{m}$  to  $8 \mu\text{m}$  (Figure 29)

Over this region radiation from an Oriel heated filament source, chopped at 25 Hz, either reflected from the ion-implanted surface or transmitted through the ion-implanted wafer was passed through a  $4 \mu\text{m}$  blazed grating spectrometer. The output of the spectrometer was incident upon a diamond windowed golay detector.

The signal from the golay detector, together with the chopper reference signal, was processed by a Brookdeal 9501E lock-in amplifier. This output was plotted on an x-t recorder (where the linear scan rate with time leads to an x- $\lambda$  plot) as well as being digitised by a Datron digital voltmeter.

The digital voltmeter was triggered by the same square wave signal which controlled the stepper motor drive to the blazed grating. The digital voltmeter signal was then stored on computer.

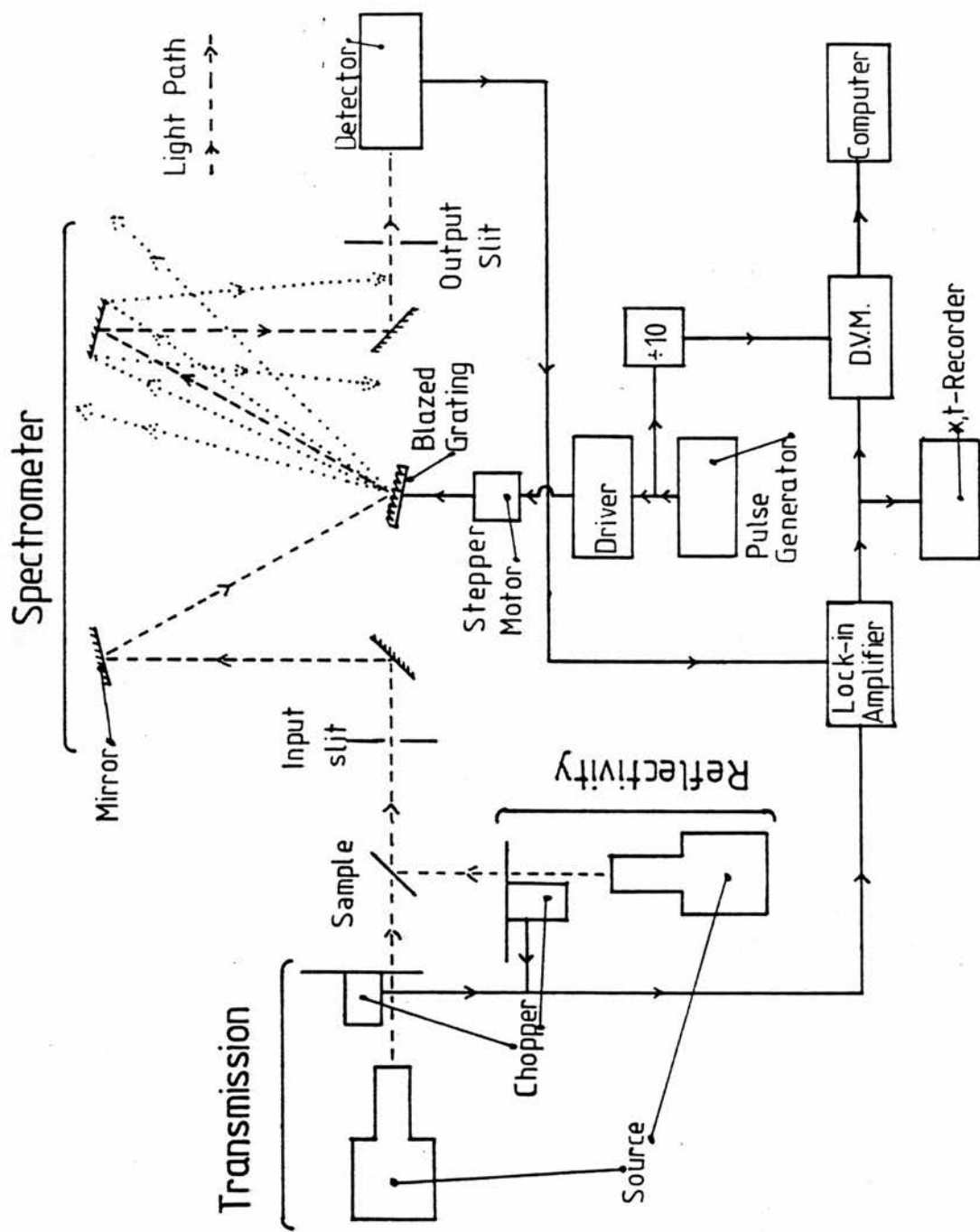


Figure 29 Grating Spectrometer

Calibration (Figure 30)

The angle of the blazed grating in the spectrometer was micrometre controlled. The large solid curve in figure 30 represents the grating spectrometer transmission without a sample vs. the micrometre reading.

To calibrate the grating spectrometer micrometre reading in wavelength, two filters (InAs and InSb) and a chloroform filled quartz microcell were used. The three inserts in figure 30 show the response of the filters and chloroform, vs. wavelength, when inserted into the system. The dashed curves on the grating spectrometer response characteristic show the effect of the three calibrated samples.

The InSb filter has 5% transmission at 7.3  $\mu\text{m}$  and this corresponds to a micrometre reading of 4260. The InAs filter has 5% transmission at 3.6  $\mu\text{m}$  and this corresponds to a micrometre reading of 2120. The chloroform transmission spectrum has absorptions at 3.3  $\mu\text{m}$  and 4.1  $\mu\text{m}$ . The 3.3  $\mu\text{m}$  absorption corresponds to 1970 and the 4.1  $\mu\text{m}$  absorption to 2490.

The four results give a calibration of

$$\text{wavelength } (\mu\text{m}) = (\text{micrometre reading} - 90) / 570$$

Sample Preparation

Hughes Microelectronics Ltd. in Glenrothes were the sponsoring body in my SERC CASE award. I was given every assistance by Hughes to prepare six silicon wafers. These were ion-implanted by me and the implantation details are given in table 1. All the wafers were heavily implanted at high energies, three with boron and three with phosphorous.

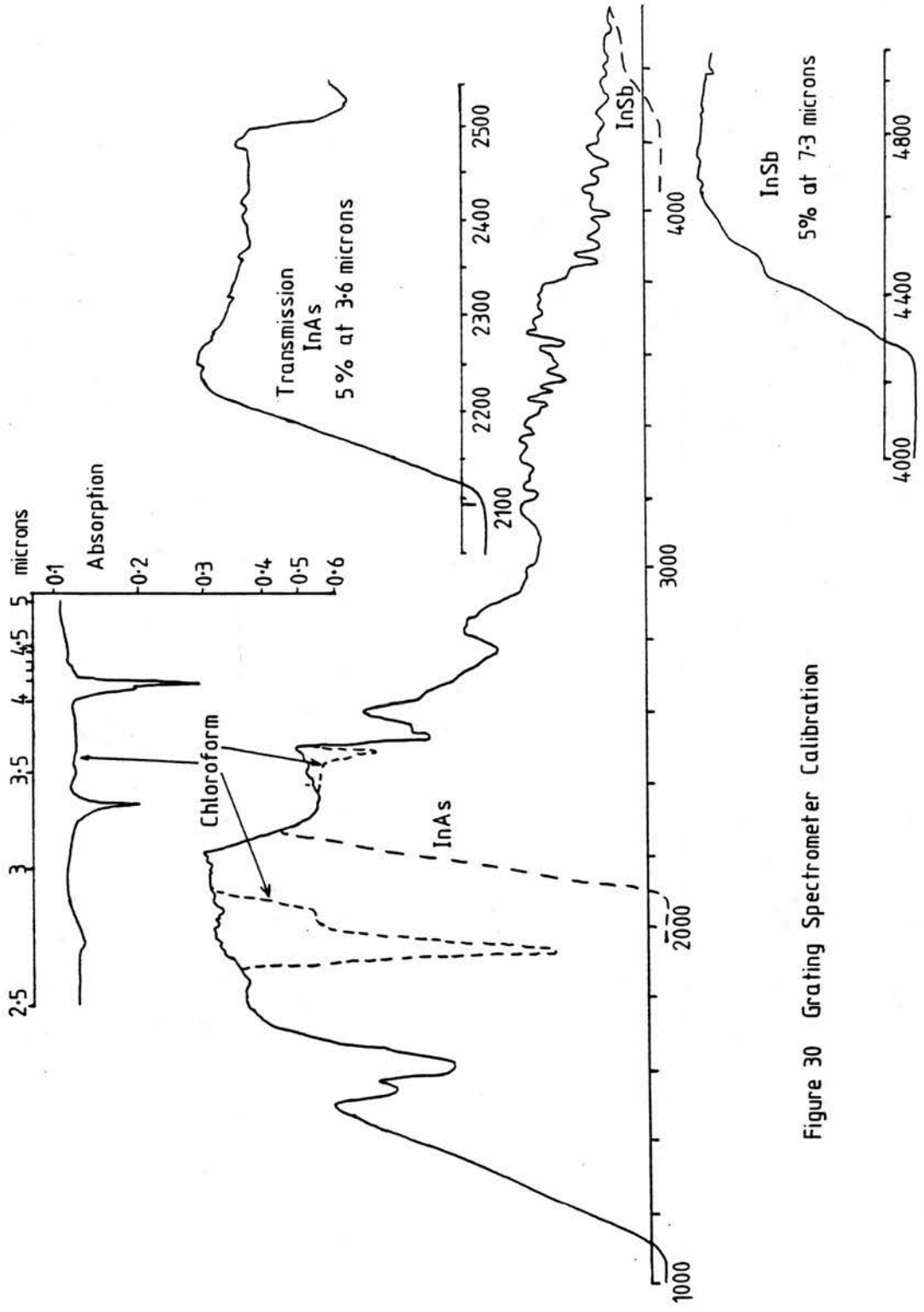


Figure 30 Grating Spectrometer Calibration

CHAPTER 4

TABLE 1

Wafer number	Implant at 180 KeV N <sup>o</sup> . of ions/cm <sup>2</sup>	Type of implant
1	10 <sup>16</sup>	Phosphorous
2	10 <sup>15</sup>	Phosphorous
3	10 <sup>14</sup>	Phosphorous
4	10 <sup>16</sup>	Boron
5	10 <sup>15</sup>	Boron
6	10 <sup>14</sup>	Boron

Other details

The wafers are all 19  $\Omega$  cm p-type <100> 3" diameter silicon about 350  $\mu$ m thick. All the wafers were processed using the standard technology of Hughes Microelectronics Limited. First a 700  $\text{\AA}$  oxide coat was grown over the wafer surface to avoid channelling during the implantation and to retain the implant on annealing. After ion-implantation the wafers were annealed at 950 °C for 20 minutes in a nitrogen atmosphere to activate the implants, see chapter 1 page 13.

The reflectivity vs. wavelength plots from these samples are discussed in chapter 5 page 42.

A further set of six wafers were implanted by me at Hughes Microelectronics Limited using phosphorous only. The implantation details are given in table 2.

## CHAPTER 4

TABLE 2

Wafer number	Implant at 180 KeV N <sup>o</sup> . of ions/cm <sup>2</sup>	Type of implant
7	10 <sup>16</sup>	Phosphorous
8	5x10 <sup>15</sup>	Phosphorous
9	3x10 <sup>15</sup>	Phosphorous
10	10 <sup>15</sup>	Phosphorous
11	no implant	none
12	blank wafer	control

Other details

The same wafer types as before were used, and once again a 700 Å oxide layer was first grown over all the wafers except N<sup>o</sup>. 12. Wafer 11 was loaded into the ion-implanter but not implanted. Annealing took place for all the wafers except N<sup>o</sup>. 12 at 950 °C for 20 minutes in a nitrogen atmosphere. The oxide was then removed from half of each wafer by dipping in 5:1 hydrofluoric acid followed by a de-ionised water rinse.

Wafer 12 came from the same batch as the others but was kept aside to act as a control for wafer 11 which went through all the processing steps apart from being implanted.

The above implantation doses provided several more concentration steps over the experimentally sensitive region, as well as allowing the effect of a thick oxide layer on reflectivity and transmission to be assessed.

The reflectivity vs. wavelength plots from these samples are discussed in chapter 5 page 42.

Further Near Infrared Experiments

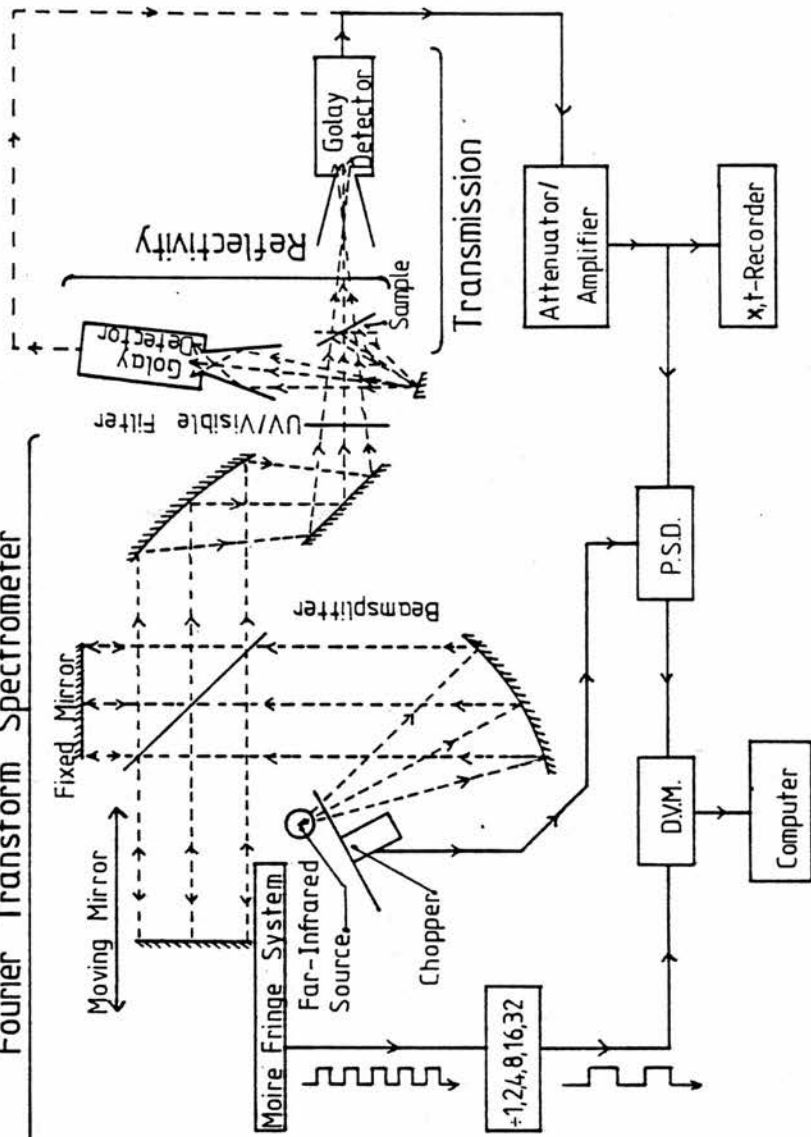
Only the near infrared measurements provide the information required to determine the distribution of activated implanted ions with depth. In order to test the effectiveness of the experimental procedures developed earlier in measuring the implant profile, measurements were made with two samples provided by Dr. A.G.O'Neill of Plessey Research Caswell. The silicon wafers were ion-implanted with arsenic then annealed. Half of each wafer was kept and profiled by Plessey using stripping measurements. Sample MSO61/TP4 was implanted at 30 KeV with a dose of  $3.9 \times 10^{15}$  ions/cm<sup>2</sup> then annealed for 30 minutes in Argon at 950°C. Sample MSO38/1 was implanted with a dose of  $10^{15}$  ions/cm<sup>2</sup> then annealed for 25 minutes in nitrogen/2% oxygen at 1000°C, the implant energy is unknown.

Near infrared spectra of each sample were taken and the experimental reflectivity results matched theoretically. This provided a predicted value of the implant concentration and distribution with depth. The implant was performed by Plessey, so the parameters used to predict the reflectivity were different from those used for the Hughes Microelectronics implants. The reflectance results for these samples are shown in chapter 5 page 45

12.5  $\mu$ m to 1 mm Techniques (Figure 31)

A Beckman Fourier transform spectrometer with a quartz ultra-violet lamp as the far-infrared source, chopped at  $16\frac{2}{3}$  Hz, and a diamond windowed Golay detector were used to determine the ion-implanted wafers transmission and reflection characteristics in the far-infrared. Black polyethene was used to block the ultra-violet, visible and near infrared radiation from the source. The spectrometer was evacuated to remove any water vapour absorptions.

Figure 31 Fourier Transform Spectrometer



## CHAPTER 4

A 1 cm x 1 cm square was cut from each wafer, and for reflectivity measurements mounted at an angle to a copper support. This avoids any extra power entering the detector by reflection from the support itself. The reflected background was taken using a gold plated mirror. For transmission measurements, the remaining wafer was mounted over a 1 cm<sup>2</sup> hole in aluminium foil.

The Golay signal was first attenuated or amplified before being passed to a phase sensitive detector referenced from the 16<sup>2</sup>/<sub>3</sub> Hz chopper. The output from the phase sensitive detector was plotted by an x-t recorder and digitised by a Datron digital voltmeter to be stored on computer. The digital voltmeter was triggered from the Fourier transform spectrometer's own electronics.

The computer was programmed to perform a fast Fourier transform on the data and to plot the resultant spectrum of intensity vs. frequency (in cm<sup>-1</sup>). Due to the nature of the computer fast Fourier transform, no absolute intensity values were obtained. In order to allow comparisons between wafers, a measure of the absolute intensity is required. This was obtained by removing any attenuation or amplification and noting the phase sensitive detector's output level well away from the spectrometer mirror's zero path difference.

The far-infrared results on the second batch of ion-implanted wafers are presented in chapter five page 46.

Discrete Far-Infrared Measurements (Figure 32)

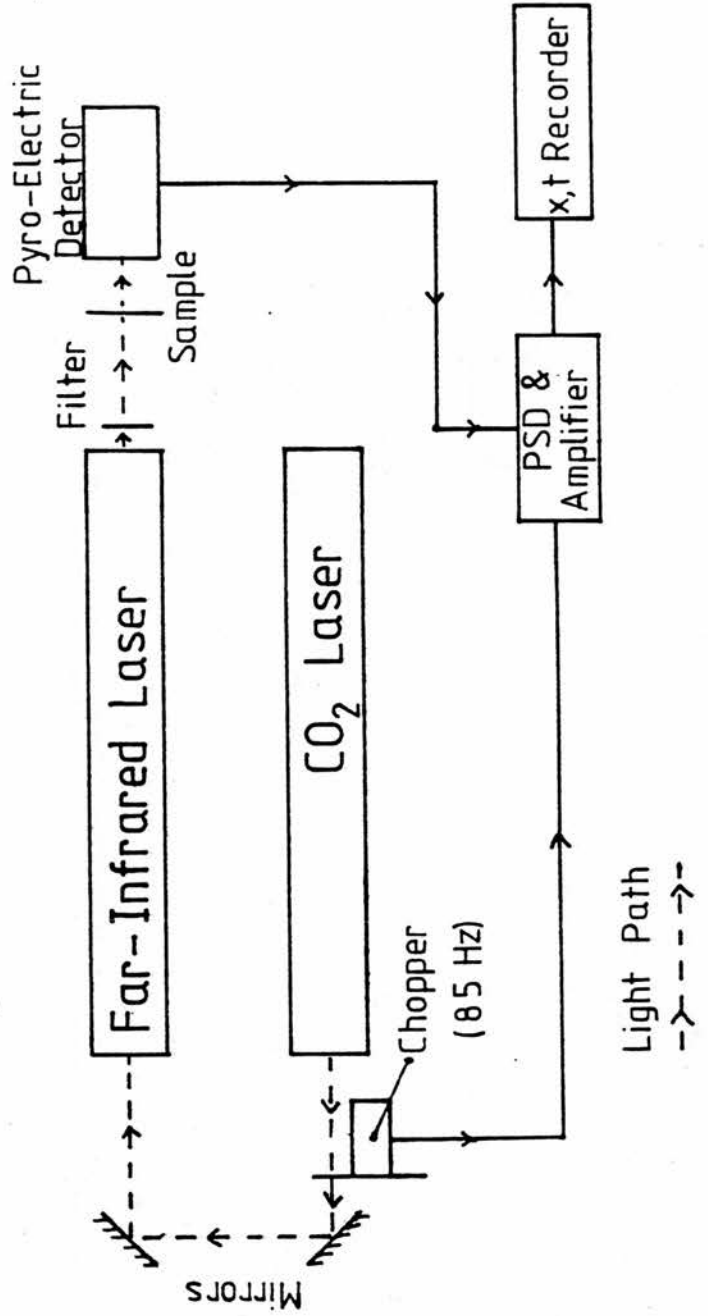
For a rapid evaluation of wafers in a production plant measurement of transmission or reflection at a single wavelength may be preferable to the lengthy collection of data required for a complete wavelength or frequency scan. In order to determine the potential of such a simple test system measurements were made with a number of monochromatic sources in the far-infrared and microwave regions.

-----

A CO<sub>2</sub> infrared laser was chopped at 85 Hz, and used to pump a far-infrared laser cavity filled with methanol to provide discrete wavelengths at 118 μm, 163 μm and 571 μm. The laser was filtered through PTFE to remove any residual 10.6 μm from the CO<sub>2</sub> laser, then either directly detected or passed through one of the samples and detected. Once ratioed this gave absolute transmission results for each sample. A Molelectron pyroelectric detector type P4-42 was used, coupled directly into a Brookdeal phase sensitive detector. The output from this was plotted on an x-t recorder.

The second batch of wafers was investigated. Typical results and analysis are given in chapter 5 page 50.

Figure 32



## CHAPTER 4

### Millimeter Wave Measurements (Figure 33)

A similar experiment to the far-infrared laser experiment was conducted using a 95 GHz ( $3160 \mu\text{m}$ ,  $3.17 \text{ cm}^{-1}$ ) impatt source, chopped electrically at 100 Hz then transmitted directly through the sample to the Molelectron pyro-electric detector. Removing the sample allowed the impatt output power to be measured directly. Ratioing the two results gives absolute transmission measurements.

The signal was processed through a Brookdeal 9412A phase sensitive detector and its output plotted as a function of time. These results are presented in chapter 5 page 52.

### Centimeter Wave Measurements (Figure 34)

A klystron microwave source was coupled through a ferrite isolator and a slide screw impedance phase matcher to a crystal detector. The crystal was used to measure the silicon wafer's transmission at three frequencies, 8.4 GHz, 8.68 GHz and 9.98 GHz ( $3.57 \text{ cm}$ ,  $3.45 \text{ cm}$  and  $3 \text{ cm}$ ).

The experimental method involved first tuning the source then using the phase matcher to match impedances between the source and detector, so maximising the crystals output. After noting the detector output, the sample was placed between the detector and the tuner and the reduced output noted. Ratioing these two values gives an absolute measure of the transmission which can be compared with the predicted value. These results are presented in chapter 5 page 53.

Figure 33 Millimeter Wavelength  
Experimental Arrangement

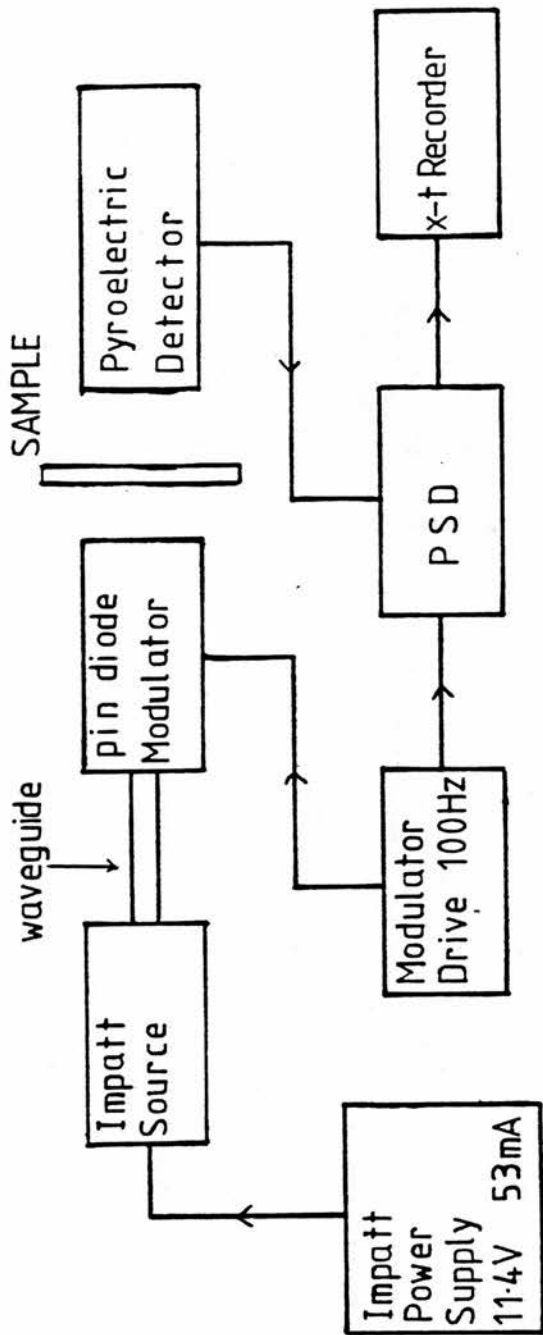
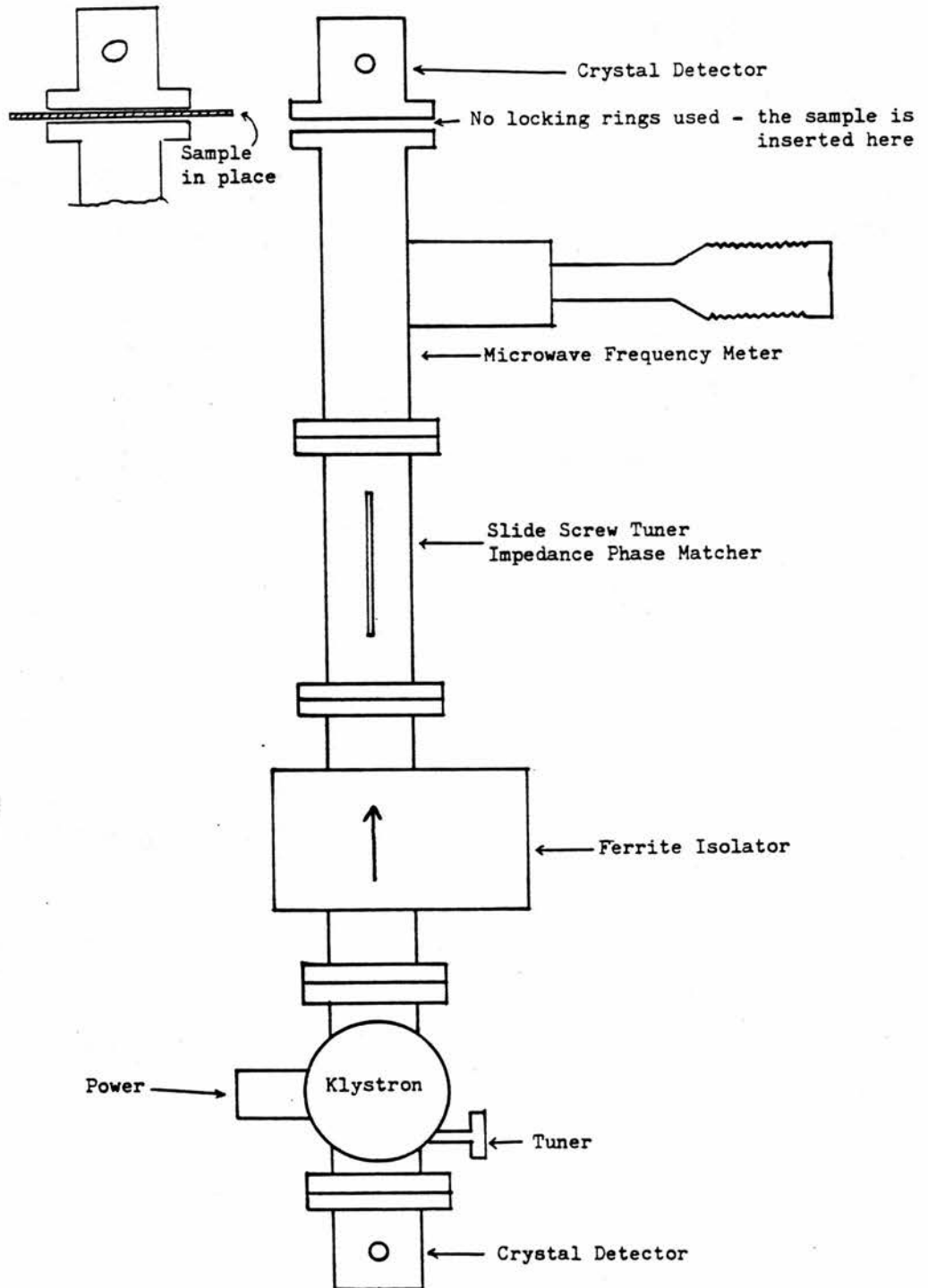


Figure 34 Centimeter wavelength  
Experimental Arrangement



## CHAPTER 4

### Sheet Resistivity

The predicted distribution of electron concentration with depth (figures 36 and 48) and the formula used to relate mobility with electron concentration (Chapter 2 equations 45 & 46) can be used to calculate the conductivity of the implanted layer:  $\sigma = N.e.\mu$  the sheet resistivity of the layer is:  $R_s = 1 / (\sigma.d)$  where d is the implanted layer thickness. The sheet resistivity of the six samples ion-implanted at Hughes Microelectronics Limited along with the two Plessey samples was measured at Hughes Microelectronics Ltd. and the measured vs. the calculated results are given in chapter 5 page 55.

## CHAPTER 5

### EXPERIMENTAL RESULTS

#### 2 $\mu\text{m}$ to 8 $\mu\text{m}$ Results

The reflectivity vs. wavelength plots for each of the first six wafers implanted (details in table 1 chapter 4 page 35) are shown in figure 35 a), b) & c) for boron and figure 36 a), b) & c) for the phosphorous implants. The greatest change was noted in the reflectance curves for phosphorous, (because of the higher mobility of the electrons compared to the holes), and it was decided to concentrate on this implant type. The transmission results are not presented because the wafer's rear surfaces were unpolished and this resulted in the transmitted light being scattered diffusely giving unreliable results in the near infrared.

Figures 35 and 36 are plots of examples of the raw data collected directly into the St. Andrews University computer. By dividing point for point the reflectivity or transmission data by the appropriate background spectra, e.g. figure 30 with no filters being used, the characteristic features of the spectrometer and air absorptions can be removed. A simple programme was written to perform this, and the ratioed reflectance results of wafers 8 to 12 (implant details given in table 2 chapter 4 page 36) are shown in figure 37. No signal appears below  $\approx 2 \mu\text{m}$  because the spectrometer signal throughput is too low for ratios to be obtained accurately.

The grating spectrometer working over the 2  $\mu\text{m}$  to 8  $\mu\text{m}$  spectral region, with 2 mm, slits has a resolution of approximately 0.1  $\mu\text{m}$ . Digitised spectra over the 2  $\mu\text{m}$  to 8  $\mu\text{m}$  region contain about 700 points. This corresponds to about 12 times more points than the spectrometers resolution.

The fine structure seen in the experimental results is therefore noise. This can be averaged out and a computer

Figure 35 Reflectivity vs. Wavelength  
Silicon Implanted with Boron

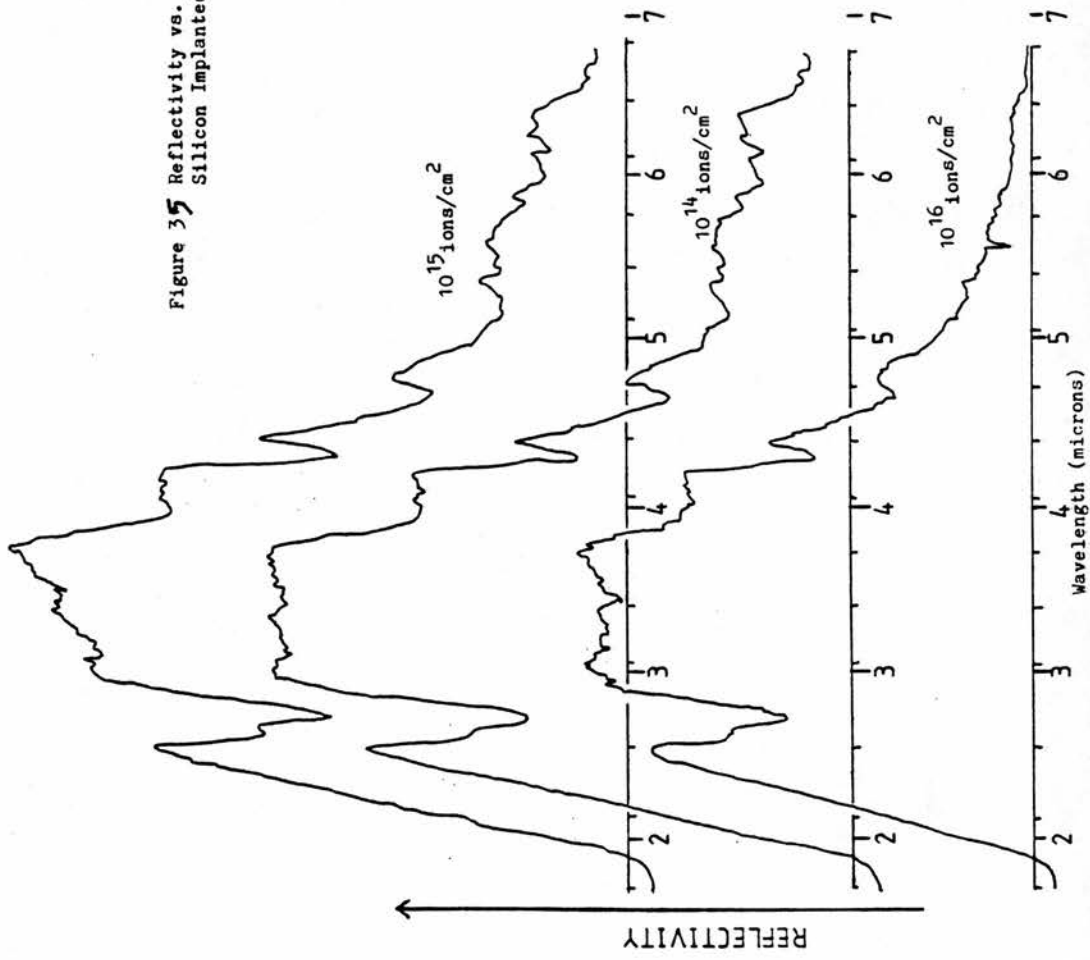


Figure 36 Reflectivity vs. Wavelength  
Silicon implanted with Phosphorous

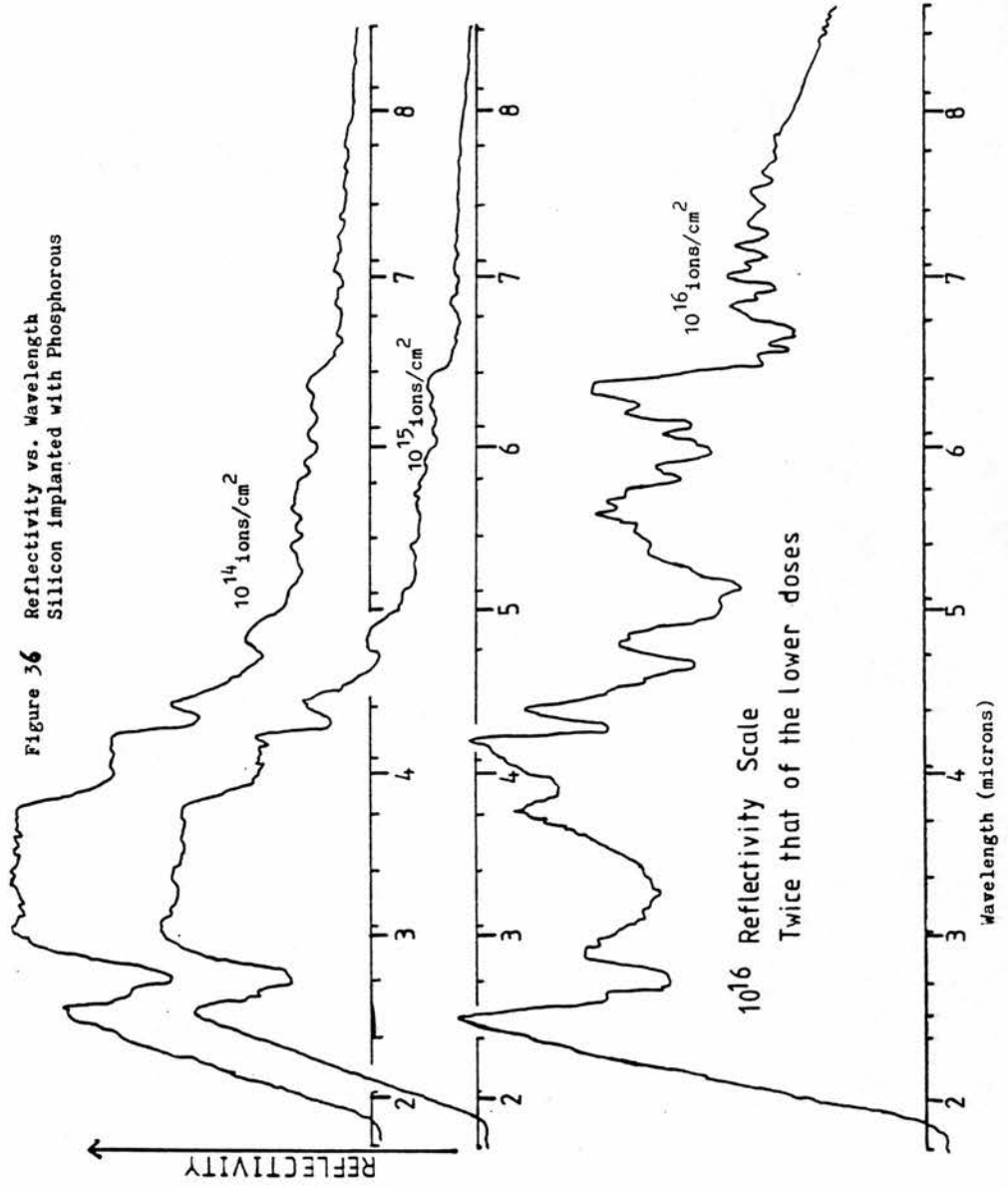
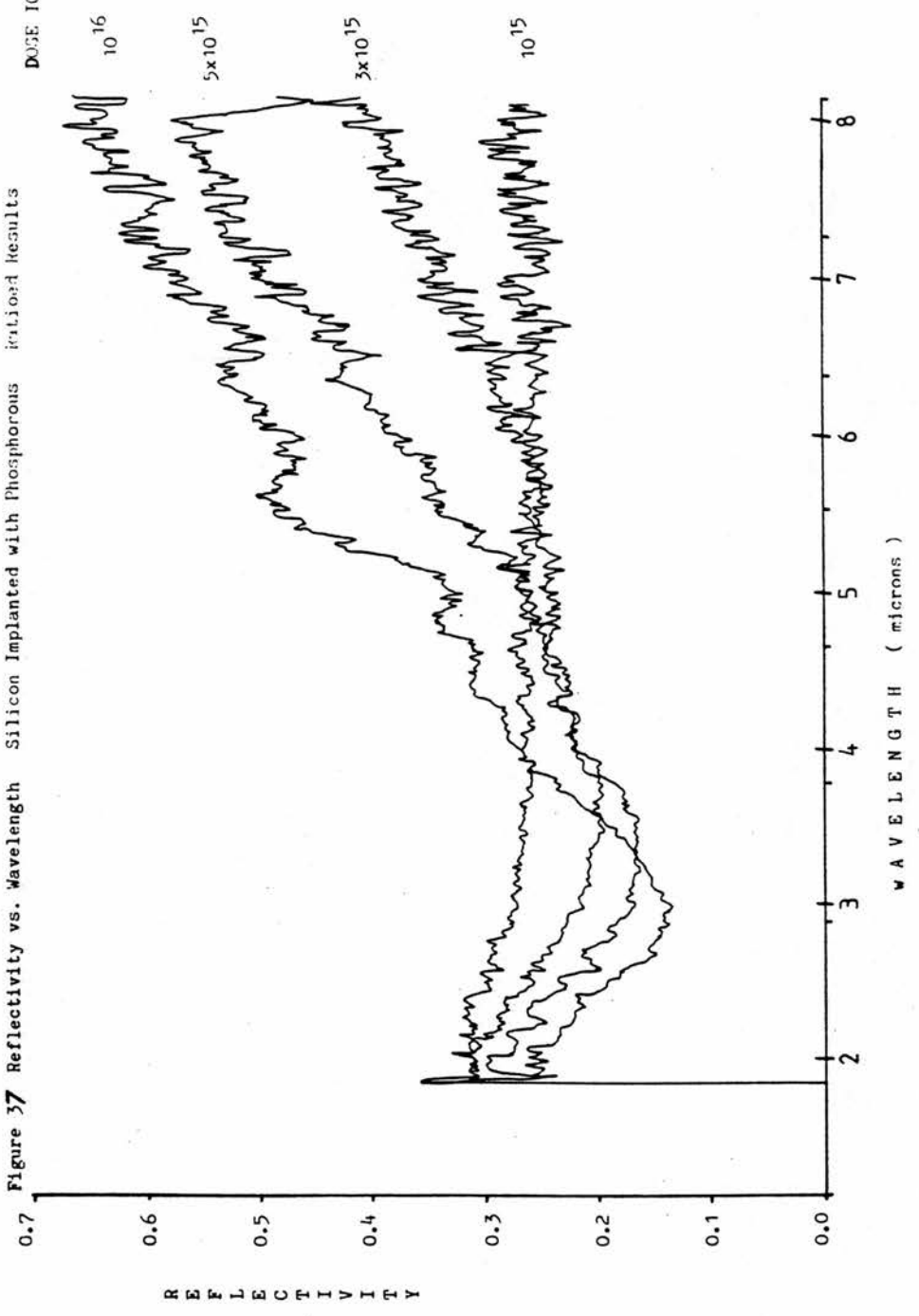


Figure 37 Reflectivity vs. Wavelength Silicon Implanted with Phosphorous Irradiated Results



## CHAPTER 5

programme was written to do this. The method took a moving average of eleven data points i.e. for any spectrum with 700 points  $x_1$  to  $x_{700}$  then the averaged spectrum is  $a_6$  to  $a_{695}$

where 
$$a_r = \left( \sum_{i=-5}^{i=+5} x_{r+i} \right) / 11$$

The theoretical curves were then calculated using the programme described in Chapter 3 and Appendix A, and the assumed implanted ion distribution adjusted until the best fit was achieved for all the experimental reflectance data.

The starting point for the calculated distribution came from Runge [27] page 159. Runge defines range as the mean depth of the implant distribution and  $\Delta R$  as the standard deviation. At 180 KeV the calculated range of phosphorous in silicon is given as  $\approx 2800 \text{ \AA}$  with a  $\Delta R$  of  $\approx 800 \text{ \AA}$ . From this, the theoretical reflectance curve was calculated and plotted over the experimental reflectance curve for one implant dose. This process was repeated adjusting the mean (range) and standard deviation ( $\Delta R$ ) of the ion distribution to optimise the fit, using figures 11, 12 and 13 of chapter 3 as guides to the effect of the changes.

Because the identical conditions i.e. implant energies, orientations, oxide thicknesses etc. were used for each wafer, each wafer should have the same ion distribution (same depth of peak concentration and standard deviation). The only difference should be in total number of ions implanted and therefore the total number of free electrons. Thus, once the best fit for one dose is found, by changing only the dose parameter in the programme the theoretical output curve should match the experimental curve for the new dose.

Using a ten layer model with the last layer at 3000  $\text{\AA}$ , the ion distribution peak at 1000  $\text{\AA}$  and a standard deviation of 1500  $\text{\AA}$  gives the computer generated curves shown in figure

38 a), b) and c) vs. the averaged experimental data for the  $10^{15}$ ,  $3 \times 10^{15}$ , and  $5 \times 10^{15}$  ions/cm<sup>2</sup> implants.

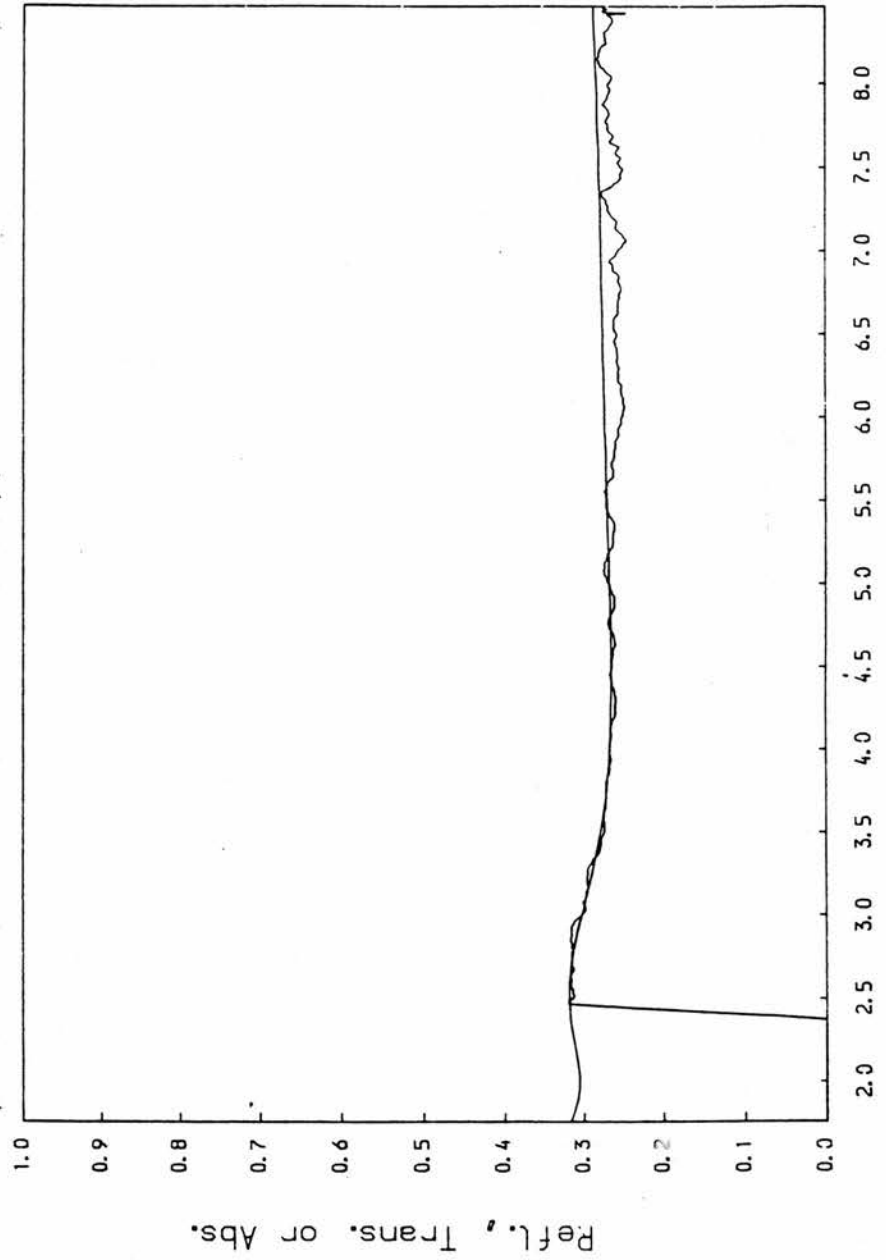
Two plots, using the same distribution data (figure 39 a & b), are shown for the  $10^{15}$  ions/cm<sup>2</sup> implant. Plot a) assumes  $10^{15}$  ions/cm<sup>2</sup> but because this is not such a good fit plot b) assumes  $0.75 \times 10^{15}$  ions/cm<sup>2</sup> which gives a better fit. This is still not as good as the lower implant fits. Figure 40 shows the calculated electron concentration vs. depth into the wafer for the figure 38 and figure 39 results.

The b) plot (figure 39), was based on an assumption that only 75% of the implanted ions provided free electrons i.e. 75% activation. Silicon has  $5 \times 10^{22}$  atoms per cm<sup>3</sup>; the peak concentration used in the model occurs at a depth of 1000 Å and is  $2.7 \times 10^{20}$  atoms of phosphorous per cm<sup>3</sup> or 0.5% phosphorous. This is above the solubility limit of phosphorous in silicon (chapter 1 page 14) and at these concentrations the assumption that phosphorous in the silicon lattice does not disturb the band structure and that each phosphorous atom can be treated independently may not be valid. After annealing, various complexes between the phosphorous atoms and the phosphorous and silicon atoms can form, as well as with the residual carbon and oxygen impurities. This reduces the number of electrons available for conduction below the 100% activation value.

Thus rather than using 75% activation over the whole depth of the implant, another approach is to postulate a cut-off implant concentration above which any additional donor atoms provide no free electrons.

Placing such a cut-off value into the theoretical calculation, and maintaining the distribution which gives accurate fits at lower implant doses whilst using an implant dose of  $10^{15}$  ions/cm<sup>2</sup>, dramatically alters the calculated reflectance curve. Figure 41 shows the best fit obtained using a cut-off concentration of  $1.4 \times 10^{20}$  ions/cm<sup>3</sup> and

Figure 3(a) Si → P  $10 \times 10^{15}$  ions/cm<sup>2</sup>  
Optical characteristics of ion implanted Silicon



Linear wavelength scale, microns

Figure 3(b) Si → P  $3.0 \times 10^{15}$  ions/cm<sup>2</sup>  
Optical characteristics of ion implanted Silicon

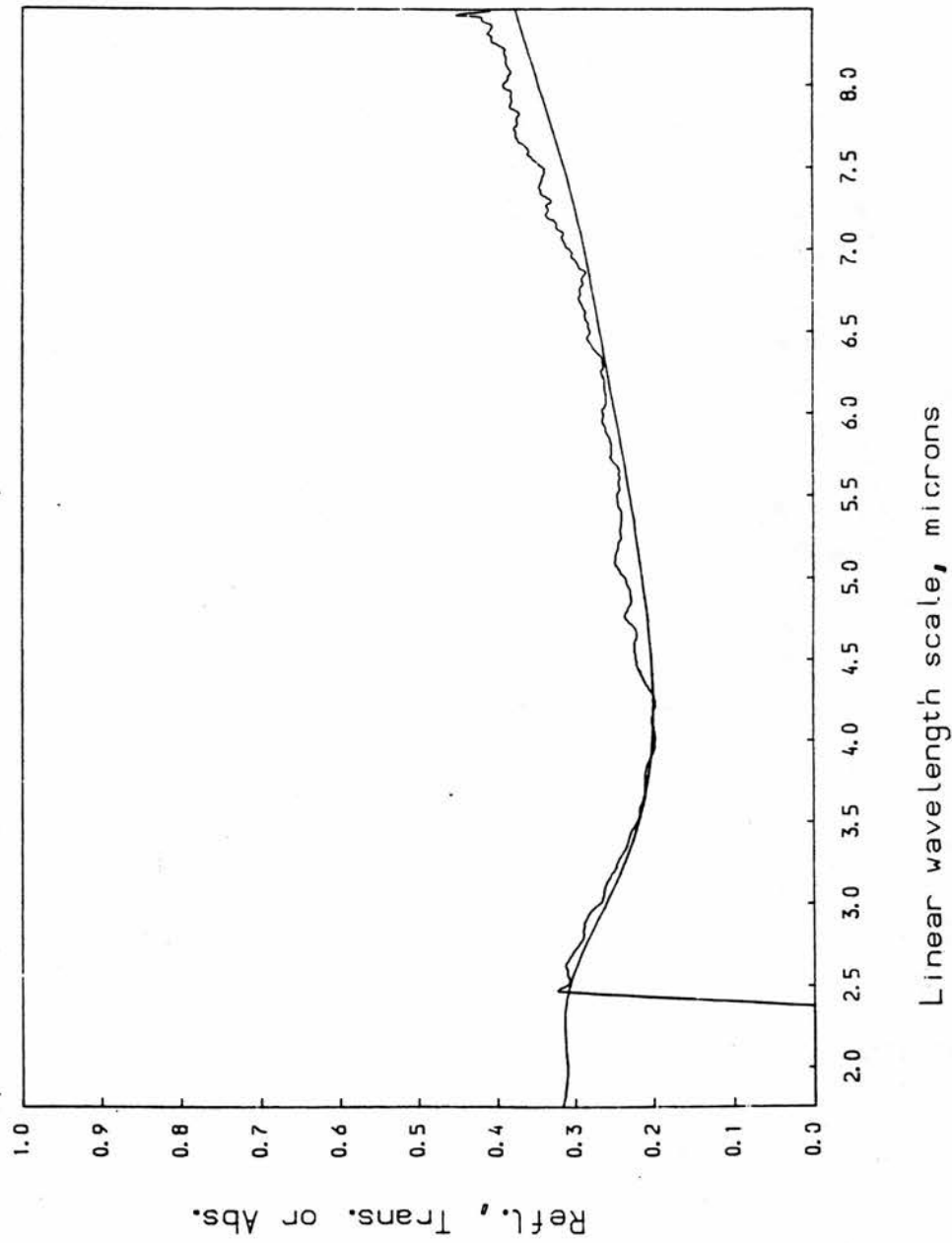


Figure 30 c) Si → P  $5.0 \times 10^{15}$  ions/cm<sup>2</sup>  
Optical characteristics of ion implanted Silicon

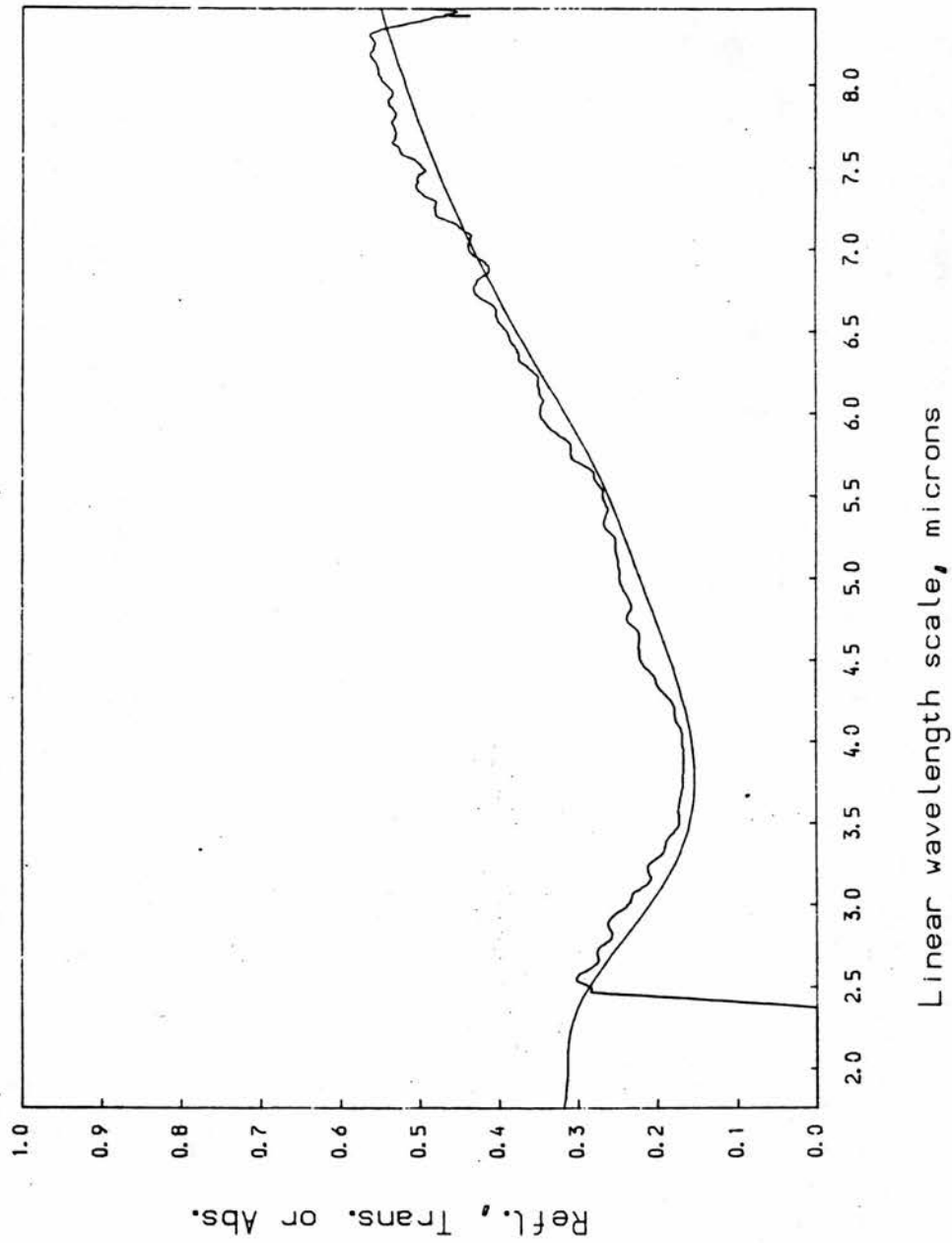


Figure 39 Si → P a:  $10 \times 10^{16}$  ions/cm<sup>2</sup>; b:  $7.5 \times 10^{15}$  ions/cm<sup>2</sup>  
Optical characteristics of ion implanted Silicon

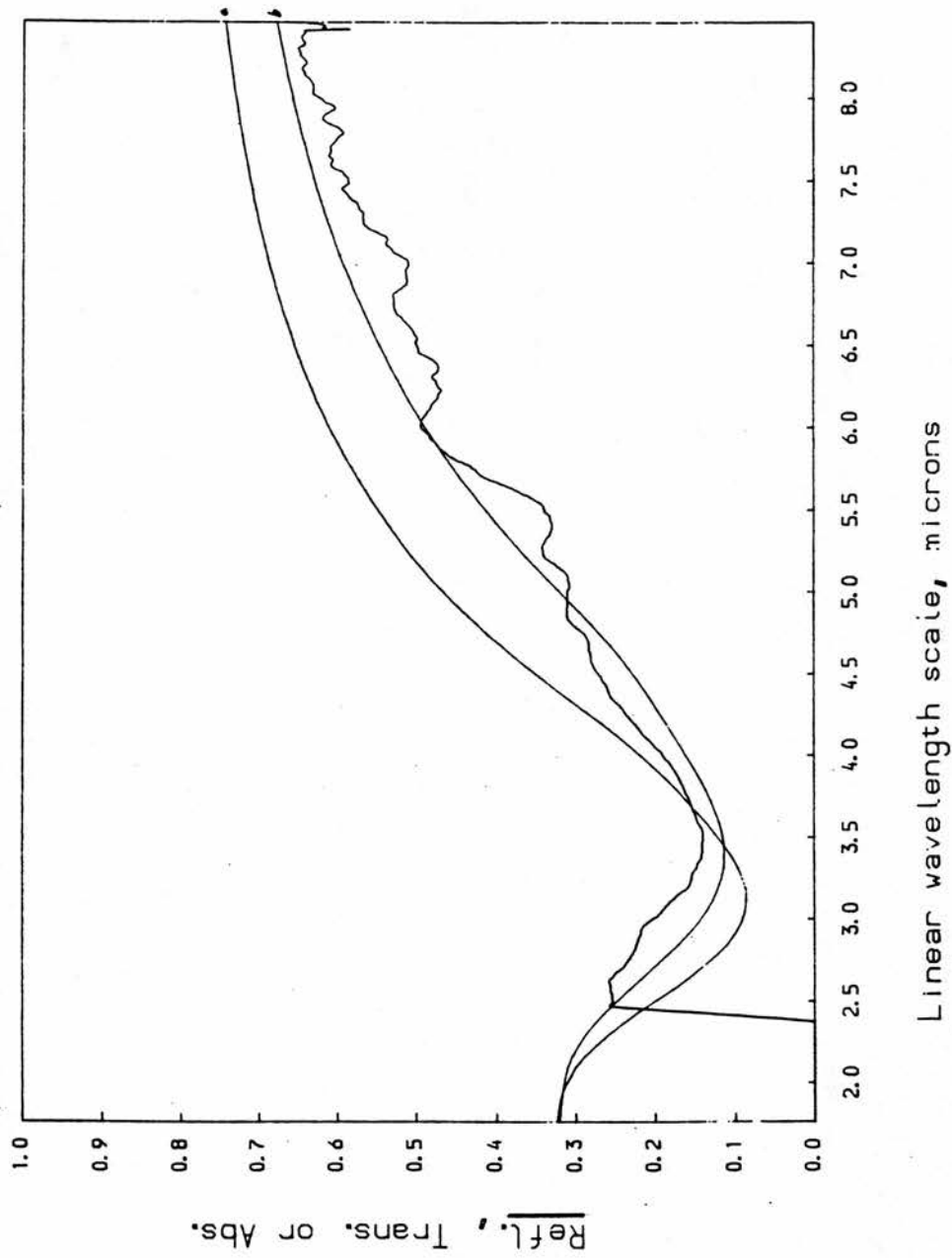


Figure 40

Predicted Implanted Phosphorous Concentration vs. Depth

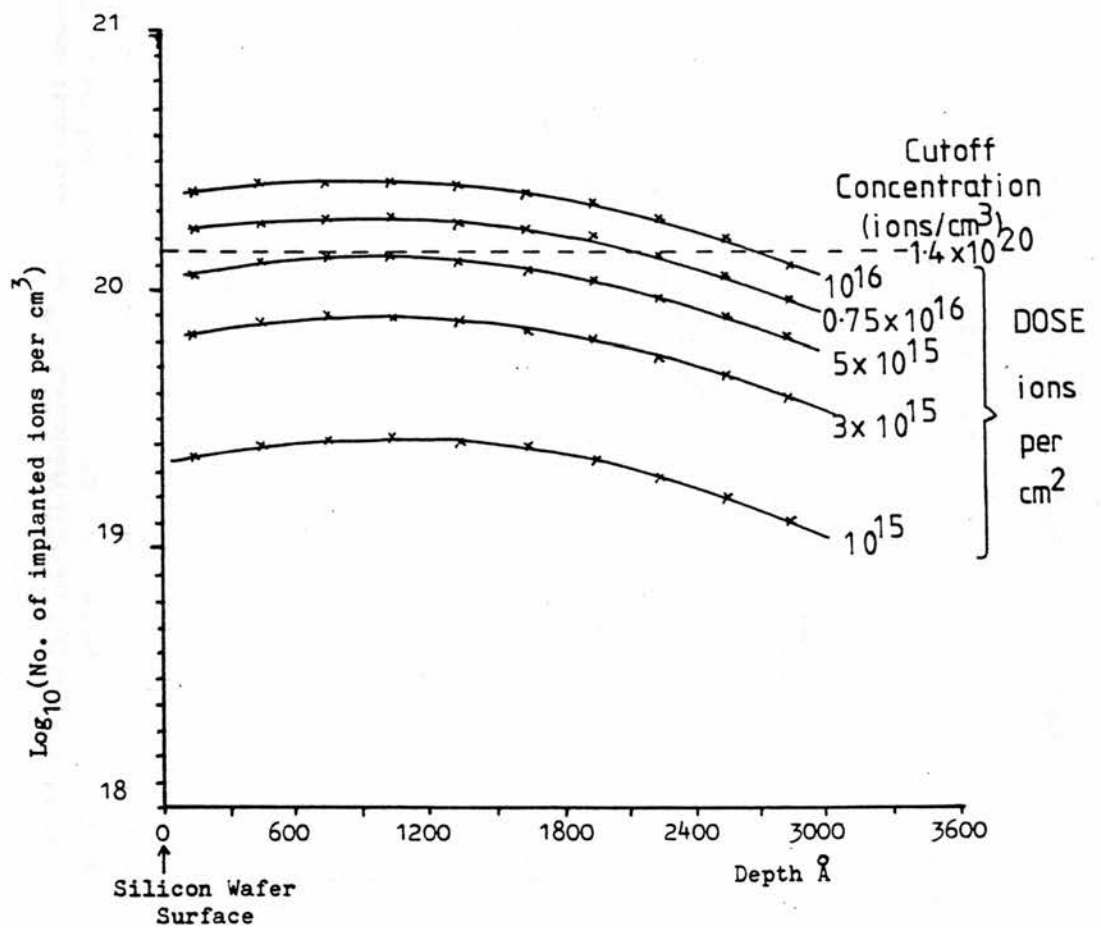
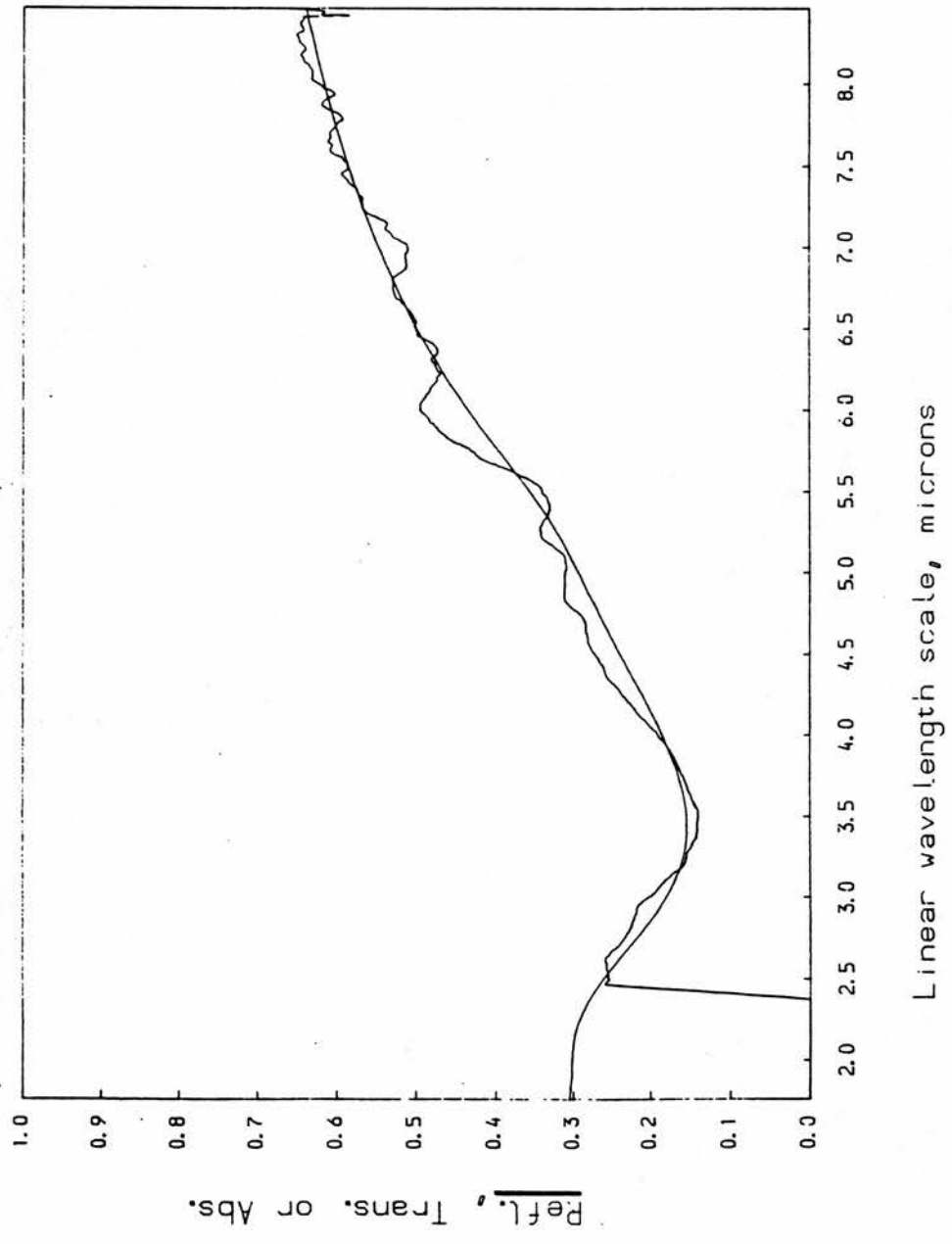


Figure 41 Silicon implanted with Phosphorous  $10^{16}$  ions/cm<sup>2</sup> with cutoff concentration at  $1.4 \times 10^{20}$  electrons/cm<sup>3</sup>  
Optical characteristics of ion implanted Silicon



## CHAPTER 5

compares it to the experimental reflectance curve. The cut-off concentration is drawn on figure 40.

### Results for Arsenic Implanted Silicon from Plessey

Figure 42 shows the experimental reflectance curve and the best predicted curve for sample MSO61/TP4; figure 43 gives the same information for sample MSO38/1.

For MSO61/TP4 figure 44 a) shows the distribution of activated implant ions vs. depth. The values used are:-

implant concentration =  $3.9 \times 10^{15}$  ions per  $\text{cm}^2$   
cutoff concentration =  $1.4 \times 10^{20}$  electrons per  $\text{cm}^3$

Mean depth = 18 Å  
Standard deviation = 900 Å  
Maximum depth = 1800 Å

For MSO38/1 figure 44 b) shows the distribution of activated implant ions vs. depth. The values used are:-

implant concentration =  $10^{15}$  ions per  $\text{cm}^2$   
cutoff concentration =  $1.4 \times 10^{20}$  electrons per  $\text{cm}^3$

Mean depth = 450 Å  
Standard deviation = 300 Å  
Maximum depth = 1800 Å

Figure 45 shows the arsenic and carrier concentration vs. depth data supplied by Plessey, with the reflectivity data points, independently derived, superimposed upon it.

Sample MSO61/TP4 has the implanted ion and the carrier concentration plotted separately. The carrier concentration follows the implanted ion concentration until the  $1.4 \times 10^{20}$  per  $\text{cm}^3$  level where the carrier concentration levels

Figure 42 Experimental and matched Theoretical Reflectivities for Arsenic Implanted Silicon  
Optical characteristics of ion implanted Silicon

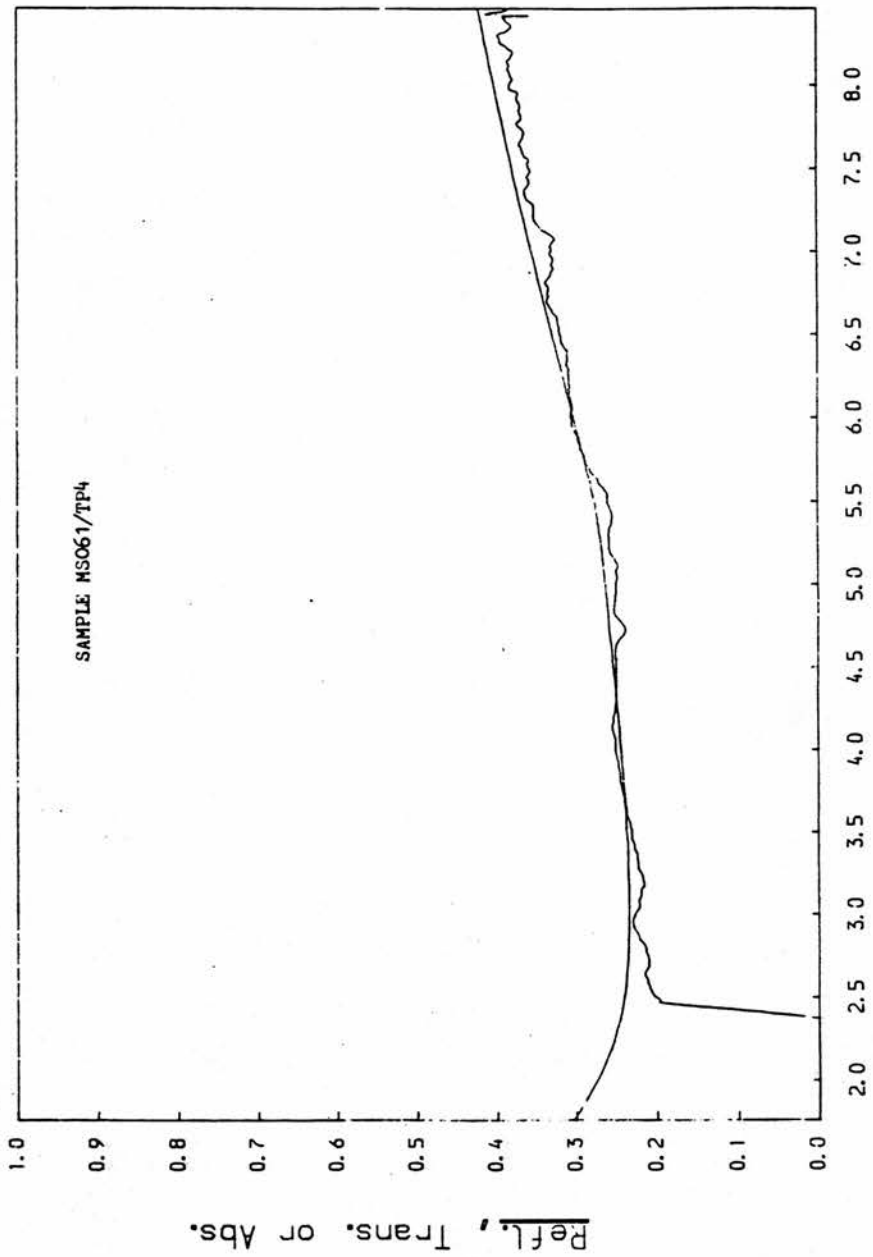
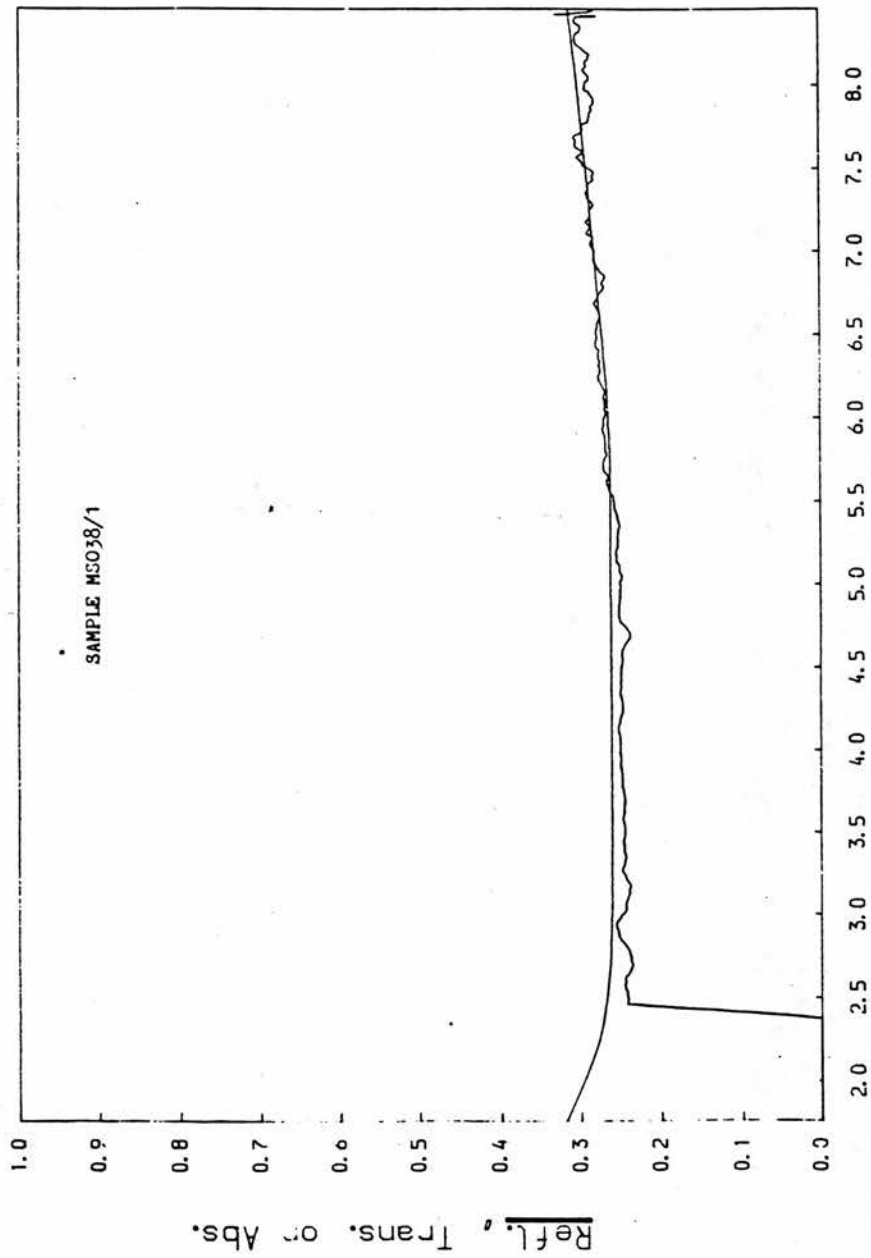


Figure 4.3 Experimental and Matched Theoretical Reflectivities for Arsenic Implanted Silicon  
Optical characteristics of ion implanted Silicon



Linear wavelength scale, microns

Figure 44 Predicted Electron Concentrations vs. Depth for Implanted Arsenic

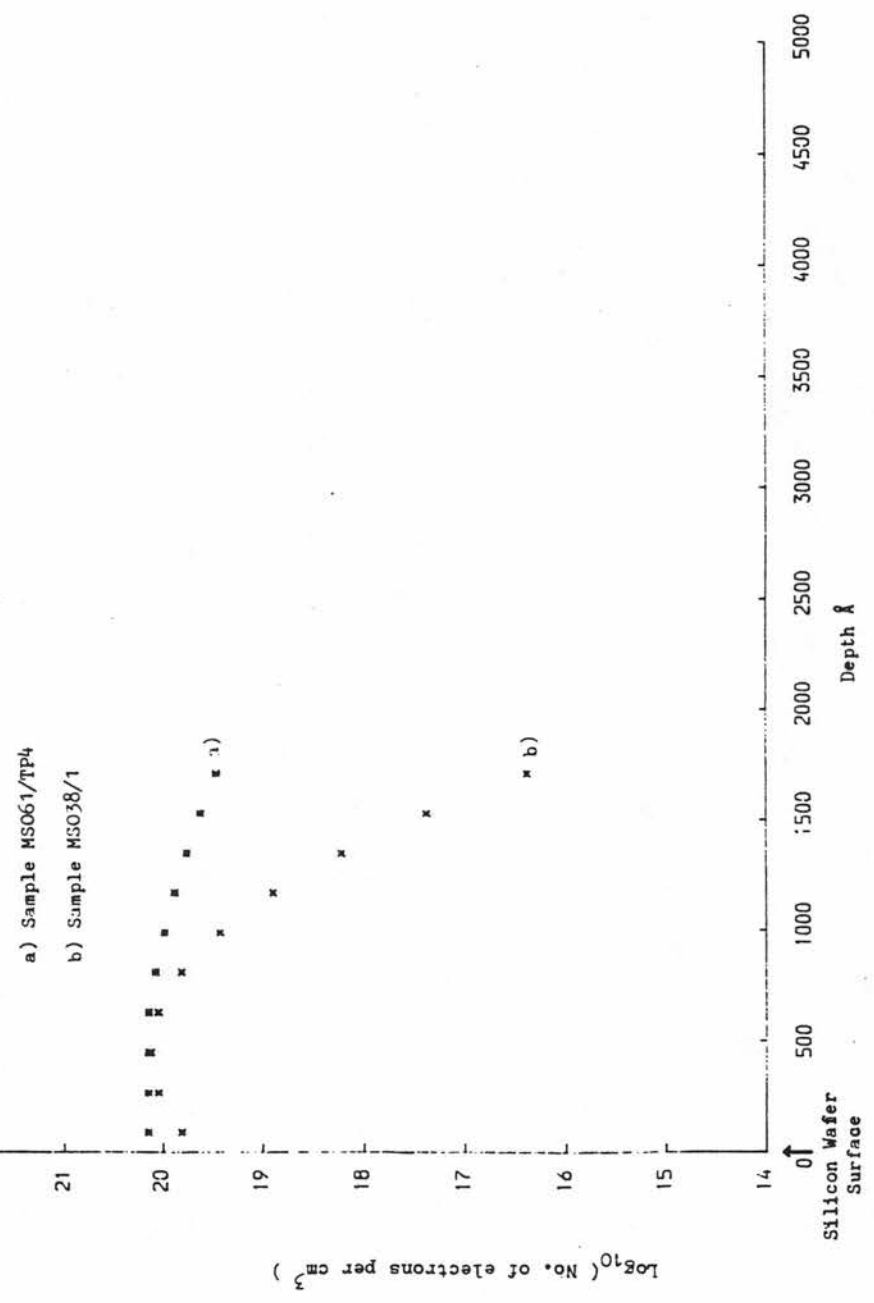
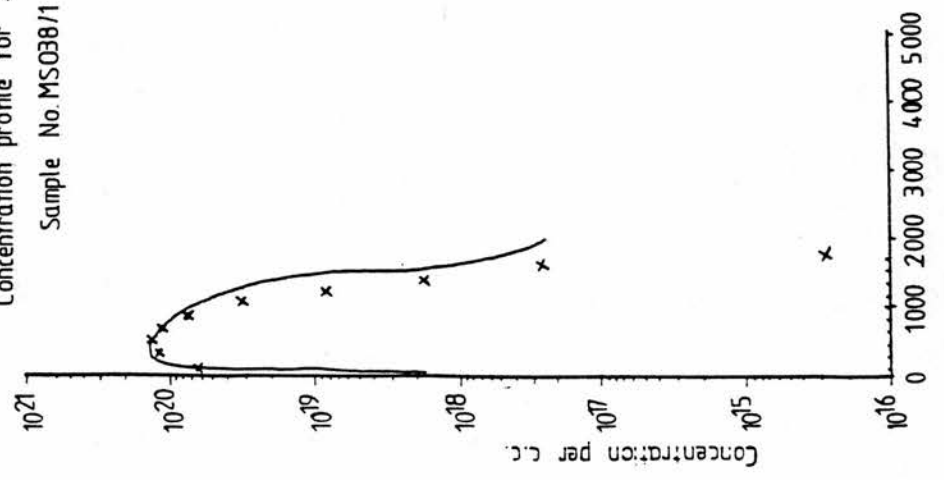


Figure 45

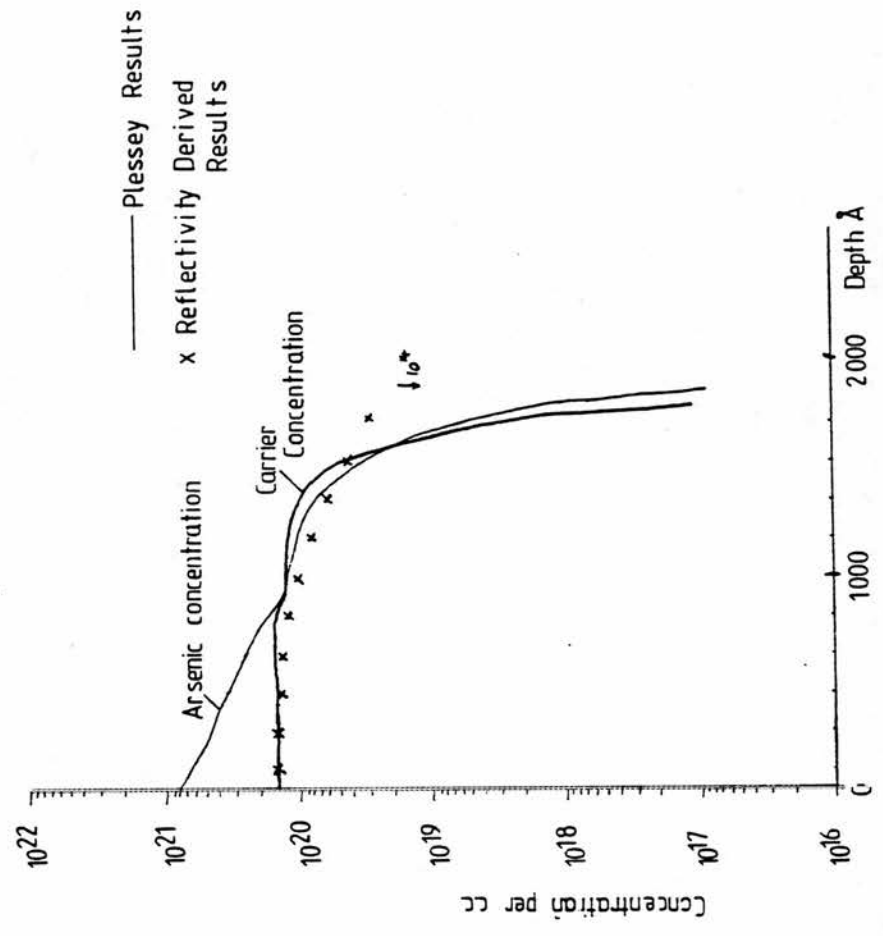
Concentration profile for Si  $\rightarrow$  As

Sample No. MS038/1



Concentration profile for Si  $\rightarrow$  As

Sample No. MS061/TP4



off. This occurs at exactly the same concentration as was required to obtain the optimum fit to model the Hughes ion-implanted samples (figure 40).

Figure 44 also demonstrates how close the predicted ion concentrations are to the measured values, particularly for MSO38/1.

These results demonstrate that the theoretical calculations are not specific to phosphorous, but that they apply to donor species in general and that profiling can indeed be performed non-destructively by near infrared techniques.

#### 12.5 $\mu\text{m}$ to 1 mm Results

The second batch of wafers (7 to 12) were analysed. The samples showed very strong interference fringe effects in transmission, and the transmission dropped (reflectance rose) as the implant dose was increased. The predicted interference fringe spacing corresponds well to the experimentally observed spacing ( $3.99 \text{ cm}^{-1}$ ) for a wafer thickness of  $364.8 \mu\text{m}$ . Figure 46 a) shows a typical background spectra without a sample; the broad structure is caused by the 100 gauge beamsplitter used (Appendix B). Figure 46 b) shows a transmission spectrum for an un-implanted silicon wafer but otherwise the conditions are the same as for figure 46 a). The fine structure is the product of the wafer acting as a Fabry-Pérot interferometer in a similar way to the 100 gauge beamsplitter.

Finally figure 46 c) shows the transmission given in figure 46 b) divided point for point by values from figure 46 a) to remove spectrometer features which leaves only the silicon wafer effects. Gaps are left where the spectrometer throughput has dropped too low to provide an accurate ratio. Comparing figure 46 c) with the predicted characteristic figure 18 in chapter 3 shows that up to  $100 \text{ cm}^{-1}$  the modulation in transmission varies from 100% down to 30% and

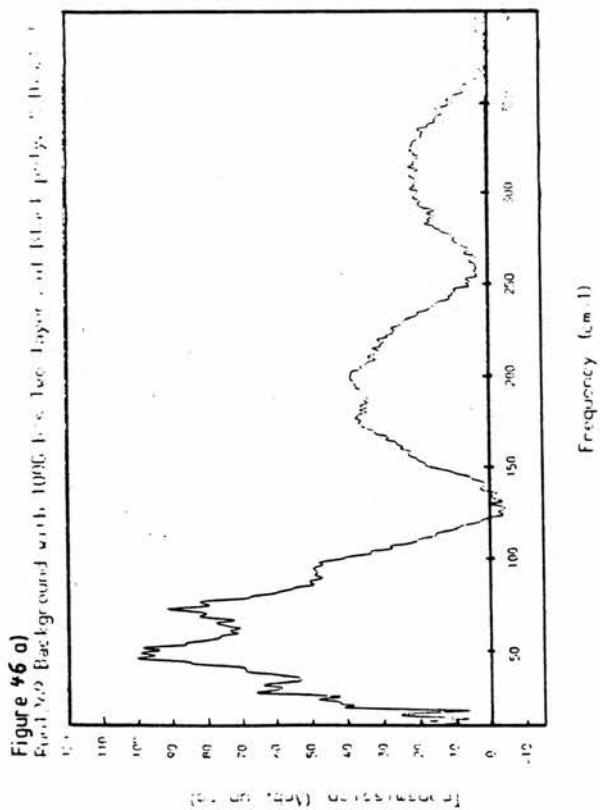
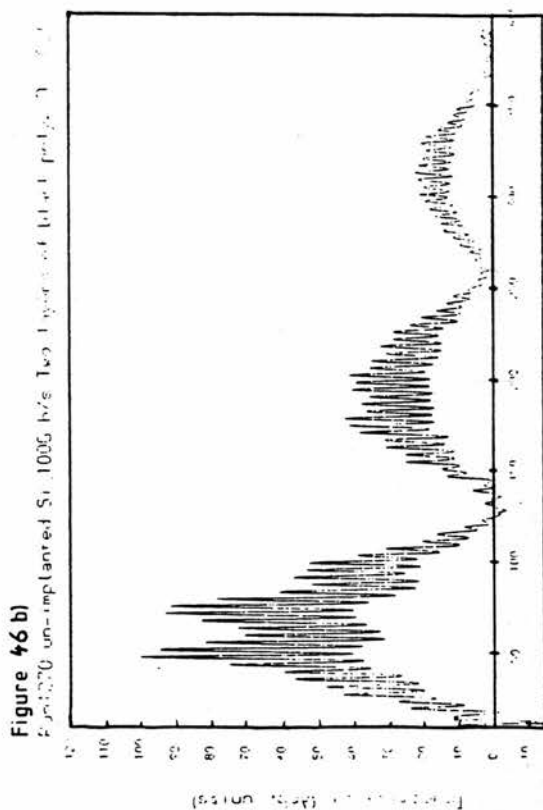
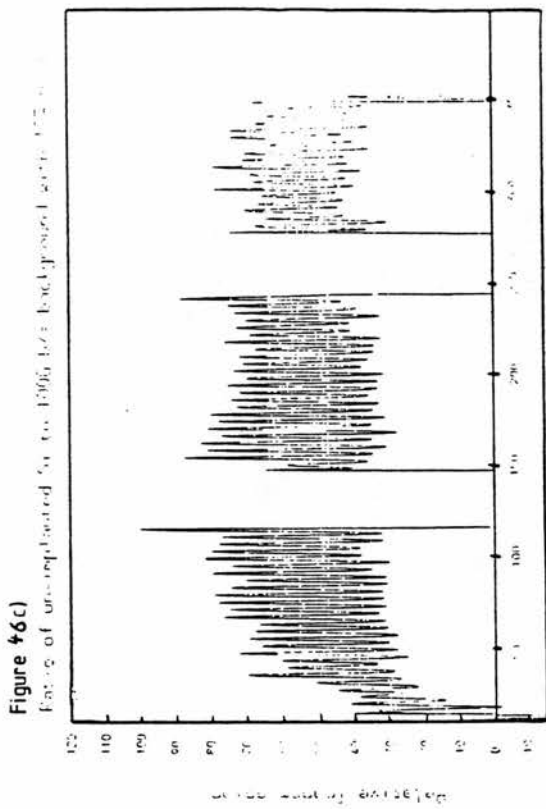


**Figure 46** Far infrared Fourier Transform Spectrometer  
 Experimental Results for an un-implanted  
 Silicon Wafer



## CHAPTER 5

that the experimental results are in agreement with this. At higher wavenumbers the modulation in transmission falls off. This could be due to the coherent reflection power from the rear of the wafer dropping as the radiation wavelength becomes small compared to the wafer thickness and the un-polished wafer rear surface starting to act as a diffuse rather than specular reflector (see Chapter 3 page 27 for a more detailed explanation). For the implanted wafers the theoretical transmission modulation falls with increased dose, for  $10^{16}$  ions/cm<sup>2</sup> the modulation is from 18% to 12% (figure 18 in chapter 3), and the experimental results agree. The higher implants transmit little light and table 3 compares these results with theory.

The practical low frequency (long wavelength) limit to the interferometer is  $\approx 10$  cm<sup>-1</sup>. This is unfortunate because, as can be seen by comparison with theoretical results (chapter 3 figures 26, 27 and 28), the longer wavelength region of the spectrum offers insensitivity to the precise thickness of the wafer, combined with a strong dependence on value of dose.

Table 3 gives the reflection and transmission values obtained experimentally. These were derived from the measure of absolute intensity (as described in Chapter 4, page 38) and represent the total reflected and transmitted power over the full pass band of the interferometer ( $\approx 10$  cm<sup>-1</sup> to 400 cm<sup>-1</sup>). Table 3 also shows the transmission and reflection ratios for implanted to un-implanted wafers and the corresponding theoretical values.

## CHAPTER 5

TABLE 3

Total Transmission				Total Reflection			
Experimental		Theory		Experimental		Theory	
Implant ions/cm <sup>2</sup>	Absolute value PSD level	Ratio	Ratio	Absolute value PSD level	Ratio	Ratio	Ratio
10 <sup>15</sup>	0.08	0.02	0.05	9.98	2.42	1.87	
5x10 <sup>15</sup>	0.22	0.05	0.06	9.40	2.28	1.82	
3x10 <sup>15</sup>	0.41	0.09	0.10	8.61	2.09	1.69	
10 <sup>15</sup>	1.29	0.30	0.27	5.65	1.37	1.34	
none	4.37	1.00	1.00	4.12	1.00	1.00	
control	4.37	1.00	1.00	4.12	1.00	1.00	

The ratioed experimental values allow direct comparison between theory and experiment. They are calculated by dividing each experimental result by the control result. The theoretical ratio is obtained by dividing the theoretical transmittance, or reflectance, for each implant dose by that obtained for an un-implanted wafer.

The experimental error for the transmission ratio is  $\pm 0.01$ . However the specimen area sampled in the reflectivity experiments is less well defined and any uncertainty in this has a squared effect on the power measured increasing the error to possibly as high as 20%.

The effect of a thick, 700 Å, oxide layer on reflection and transmission was not noticeable in any of the experiments in the near- or far-infrared. At 1  $\mu\text{m}$   $\lambda/4$  is 2500 Å, so the effects of a 700 Å layer were expected to be negligible over the range of wavelengths investigated.

## CHAPTER 5

The predictions of chapter 3 page 31 and 32 about the change in phase of the transmission fringes are difficult to observe. The individual wafers vary a significant amount in thickness (from 365  $\mu\text{m}$  to 385  $\mu\text{m}$ ) and this translates into a variation in fringe spacing which makes the reliable observation of a phase shift over a large frequency interval difficult. By looking at the first clearly observable fringe at lowest wavenumber the phase inversion is seen. All the wafers have identical phase except the unimplanted one which is 180° out of phase as predicted.

## CHAPTER 5

### Discrete Far-Infrared Measurement Results

The second batch of wafers was investigated and typical results shown in Figure 47.

To predict the transmission properties at a discrete wavelength requires the wafer thickness to be accurately known, e.g. for an unimplanted silicon wafer, the theoretical optical transmission at 118  $\mu\text{m}$  varies with wafer thickness as shown in table 4. The transmission values are calculated using the programme in appendix A.

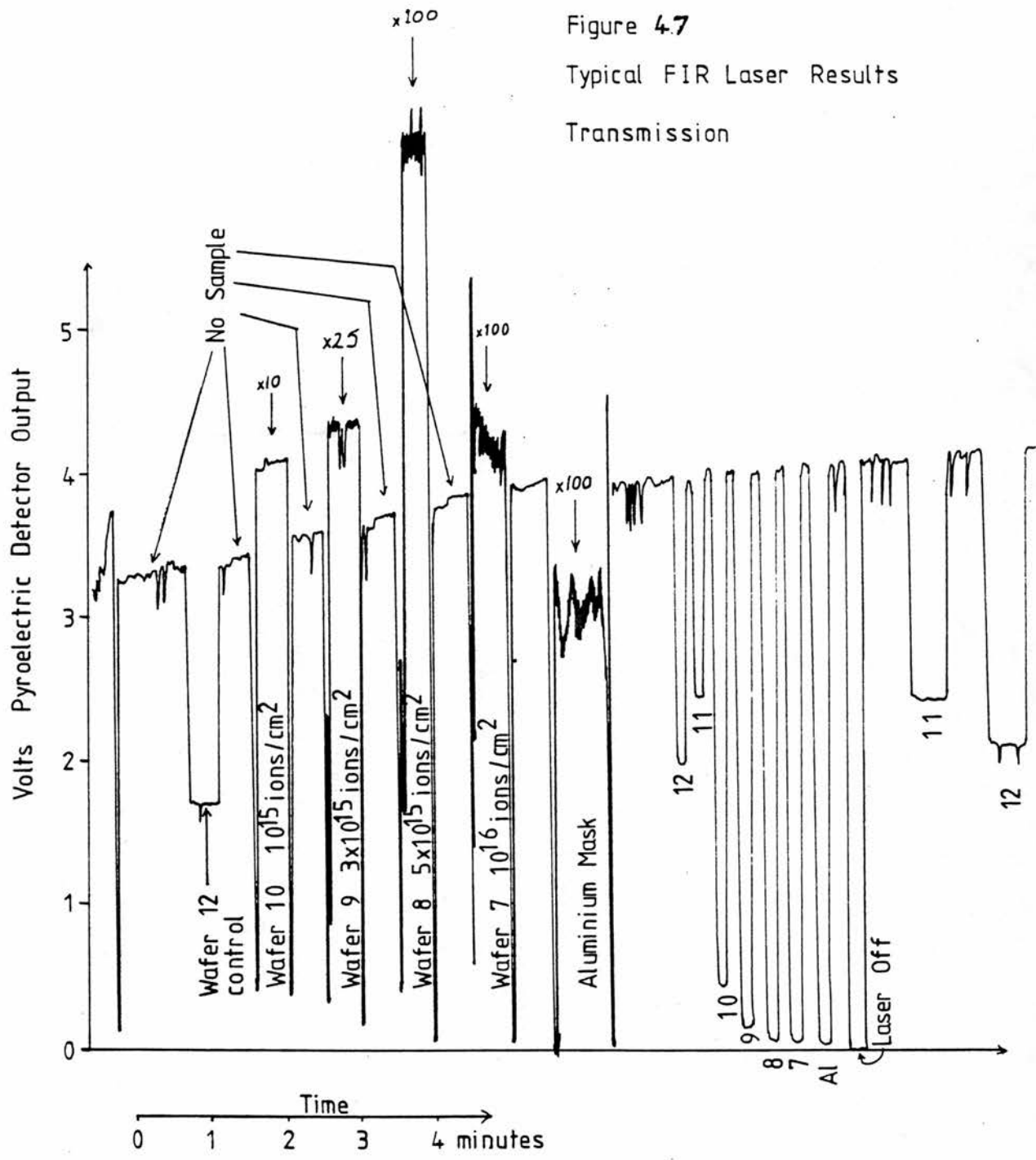
TABLE 4

Transmission vs. Thickness  
For an Undoped Silicon Wafer

Wafer thickness ( $\mu\text{m}$ )	Transmission (%)		
	118 $\mu\text{m}$	163 $\mu\text{m}$	571 $\mu\text{m}$
360	0.96	0.61	0.35
361	0.99	0.51	0.34
362	0.89	0.44	0.33
363	0.72	0.38	0.33
364	0.56	0.35	0.32
365	0.45	0.32	0.31 see fig.18
366	0.38	0.30	0.31
367	0.33	0.29	0.30
368	0.30	0.29	0.30
369	0.29	0.29	0.30
370	0.29	0.31	0.29

At 118  $\mu\text{m}$  a 1% change in wafer thickness (eg 363  $\mu\text{m}$  to 366  $\mu\text{m}$ ) can lead to a change in transmission from 0.72 to 0.38. The extreme sensitivity to thickness is due to the 118  $\mu\text{m}$  wavelength being on the 'side' of an interference

Figure 4.7  
Typical FIR Laser Results  
Transmission



CHAPTER 5

fringe. See, for example, figure 18. If the wavelength was centered at the 'top' or 'bottom' of an interference fringe (such as the 571  $\mu\text{m}$  line) then the effect would be reduced. Bearing this in mind, the predicted figures for transmission at the three laser wavelengths used can be strongly dependent on wafer thickness and orientation.

Table 5 summarises the experimental results.

TABLE 5

Experimental Results vs Theory  
For Silicon Transmission at Three Laser Wavelengths

Wafer No.	12	11	10	9	8	7
implant	control	0	$10^{15}$	$3 \times 10^{15}$	$5 \times 10^{15}$	$10^{16}$
Experiment	TRANSMISSION					
118 $\mu\text{m}$	0.62	0.49	0.11	0.061	0.023	0.003
163 $\mu\text{m}$	0.50	0.61	0.11	0.035	0.008	0.004
571 $\mu\text{m}$	0.57	0.54	0.08	0.053	0.018	0.011
Theory						
Average	0.52	0.52	0.12	0.06	0.04	0.02
Modulation						
Maximum	1.00	1.00	0.18	0.09	0.06	0.055
Minimum	0.29	0.29	0.12	0.03	0.01	0.01

The error amounts to  $\pm 0.05$  which implies poor accuracy for the high implants when the transmission is small.

CHAPTER 5

The nominal thickness of the silicon wafer was 350  $\mu\text{m}$ . The Fourier transform spectrometer results for the unimplanted wafer give a measured interference fringe spacing of  $3.99 \text{ cm}^{-1}$ . This corresponds to a 364.8  $\mu\text{m}$  wafer thickness.

Without knowledge of the absolute wafer thickness to better than 0.5  $\mu\text{m}$  no accurate predictions can be made. The calculated average values of transmission over the 100  $\mu\text{m}$  to 1000  $\mu\text{m}$  region are given at the bottom of table 5, the maximum and minimum refer to figure 18 (the three laser line wavelengths are marked on this figure).

Millimeter Wave Measurement Results

Figure 48 shows typical results for the second batch of implanted wafers (7 to 12). Table 6 gives the experimental transmission results for each wafer as well as the predicted results (see figure 21); fairly close agreement was obtained with theory.

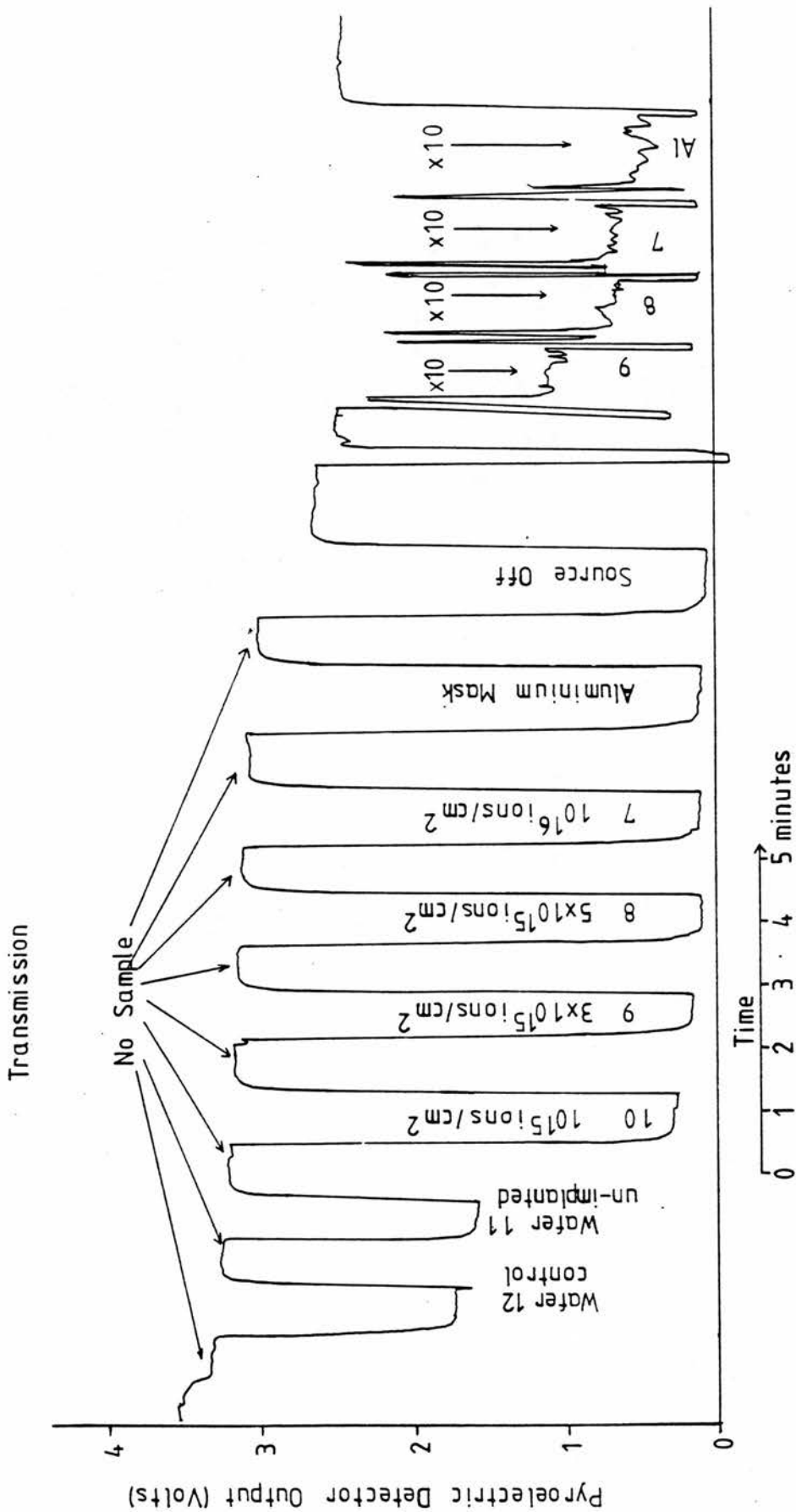
TABLE 6

Experimental Results vs Theory  
For Silicon Transmission at 95 GHz (3.16 mm)

Wafer No.	12	11	10	9	8	7
Implant	control	0	$10^{15}$	$3 \times 10^{15}$	$5 \times 10^{15}$	$10^{16}$
Experiment	0.51	0.48	0.09	0.042	0.026	0.026
Theory	0.49	0.49	0.12	0.039	0.023	0.017

The experimental error amounts to  $\pm 0.006$

Figure 48 Typical Millimeter Wave Results



CHAPTER 5

Centimeter Wave Measurement Results

Tables 7,8 and 9 list the experimental results for each of the three frequencies used as well as the predicted values (figure 24). Only the second batch of wafers was measured (N<sup>o</sup>. 7 to 12).

TABLE 7

Experimental Transmission Compared With Theory  
For Silicon at 9.98 GHz (3 cm)

Wafer N <sup>o</sup> .	12	11	10	9	8	7
Dose cm <sup>-2</sup>	control	0	10 <sup>15</sup>	3x10 <sup>15</sup>	5x10 <sup>15</sup>	10 <sup>16</sup>
Experiment	0.62	0.65	0.19	0.08	0.06	0.04
Theory	0.68	0.68	0.11	0.03	0.02	0.01

TABLE 8

Experimental Transmission Compared With Theory  
For Silicon 8.68 GHz (3.45 cm)

Wafer N <sup>o</sup> .	12	11	10	9	8	7
Dose cm <sup>-2</sup>	control	0	10 <sup>15</sup>	3x10 <sup>15</sup>	5x10 <sup>15</sup>	10 <sup>16</sup>
Experiment	0.62	0.65	0.20	0.11	0.08	0.06
Theory	0.69	0.69	0.11	0.03	0.02	0.01

CHAPTER 5

TABLE 9

Experimental Transmission Compared With Theory  
 For Silicon at 8.4 GHz (3.57 cm)

Wafer N <sup>o</sup> .	12	11	10	9	8	7
Dose cm <sup>-2</sup>	control	0	10 <sup>15</sup>	3x10 <sup>15</sup>	5x10 <sup>15</sup>	10 <sup>16</sup>
Experiment	0.62	0.66	0.20	0.10	0.07	0.05
Theory	0.70	0.70	0.11	0.03	0.02	0.01

The experimental error amounts to ±0.04

CHAPTER 5

Sheet Resistivity Results

TABLE 10

Sheet Resistivity  
Theory vs. Experiment

Sample No.	Implant Dose	Sheet Resistivity ( $\Omega$ )	
		Measured	Predicted
7	$10^{15}$	12.06	23.6
8	$5 \times 10^{15}$	16.0	27.2
9	$3 \times 10^{15}$	24.1	39.0
10	$10^{15}$	61.2	100.1
11	none	639	357
12	control	522	357
MSO61/TP4	$3.9 \times 10^{15}$	52.9	50.9
MSO38/1	$10^{15}$	138.1	89.3

In the case of the Hughes implanted wafers the wafer is p-type and the implant is n-type. This means that the substrate conductance cannot be simply incorporated into the predicted result because of the partial substrate-implant isolation caused by the pn junction. The predicted sheet resistivity is always higher than the measured value for the implanted wafers and the inclusion of some substrate conductance would lower this.

DISCUSSION AND CONCLUSIONSOptimisation Errors

The method used to adjust the predicted curves to fit the experimental data involves using figures 10, 11 and 12 of chapter 3. These show how changes in one of the three parameters - depth, peak position and implant spread adjust the predicted response.

From the results given in chapter 5 pages 43 and 44 the optimum implant distribution required to give theoretical reflectivities which matched the experimental results for the phosphorous implants had the following parameters:

Implant maximum depth	= 3000 Å
Peak concentration depth	= 1000 Å
Standard deviation of implant	= 1500 Å
'Cutoff' concentration	= $1.4 \times 10^{20}$ electrons/cm <sup>3</sup>

By varying the above parameters by 10% and observing the effect on the predicted reflectivities, an idea of the accuracy of the fit can be obtained. If the predicted reflectivity changes significantly for small changes in the assumed implant distribution then the modelling techniques are sensitive to the implanted electron concentrations and profile. If on the other hand changing the assumed implant distribution has little effect on the predicted reflectivities then the modeling techniques are not suitable for mapping the electron concentration with depth.

Figure 49 shows the predicted reflectivities for samples 7, 8, 9 and 10 (implants of  $10^{16}$  to  $10^{15}$  ions/cm<sup>2</sup>, see table 2 chapter 4) where the maximum depth, peak concentration depth and distribution standard deviation have assumed the values listed below and illustrated in figure 50.

FIGURE 49a

Ion-implanted Silicon  
 $10^{16}$  ions/cm<sup>2</sup>

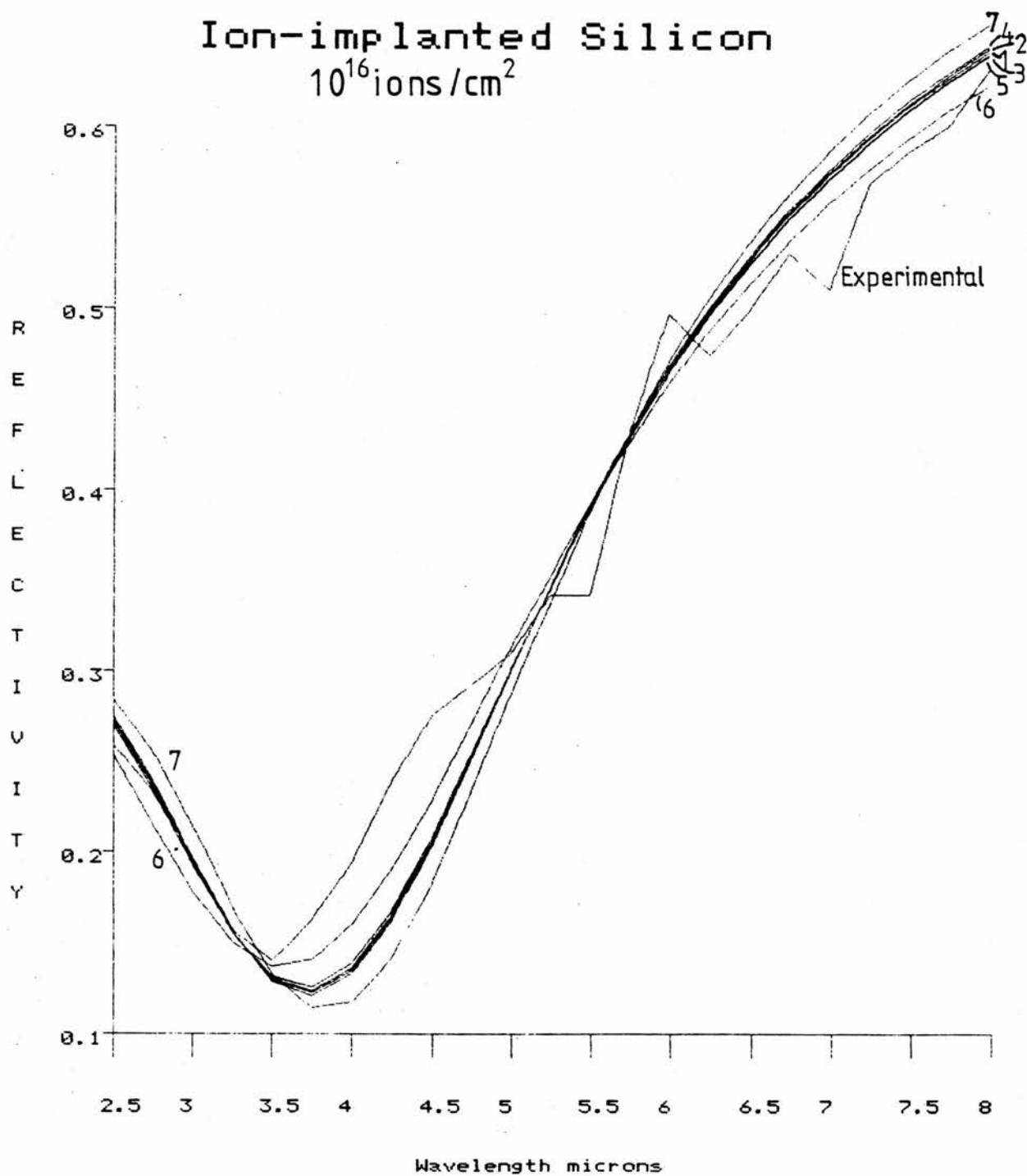


FIGURE 49b

Ion-implanted Silicon  
 $5 \times 10^{15}$  ions/cm<sup>2</sup>

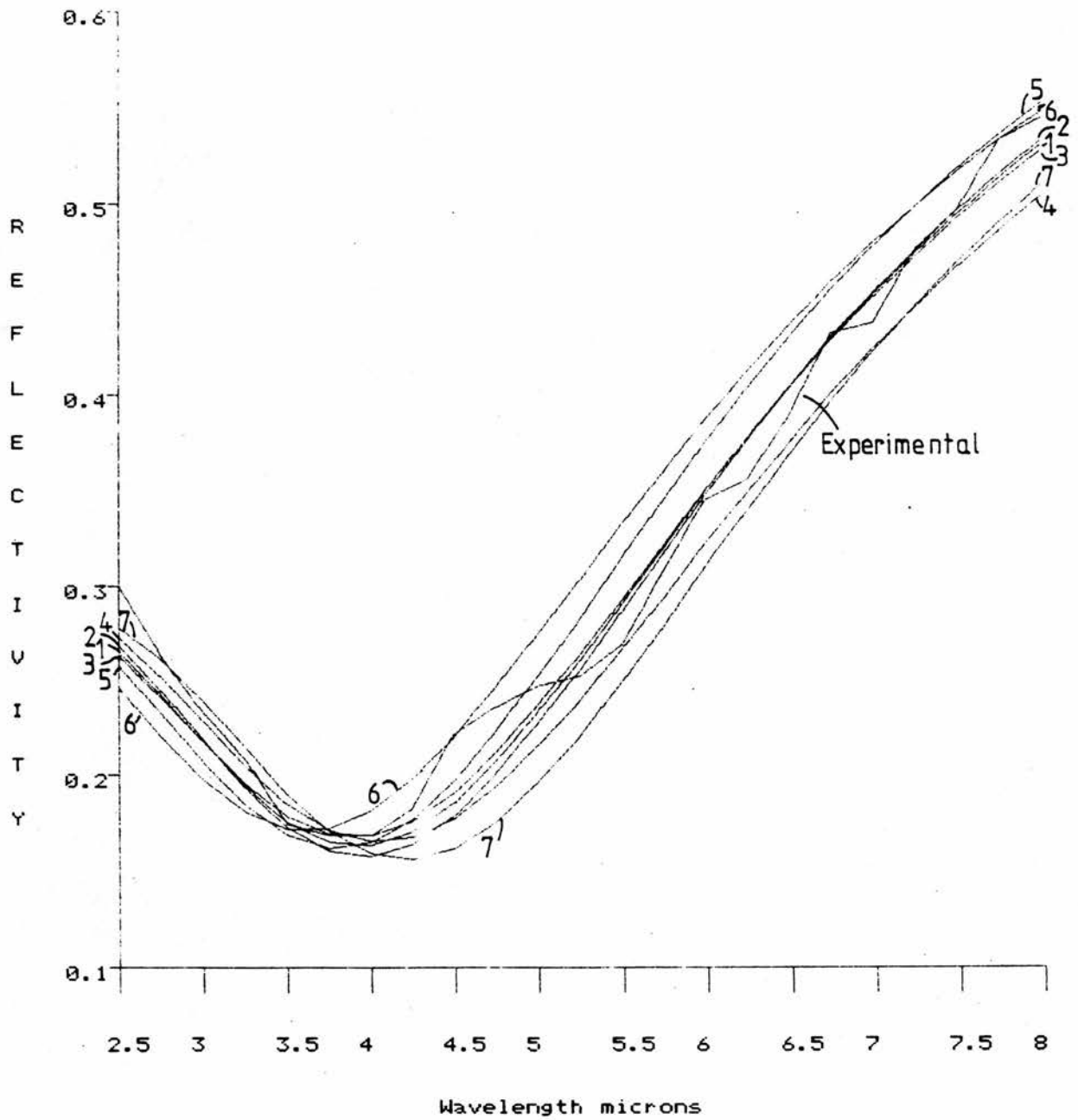
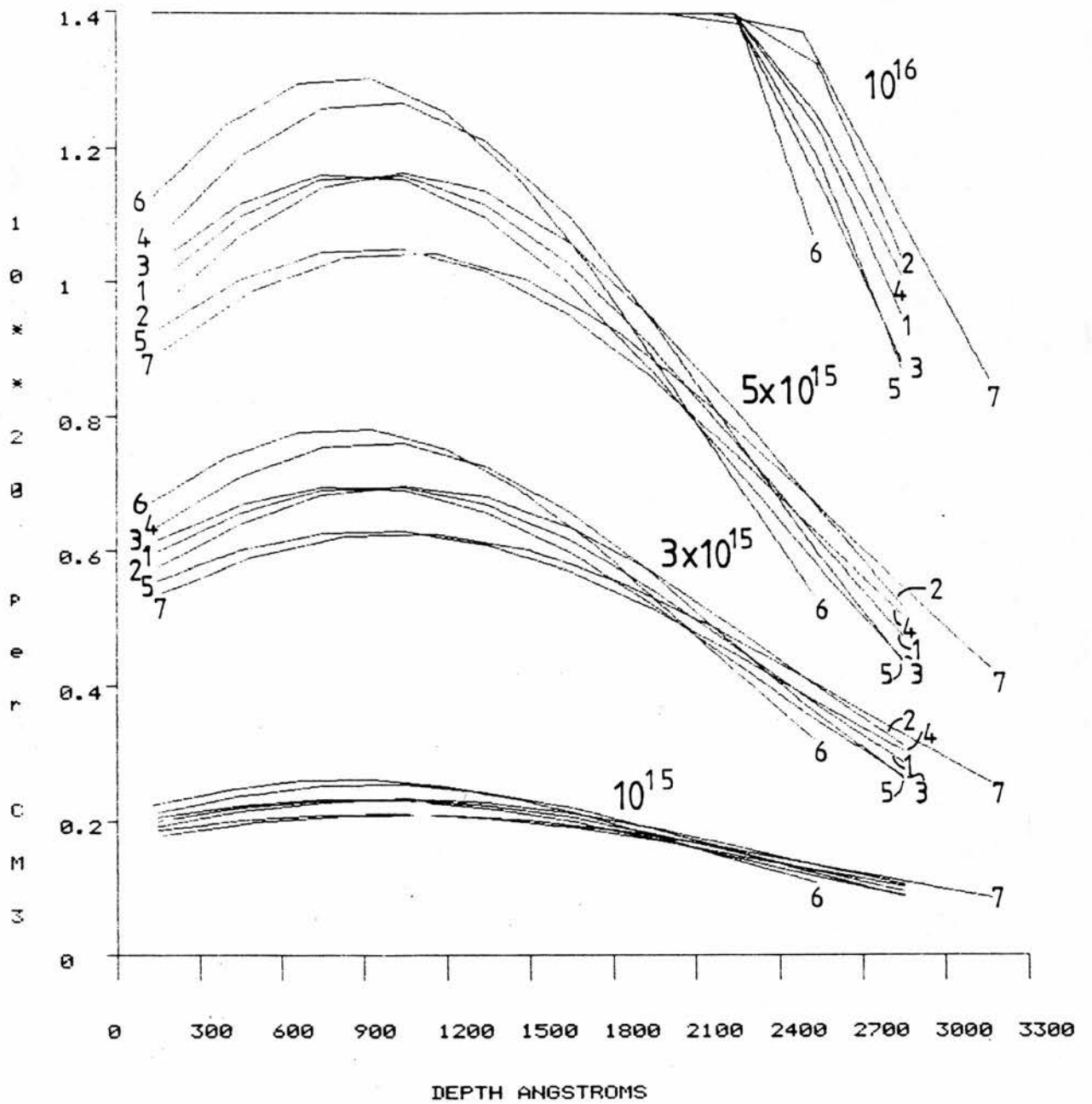






FIGURE 50

Electron concentration vs depth



## CHAPTER 6

TABLE 11

Implant Distribution Values Used in Figures 49 &amp; 50

(See Chapter 2 for definitions of mean etc.)

Curve number	Maximum Depth (Å)	Mean (Å)	Standard Deviation (Å)	Parameter changed
1	3000	1000	1500	None
2	3000	1100	1500	Mean
3	3000	900	1500	Mean
4	3000	1000	1650	Sigma
5	3000	1000	1350	Sigma
6	2700	900	1350	Depth
7	3300	1100	1650	Depth

For the highest dose implant of  $10^{16}$  ions/cm<sup>2</sup> another fitting parameter is used to limit the maximum electron concentration, the 'cutoff' number. This is assumed in earlier calculations to be  $1.4 \times 10^{20}$  electrons/cm<sup>3</sup>. For a dose of  $10^{16}$  ions/cm<sup>2</sup> figure 51 a) shows the effect on reflectivity of varying this parameter from  $1.1 \times 10^{20}$  to  $1.7 \times 10^{20}$  electrons/cm<sup>3</sup>. Figure 51 b) shows the plots of electron concentration with depth for these different 'cutoff' values.

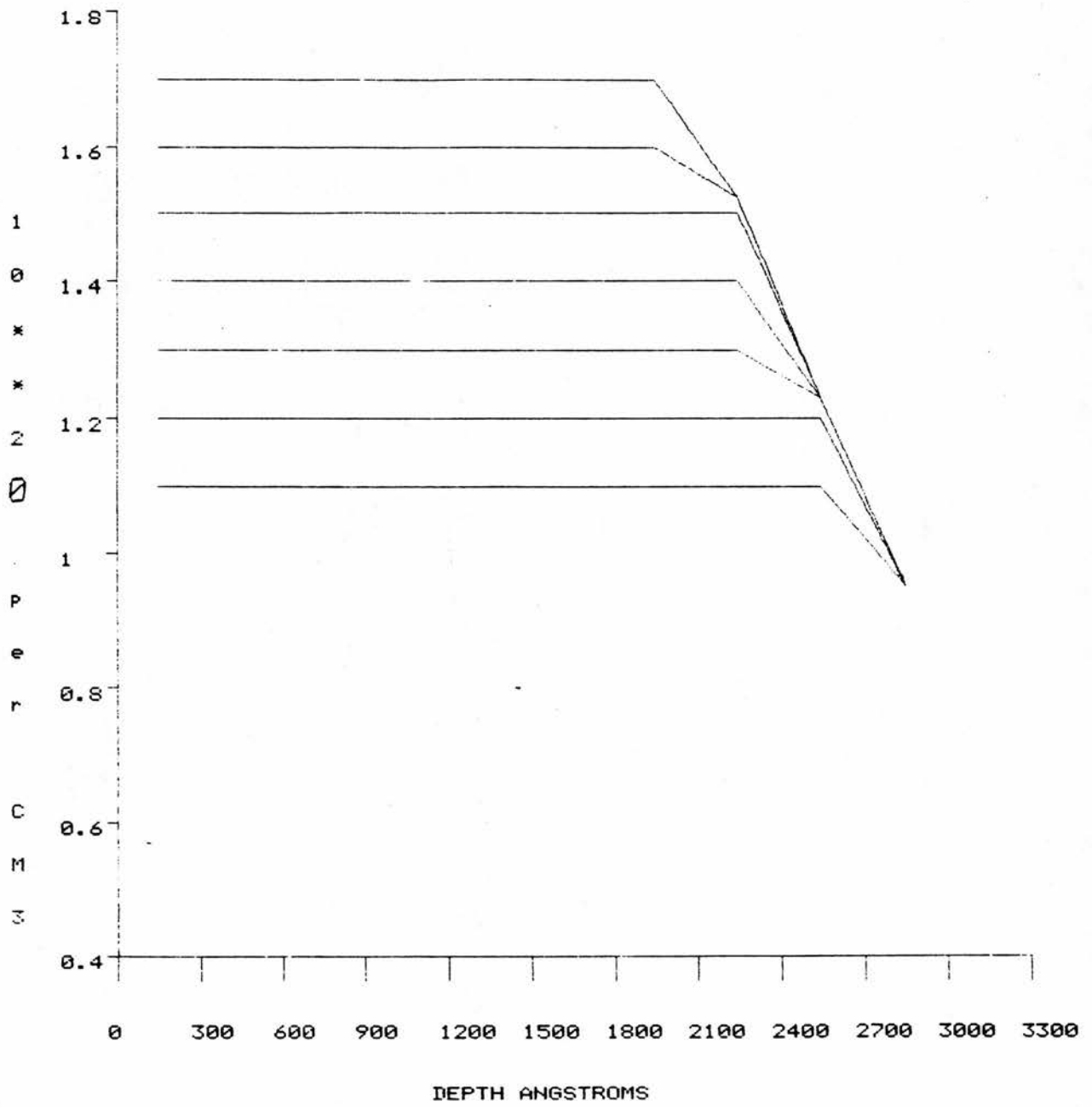
Figures 49 a), b), c), d) and 51 a) show that 10% changes in the fitting parameters give noticeable changes in the predicted reflectivities for the doses greater than  $10^{16}$  ions/cm<sup>2</sup>. The maximum dose of  $10^{16}$  ions/cm<sup>2</sup> is strongly affected by the 'cutoff' concentration value as well as by the other fitting parameters.

This shows that the characterisation of the implant distribution in the near infrared requires high doses to give large effects in reflectivity from small changes in implant distribution.



FIGURE 51b

Electron concentration vs depth



CHAPTER 6

Figures 52 a), b), c) and d) show similar results to the above for the Plessey implanted samples. Table 12 lists the parameters used to model sample MSO61/TP4 (curve 1) and the variations on this (curves 2 to 7). Table 13 does this for sample MSO38/1. See page 37 for sample details.

TABLE 12

Implant Distribution Values Used in Figures 52 a) & c)  
(See Chapter 2 for definitions of mean etc.)

Curve number	Depth (A)	Mean (A)	Standard Deviation (A)	Parameter changed
1	1800	18	900	None
2	1800	20	900	Mean
3	1800	16	900	Mean
4	1800	18	1000	Sigma
5	1800	18	800	Sigma
6	1600	16	800	Depth
7	2000	20	1000	Depth

TABLE 13

Implant Distribution Values Used in Figures 52 b) & d)  
(See Chapter 2 for definitions of mean etc.)

Curve number	Depth (A)	Mean (A)	Standard Deviation (A)	Parameter changed
1	1800	450	300	None
2	1800	600	300	Mean
3	1800	360	300	Mean
4	1800	450	360	Sigma
5	1800	450	260	Sigma
6	1500	375	250	Depth
7	2100	525	350	Depth

For MSO38/1 the parameters are varied by 20% and still give only small changes in the predicted reflectivities. The

FIGURE 52a

Ion-implanted Silicon  
MS061/TP4

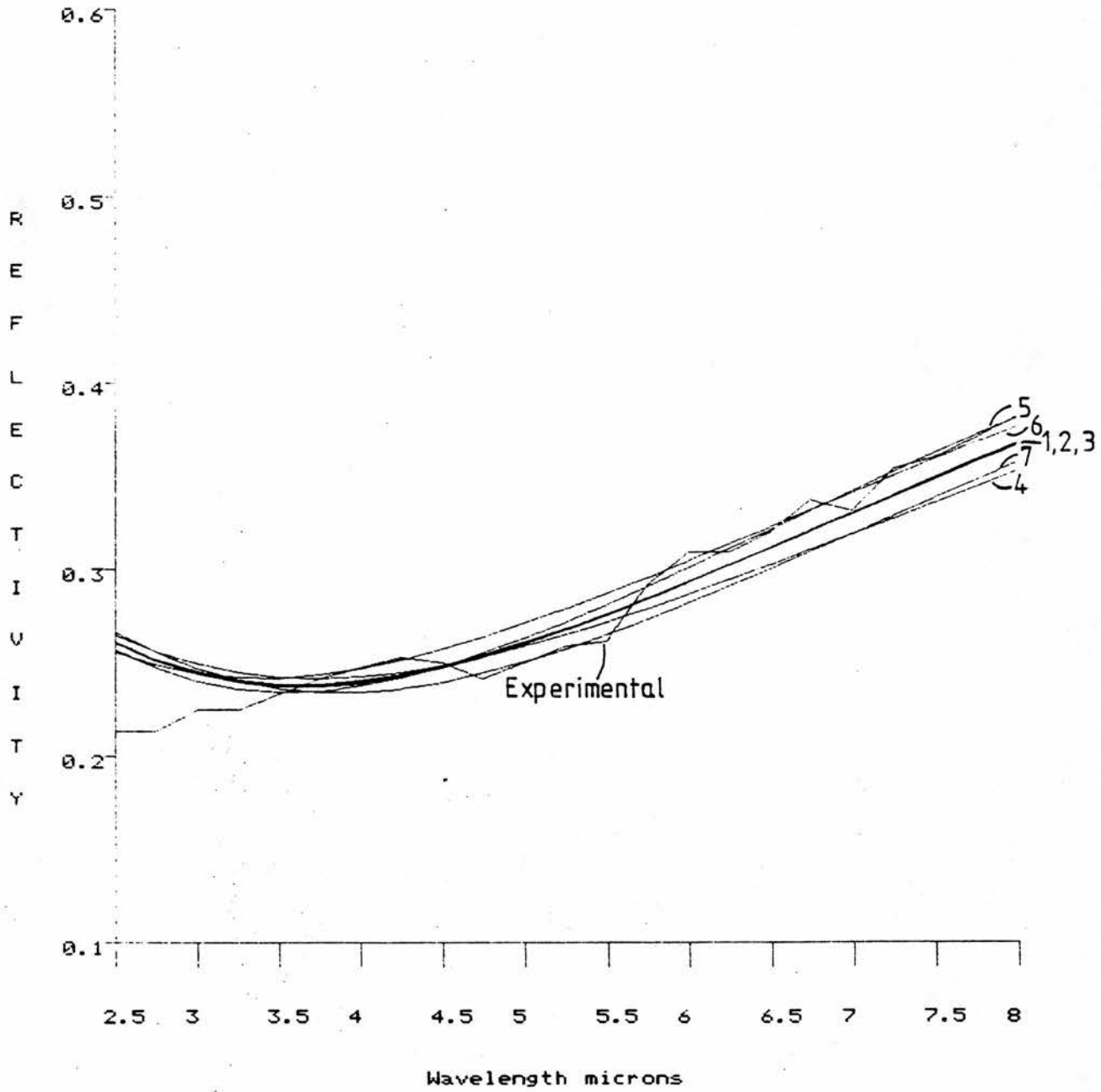


FIGURE 52b

Ion-implanted Silicon

MS038/1

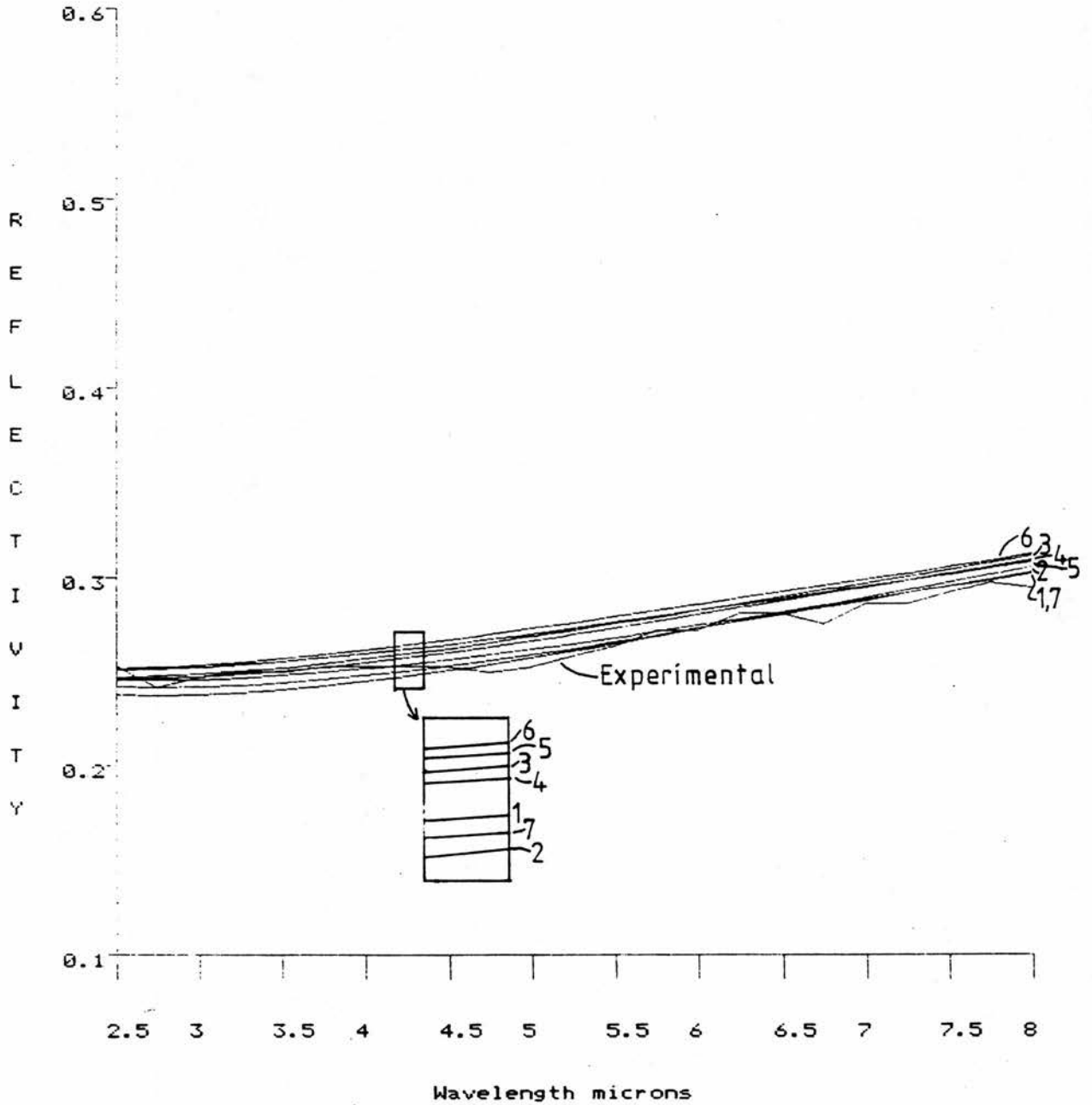


FIGURE 52c

Electron concentration vs depth

MS061/TP4

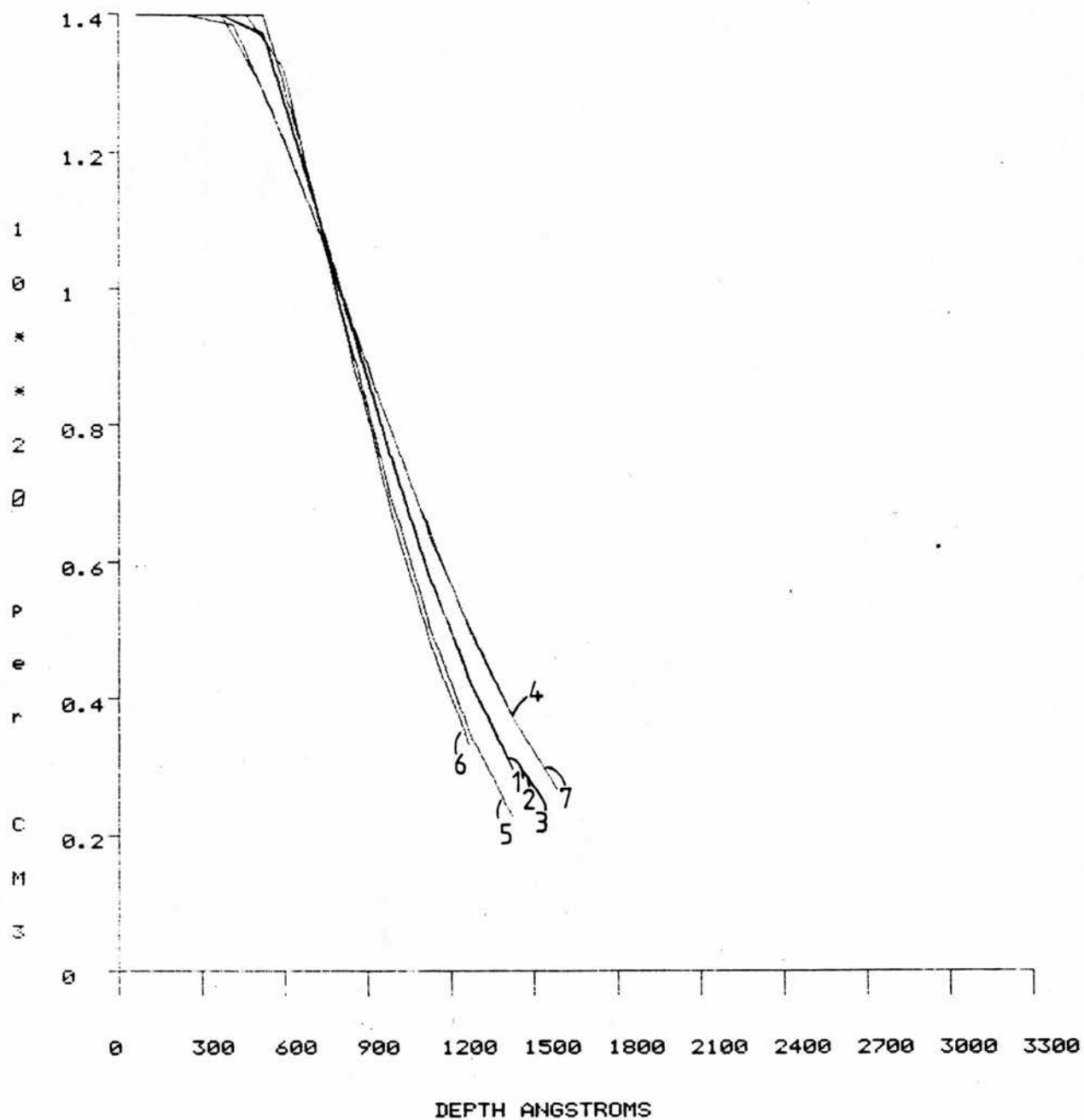
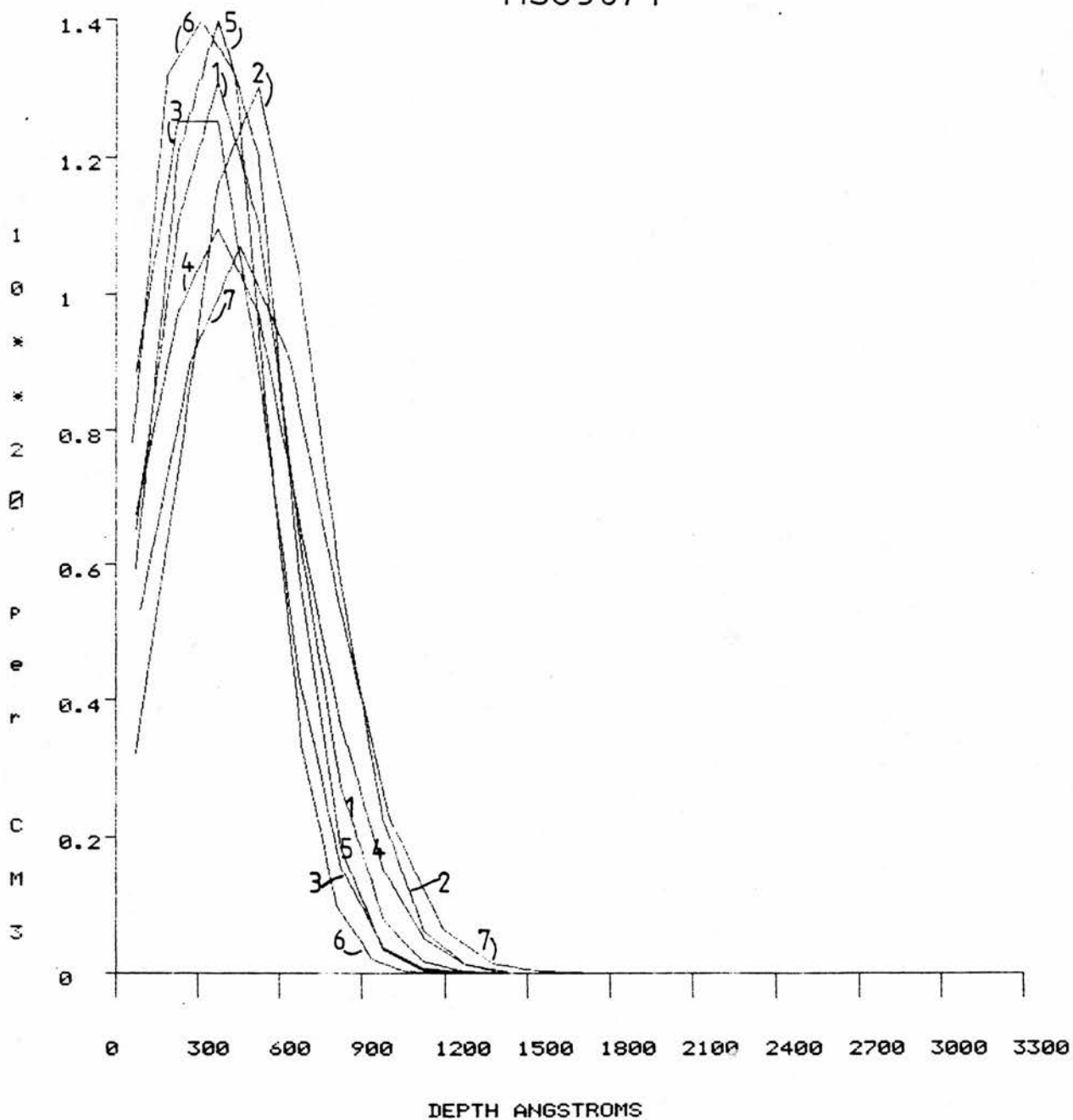


FIGURE 52d

Electron concentration vs depth

MS038/1



theoretical results for MSO38/1 indicate that for accurate modeling of an activated implant distribution with depth, larger implant depths than 1000 Å to 2000 Å are needed, or that the anneal stage should be used to drive the implant deeper.

In a production environment (chapter 1 page 12) an absolute measure of electron concentration with depth is not always needed. What may be wanted is a means of checking that an implanted and annealed wafer is suitable for production before the processing continues and more money is invested in it. This requires that optical properties of the wafer over the range investigated can be used to point out any deviation in the implant profile. Figures 49 to 52 show that this is possible since even doses of  $10^{15}$  ions/cm<sup>2</sup> do show variations in reflectivity for small changes in implanted profile.

### Discussion

The multilayer optical theory developed in chapter 2 and implemented in chapter 3 can be fitted to the experimental reflectivity data in the near-infrared and from this the implanted ion distribution can be found. The optimisation section of this chapter shows that, for donor implants of  $10^{15}$  ions/cm<sup>2</sup> and below, the fits are becoming inaccurate in the near infrared. The far-infrared results still give a clear indication of the dose down to a limit of  $2 \times 10^{14}$  ions/cm<sup>2</sup> (chapter 3 page 32). The near infrared fitting results are confirmed by the strip and probe measurements performed by Plessey. Near to mid-infrared Fourier transform spectrometers with dedicated computers are available. They can rapidly measure the optical constants of a wafer over a range of wavelengths, analyse the results and with a suitable programme (e.g. appendix A with a minimisation routine built in) calculate the implanted ion distribution vs. depth.

## CHAPTER 6

For use in a production environment, where the emphasis is on reproducibility, this type of measurement can give a rapid assesment of the variation of an implanted profile from that required.

The theory also covers the far-infrared transmission and reflection spectra but performs less well with the higher dose implants, particularly on the reflection data (Chapter 5 page 48). This could be due to the less precise nature of the reflectivity experiment where the results were dependent on sample size and orientation, unlike the transmission experiment.

In the discrete laser measurements the sample thickness is crucial for the calculation of accurate figures. However, from the predictions given in chapter 3 (figures 18 and 21), the transmission modulation drops considerably, as the implant dose increases, and the average values predicted compare well with the experimental results. This will allow the real time monitoring of implant dose in a production environment using only a couple of discrete wavelengths once a simple equipment calibration has been performed to remove the effect of wafer thickness variations. As mentioned earlier the interference effects multiply the absorption from the implanted layers and increase the dose measurement sensitivities. This is particularly useful for low dose implants.

The millimeter wave measurements are in close agreement with the theory and could also be used for the evaluation of dose. In this case the wafer size variations still need to be taken into account.

This is not so true for the centimeter wave results; here the wafer thickness is not so important. The discrepancy between the measured and predicted results is due to the use of waveguide matching techniques to optimise the transmission in the experiment whilst the theory is for free space applications. An approach to the problem using bounded centimeter wave propagation theory should allow a better prediction of transmission to be made, and thus, with the

CHAPTER 6

insensitivity to wafer thickness. centimeter wave measurements may be the preferred solution where only a measure of implanted dose is required.

The results for Boron implants presented in chapter 5 page 42 showed a much smaller variation of reflectivity at short wavelengths with implanted dose. The lower mobility of holes in silicon over electrons is one reason for this. Another reason is shown in table 14 below. Boron has over twice the range of phosphorous in silicon and a greater spread. This will reduce the peak carrier concentration and so reduce the modulation in the near infrared reflectivity.

TABLE 14

Ion-Implantation Ranges and Spread [27]  
For Silicon

Implant Energy (KeV)	Phosphorous		Arsenic		Boron	
	Range (nm)	Spread (nm)	Range (nm)	Spread (nm)	Range (nm)	Spread (nm)
10	12.8	7.4	9.9	3.7	31.0	19.3
20	24.3	12.9	16.4	6.0	63.4	31.8
30	35.9	18.1	22.5	8.1	95.6	41.4
40	47.9	23.2	28.4	10.1	127.0	49.2
50	60.1	28.0	34.3	12.1	157.4	55.6
60	72.6	32.7	40.0	14.0	186.8	61.0
70	85.2	37.2	45.8	15.9	215.3	65.7
80	97.9	41.5	51.6	17.7	242.9	69.9
100	123.8	46.8	63.1	21.4	295.6	76.8
120	149.9	57.5	74.7	25.0	345.6	82.5
140	176.2	64.8	86.3	28.6	393.3	87.2
160	202.6	71.5	98.0	32.1	438.9	91.3
180	228.9	77.8	109.7	35.6	482.8	94.8

## CHAPTER 6

Comparing the dose profiles obtained in this thesis with those calculated in Runge [27] gives the following results. The ranges and spreads into  $\text{SiO}_2$  are very similar for each of the above implants. Thus the samples implanted with phosphorous through a 700 Å oxide layer at 180 KeV will have theoretical ranges into the silicon, as calculated by Runge [27], of  $228.9 \text{ nm} - 70 \text{ nm} = 158.9 \text{ nm}$  or 1589 Å, and a spread of 778 Å. This compares very well with the theoretical predictions, in chapter 5 page 44, of 1500 Å mean depth and standard deviation of 1000 Å.

Looking now at the Plessey arsenic results (figure 45 implant energy 30 KeV), the implanted depth prior to anneal at  $1000^\circ\text{C}$  for 25 minutes is about 25 nm. This gave a maximum arsenic atomic concentration of  $2.4 \times 10^{20}$  per  $\text{cm}^3$  for sample MSO38/1. This is well above the solubility limit for arsenic in silicon, chapter 1 page 14. After annealing the peak arsenic concentration was found to drop to  $1.0 \times 10^{20}$  atoms/ $\text{cm}^3$  and the spread depth rose towards 2000 Å. The before anneal profile for sample MSO61/TP4 is not available, but the implant energy was the same. Thus the depth should be the same, with only the peak concentration being greater. The depth from Runge [27] at 30 KeV for arsenic is 22.5 nm. This result is in agreement with the profile derived by this thesis (page 45) and the Plessey profile (figure 45).

The higher energy implant of the Hughes Microelectronics samples gives rise to a deeper ion penetration depth and lower, unannealed, peak concentration. This resulted in less diffusion when the samples were annealed and a correspondingly closer agreement with the ranges given by Runge [27].

Conclusions

The results overall show that reflectivity and transmission measurements in the near infrared, far-infrared and microwave, followed by curve fitting, provide a cheap, fast and accurate alternative to destructive analysis, allowing the distribution of electron concentration with depth for ion-implanted donors in silicon wafers to be mapped. For production use an initial assessment of an implant distribution by destructive means will provide a basis for the fitting parameters. Further implanted wafers can then be compared with the standard using near infrared to microwave techniques. The advantages are:

- i) The wafers do not have to be prepared in any way e.g. by polishing.
- ii) The techniques described are contactless. Thus wafer contamination and damage (e.g. by four point probe introducing extra dislocations) is eliminated.
- iii) Being non destructive the wafers are available afterwards for continued processing. This should reduce the need for calibration and quality check runs by the ion-implanter, giving increased output.
- iv) The processing of wafers in this way is rapid and opens up the possibility of implant evaluation over the entire surface of the wafer giving information on positional consistency.

Solubility limits for arsenic and phosphorous implanted and annealed in silicon appear to be similar at about  $1.4 \times 10^{20}$  atoms/cm<sup>3</sup>. Above this 'cutoff' concentration any additional implanted ions provide no more electrons. Thus the extra time spent performing the higher dose implant is unproductive and indeed may cause deterioration in the electrical or structural properties.

Further work

The techniques could be extended to include the possibility of fitting to non-gaussian implants e.g. multiple implants at differing energies, an implant plus a drive in anneal stage, a channelled implant, or a more sophisticated fit to the standard implant. As more understanding of the theoretical implant distribution is built into the computer programme the correct class of implant distribution curve can be fitted to the sample data. The curve fitting results, of experimental data, will then be more accurate.

The work could also be extended to acceptor implants which appear to give a smaller modulation in the short wavelength optical properties because of the lower hole mobility and greater ion penetration (table 14 page 61). To enhance the acceptor results' multiple reflections from the wafer could be arranged.

The use of contactless optical techniques opens up the possibility of characterising ion-implantation in a production environment. The characterisation need not only be after implant and anneal, but could be used further along in the processing. Imaging optics would allow the investigation of small areas, permitting x-y scans, limited by the spot size projected onto the wafer, and the reflectivity/transmission distortion caused by the variation in angle of the incident light.

## CHAPTER 7

### BAND STRUCTURE

#### Introduction

Chapters 7 and 8 cover the application of photoconductive methods to the analysis of level crossings in GaAs.

At 4.2 K the majority of electrons from shallow donors in GaAs are 'frozen' into the ground state energy level around the donor impurities. Incident optical radiation of the right frequency excites these electrons into higher energy levels. Under the application of a magnetic field these are Zeeman split. Calculations by Aldrich and Green [30] (the results of which are presented in figure 53) show that, at certain magnetic fields, different inter-state transitions have the same energy, and the possibility exists of these two states interacting. Investigation of the photoconductive intensities for observable transitions could provide the opportunity to view forbidden transitions and thus collaborate the theoretical calculations.

#### Theory

##### Effective mass

GaAs crystallizes in the zinc-blend structure (Figure 54) and has a direct band gap located at the  $\Gamma$  point (Figure 55 and 56).

To a first approximation the dependence of the conduction band energy,  $E(k)$ , on wavevector,  $k$ , is parabolic. This assumption allows the effective mass to be treated as a scalar with respect to  $E(k)$  and  $k$ . With the effective mass defined as [26]:

$$E(k) = \hbar^2 k^2 / (2 \cdot m^*)$$

47

# FIGURE 53

Computed Transition Energies For a Donor In a  
Magnetic Field.

From Variational Calculations by Aldrich and Greene [30]

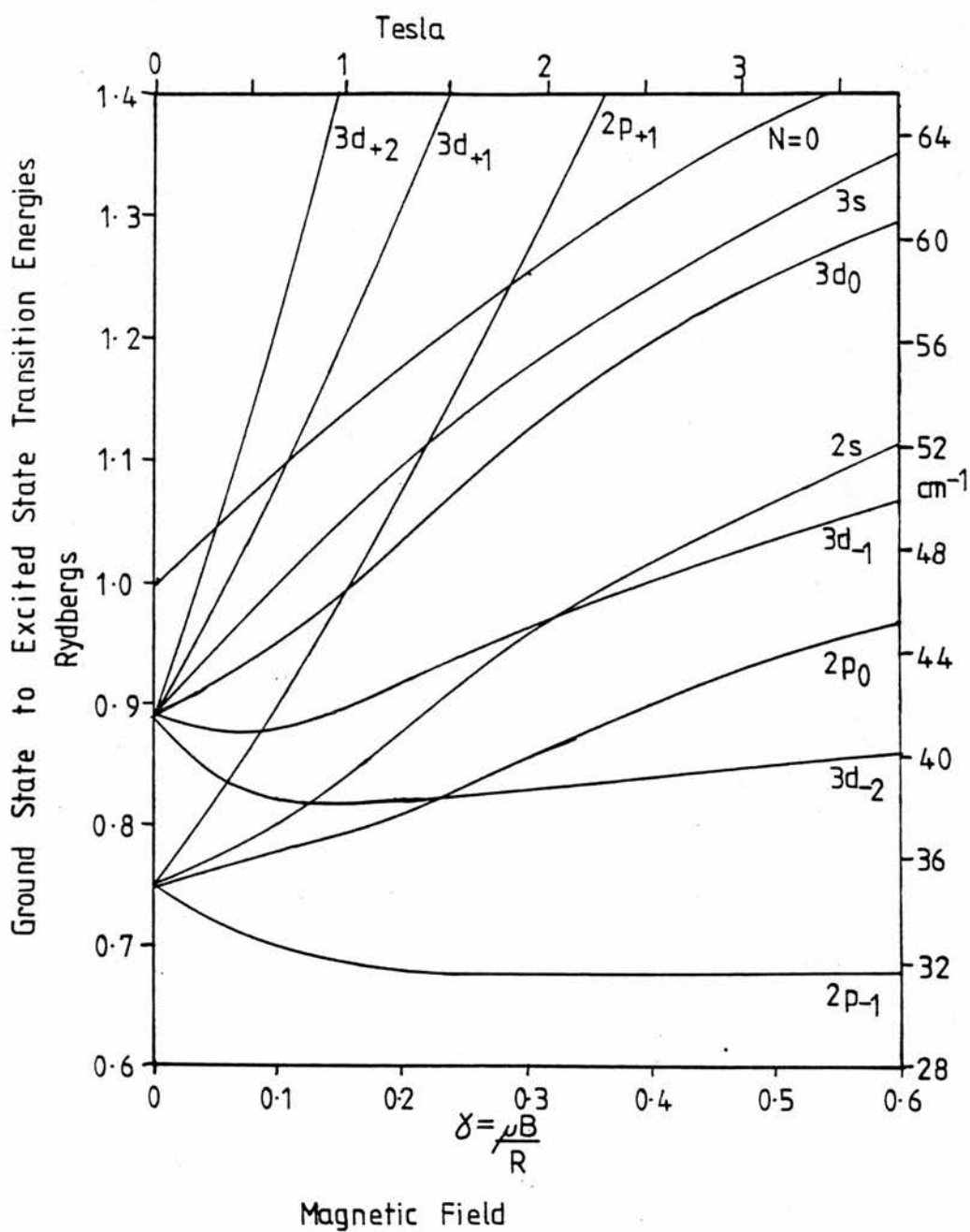


FIGURE 54

Crystal Structure of GaAs [32]

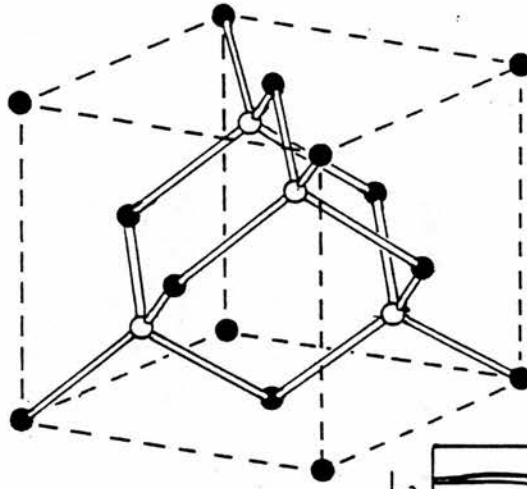


FIGURE 55

Band Structure of GaAs [31]

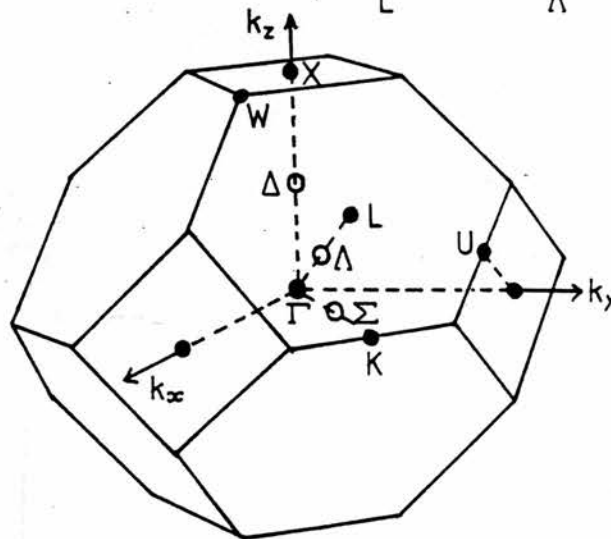
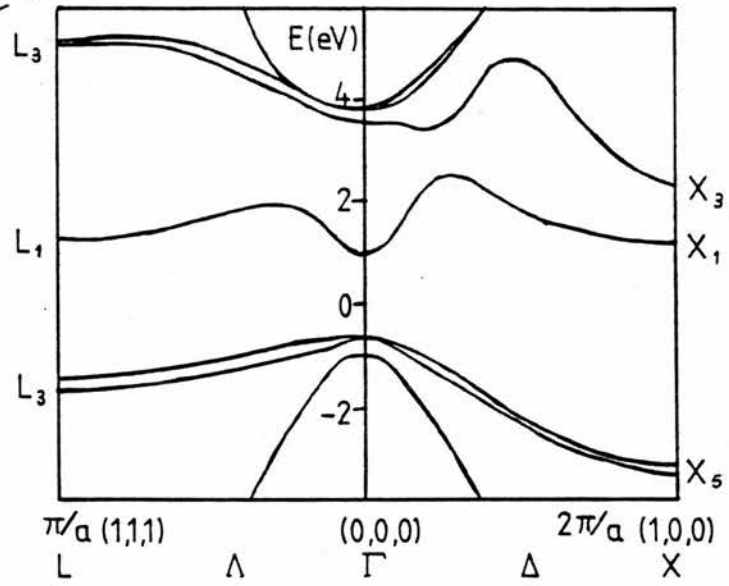


FIGURE 56

Brillouin Zones of the Face Centred Cubic Lattice [32]

## CHAPTER 7

Several definitions [28] exist for the effective mass but for the following sections no detailed knowledge of these is needed.

### Hydrogenic Model for Impurity States [29]

The simple Hydrogenic model can be used to estimate the donor binding energy. In this model a donor atom, relative to the host atom it replaces, has one extra positive charge on its nucleus. The extra electron and positive charge in the host material is analogous to a hydrogen atom in vacuum, except that the electron is moving in a dielectric medium, with a consequent modification of the Coulomb potential and that the effects of the crystal lattice must be incorporated in the form of an effective mass.

For a neutral hydrogen atom in vacuum

$$E_n = -R_0/n^2 \text{ and } a_n = a_0 n^2 \quad 48$$

$$R_0 = 13.6\text{eV and } a_0 = 5.3 \times 10^{-11} \text{m}$$

Including the effective mass and the host lattice dielectric constant gives

$$E_d = -R_0/n^2 \times (m^*/m)/\epsilon^2 \text{ and } a_d = a_0 n^2 \times \epsilon/(m^*/m) \quad 49 \ \& \ 50$$

$$E_d = \text{donor energy and } a_d = \text{donor radius}$$

For a cubic crystal with the conduction band minimum at the centre of the Brillouin zone, e.g. GaAs (figure 55), the effective mass,  $m^*$ , is isotropic.

## CHAPTER 7

In this simple state the hydrogenic model predicts the same energy level diagram for any impurity. For the excited levels this is generally a very good approximation, but for the ground state these approximations can break down.

The effective mass approximation assumes that the electron wavefunction interacts with a periodic potential, whilst the hydrogenic model assumes that the impurity core electrons screen the full nuclear charge, and, that a macroscopic dielectric constant is appropriate.

For the ground state the electron wavefunction has a finite amplitude within the core electrons (Figure 57). Thus the wavefunction is perturbed by the unique impurity core potential which is ineffectively screened. In addition the ground state wavefunction occupies a small volume centered upon the impurity; the impurity strains the crystal lattice and this affects the periodic potential, which can in some circumstances result in a change of the apparent effective mass. At small distances, relative to the inter-atomic spacing, the macroscopic dielectric constant is inapplicable and  $\epsilon \rightarrow 1$ .

Each chemically unique impurity has its own core potential and lattice strain, thus the perturbation of the ground state electron wavefunction is impurity type dependent (Figure 58).

This energy shift is referred to as the chemical shift or the central cell effect. In the extreme limit the local potential will dominate over the long range Coulomb term, the effective mass approximation breaks down, and the impurity level becomes 'deep'. The remainder of the thesis will be concerned with the properties of 'shallow' or near hydrogenic levels.

In far-infrared experiments, if more than one impurity is present, these shifts appear as additional shoulders or splittings of the ground state to excited state transitions (Figure 59).

FIGURE 57

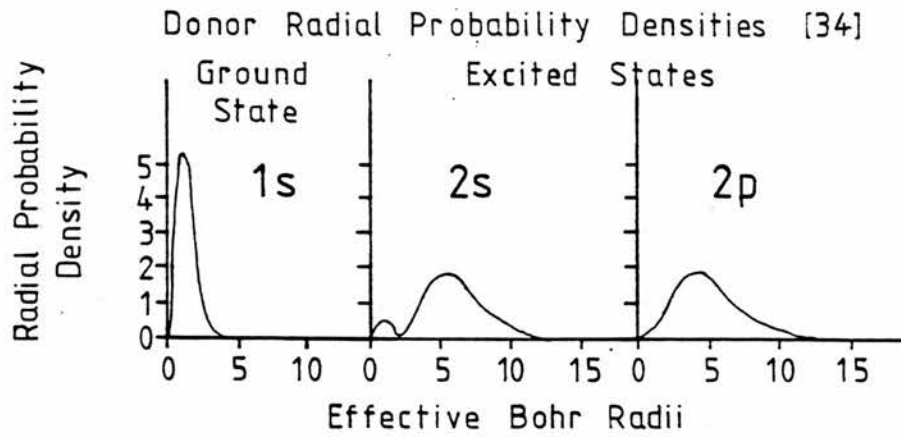


FIGURE 58

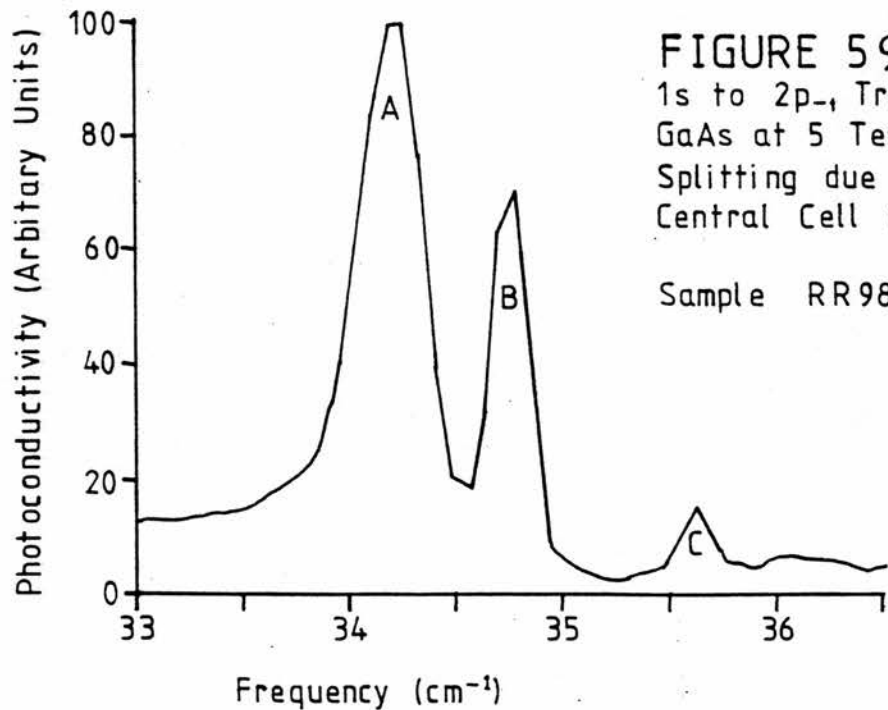
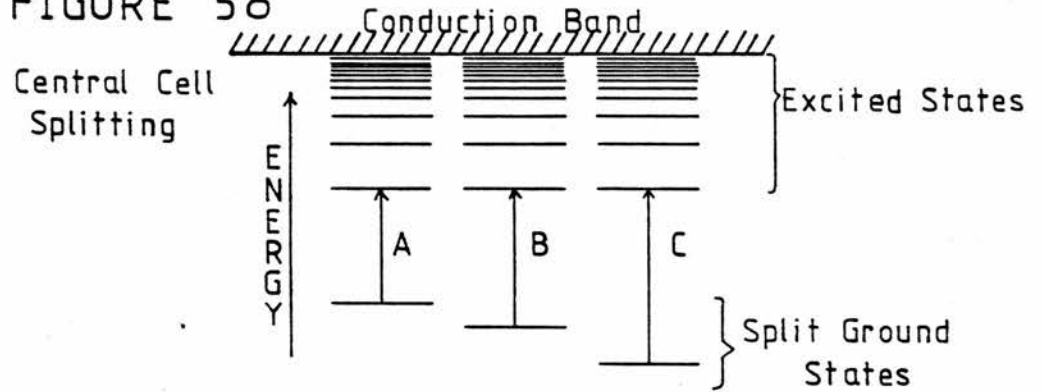


FIGURE 59

1s to 2p<sub>-</sub> Transition in GaAs at 5 Tesla. Splitting due to the Central Cell Effect.

Sample RR98B

Higher doping levels or the formation of molecular complexes can also lead to deviations from the hydrogenic model. e.g. For two donors close together, their electron wave functions can overlap and form the solid state analogue of the hydrogen molecule. This leads to the observation of transitions of lower energy than the ground to first excited state of an isolated donor.

### Magnetic Field Effects

#### Zeeman Splitting

An impurity atom has a net magnetic moment,  $\mu$ , due to the spin and orbital magnetic moments of its excitable electron. When this magnetic moment is in an external magnetic field,  $B$ , it will have an orientational potential energy.

$$\Delta E = -\mu \cdot B = -\mu_B H \quad 51$$

$\mu_B$  is the component of  $\mu$  along the direction of  $B$

Each energy level will be split into several energy levels corresponding to the several possible values of  $\mu_B$ .

This parallels the case of the hydrogen atom, but the splitting is greater due to the lower electron effective mass and the higher dielectric constant.

In a magnetic field the different spin states rapidly decouple into 'spin-up' and 'spin-down' ladders. If the spin-orbit or inversion terms are small, then the probability of a 'spin-flip' transition is also small. The energy difference between a transition in the spin-up ladder and the equivalent transition in the spin-down ladder is small and mainly arises from the non-parabolicity of the associated band.

## CHAPTER 7

Using  $\gamma = \mu B/R$  then for hydrogen,

$$\gamma = 0.1 \text{ requires } B = 23,000 \text{ Tesla}$$

whilst for GaAs with  $\gamma = 0.1$  requires  $B = 0.63$  Tesla. At  $\gamma = 0$  the  $1s$  to  $2p_{-1}$  and  $1s$  to  $2p_{+1}$  transitions require equal energies. At  $\gamma = 0.1$  the  $1s$  to  $2p_{+1}$  transition requires 29% more energy than the  $1s$  to  $2p_{-1}$  transition.

Variational calculations by Aldrich and Greene [30] with intermediate values calculated by P. Makado provide theoretical values for the  $1s$  to  $4f$  levels in arbitrary magnetic fields, figure 53.

### Landau Levels [31]

When a magnetic field,  $B$ , is applied to a sample, the motion of the conduction electrons changes. The electron experiences a Lorentz force perpendicular to it's velocity and the applied magnetic field. Classically the equation of motion is

$$m(d^2\mathbf{r}/dt^2) = e (d\mathbf{r}/dt) \times \mathbf{B} \quad . \quad 52$$

The component along  $B$ , (taken as the  $z$ -direction) gives free, constant motion

$$m(d^2r/dt^2) = 0 \quad 53$$

However in the plane perpendicular to  $B$ , the electron moves in a circle with radius  $R$

$$m^*\omega^2 R = e\omega R B \quad 54$$

which gives

$$\omega_c = eB/m^* \quad 55$$

$\omega_c$  is the cyclotron frequency

The quantum mechanical derivation quantises the energy of motion

$$E_{L_n} = (n + 0.5)\hbar\omega_c \quad 56$$

with  $n$  an integer  $0, 1, 2, \dots$  (Fig. 60)

The  $N = 0$  energy is also plotted on figure 53

### Photoconductivity

Photoconductive spectroscopy with certain approximations, covered later, provides essentially the same information as absorption spectroscopy, but with a higher sensitivity.

When a doped semiconductor carrying constant current absorbs photons (figure 61) through the excitation of carriers, the conductivity changes by  $\Delta\sigma$ . This causes a change in voltage across the sample given by

$$\Delta V/V_0 = \Delta\rho/\rho_0 = -\Delta\sigma/\sigma_0 \quad 57$$

$\sigma_0$  is the unilluminated conductivity

$\rho_0$  is the unilluminated resistivity

and  $V_0$  is the bias voltage

$$\sigma_0 = |e| \cdot (n_0\mu_n + p_0\mu_p) \quad 58$$

where  $n_0$  ( $p_0$ ) are the  $N^0$  per unit volume of electrons (holes) and  $\mu_n$  ( $\mu_p$ ) is the mobility of the electrons (holes)

$$\Delta\sigma = |e| \cdot (\mu_n\Delta n + \mu_p\Delta p) \quad 59$$

FIGURE 60

Landau Splitting of the Conduction and Valence Bands. [33]

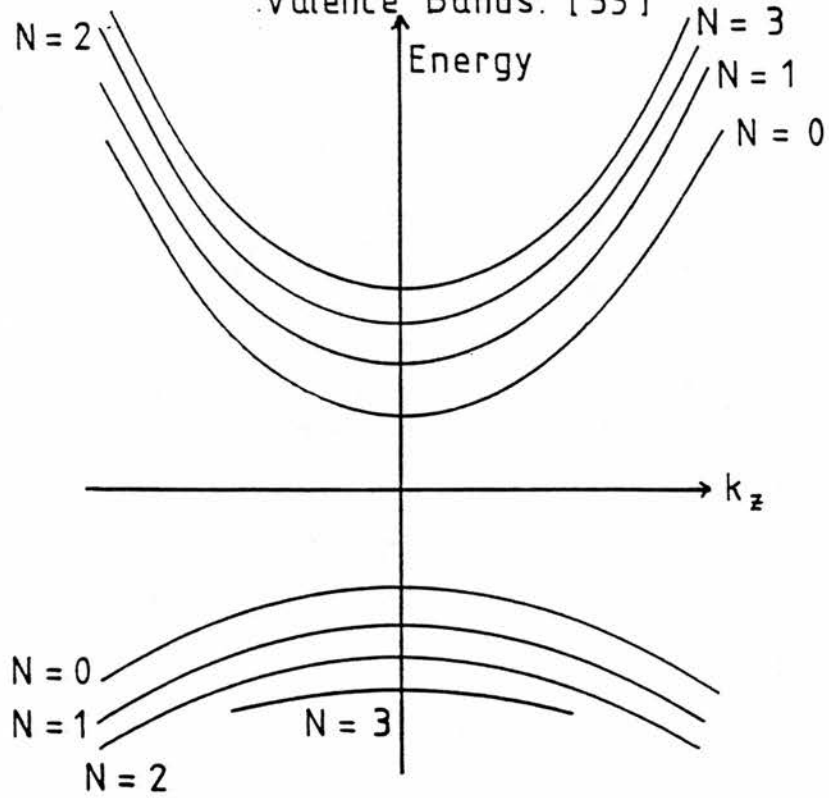
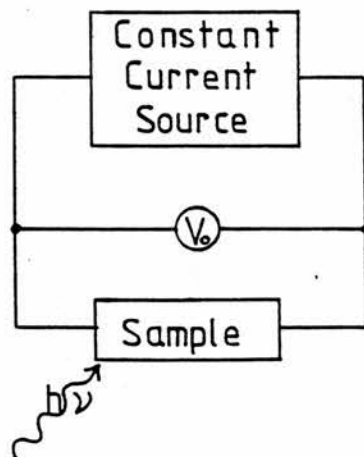


FIGURE 61

Sample Biasing



## CHAPTER 7

Substituting equations 58 and 59 into equation 57 gives

$$\Delta V/V_0 = -\Delta\sigma/\sigma_0 = (\mu_n\Delta n + \mu_p\Delta p)/(\mu_n n_0 + \mu_p p_0) \quad 60$$

on the assumption that the mobility does not change. (In free carrier detectors  $n$  does not change but  $\mu$  does).

The sensitivity of photoconductivity derives from maximising  $\Delta V/V_0$ , which can be achieved as follows:

Reduce  $\sigma_0$  by lowering the temperature thereby reducing thermal excitation of carriers,  $n_0$  &  $p_0$ , to give a large percentage change in conductivity on illumination.

With intrinsic material  $\Delta n$  and  $\Delta p$  not only depend on their generation rate by incident radiation but also on how fast they recombine i.e. a long recombination time gives a larger signal so a good quality sample with few dislocations is required for sensitive work. In an extrinsic n-type semiconductor the recombination is generally on the shallow donors.

$$\Delta\sigma = (\delta N/\delta t) \cdot \tau_{rec.e.} \cdot \mu \quad 61$$

$$= (I/hf) \cdot \tau_{rec.e.} \cdot \mu \quad 62$$

where  $I$  = absorbed intensity, (if all the photons are absorbed and each photon creates an electron).

The difference between absorption and photoconductive spectroscopy is that in the photoconductive case the bound electron absorbs a photon and moves into a bound excited state. The electron then absorbs and emits phonons. This moves it through the excited states until it is thermally ionised and can contribute to the conductivity. Absorption spectroscopy does not require phonon involvement. The probability of thermal ionisation is almost zero for an

electron in the ground state and nearly one for an excited impurity electron.

#### Faraday and Voigt Orientations and Selection Rules [31]

In the Faraday orientation the circular motion of the electrons, as determined by the magnetic field, is in a plane normal to the propagation direction of the incident radiation, figure 62. Whilst in Voigt orientation the circular motion is in a plane parallel to the propagation direction of the incident radiation, figure 63.

Transitions from an s to a p state split by a magnetic field B require the radiation to be polarised left-handed, parallel and right-handed with respect to the direction of the magnetic field, for the states -1, 0, +1 respectively. Thus for the Faraday orientation the  $1s \rightarrow 2p_0$  transition is forbidden. Usually the radiation incident upon the sample is unpolarised but has a well defined propagation direction. The integrating cavity surrounding the sample breaks this restriction to some extent but even so in the Faraday configuration the  $1s \rightarrow 2p_0$  transition is generally found to be much smaller than in the Voigt orientation. In the Voigt geometry all three transitions ( $\Delta m = \pm 1, 0$ ) are allowed.

FIGURE 62 FARADAY ORIENTATION

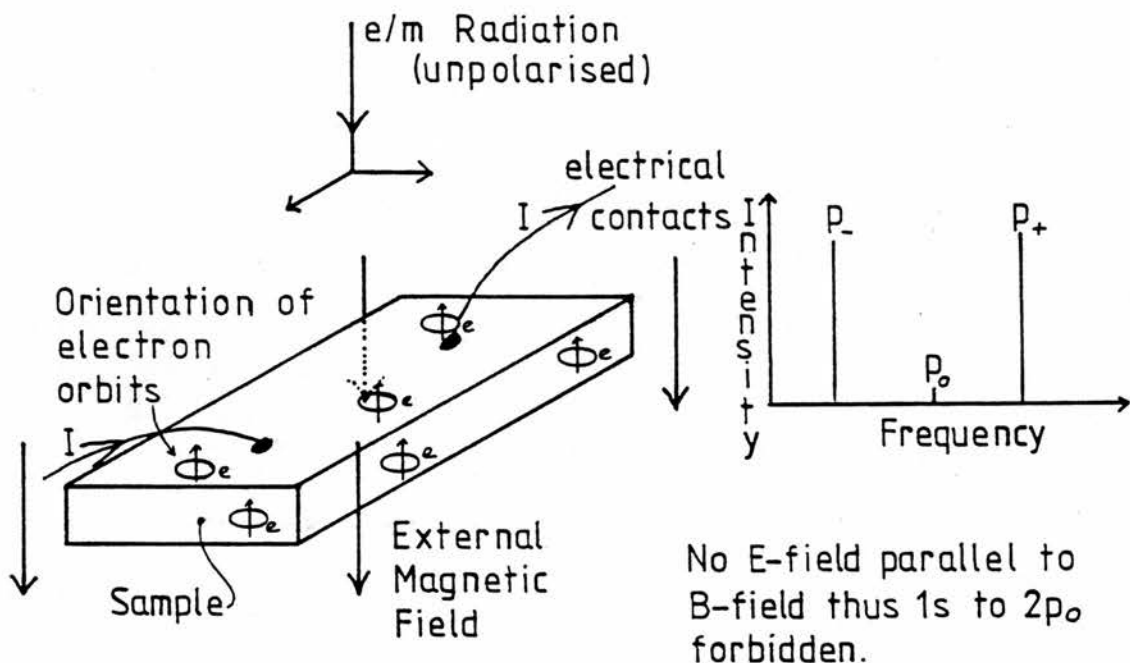
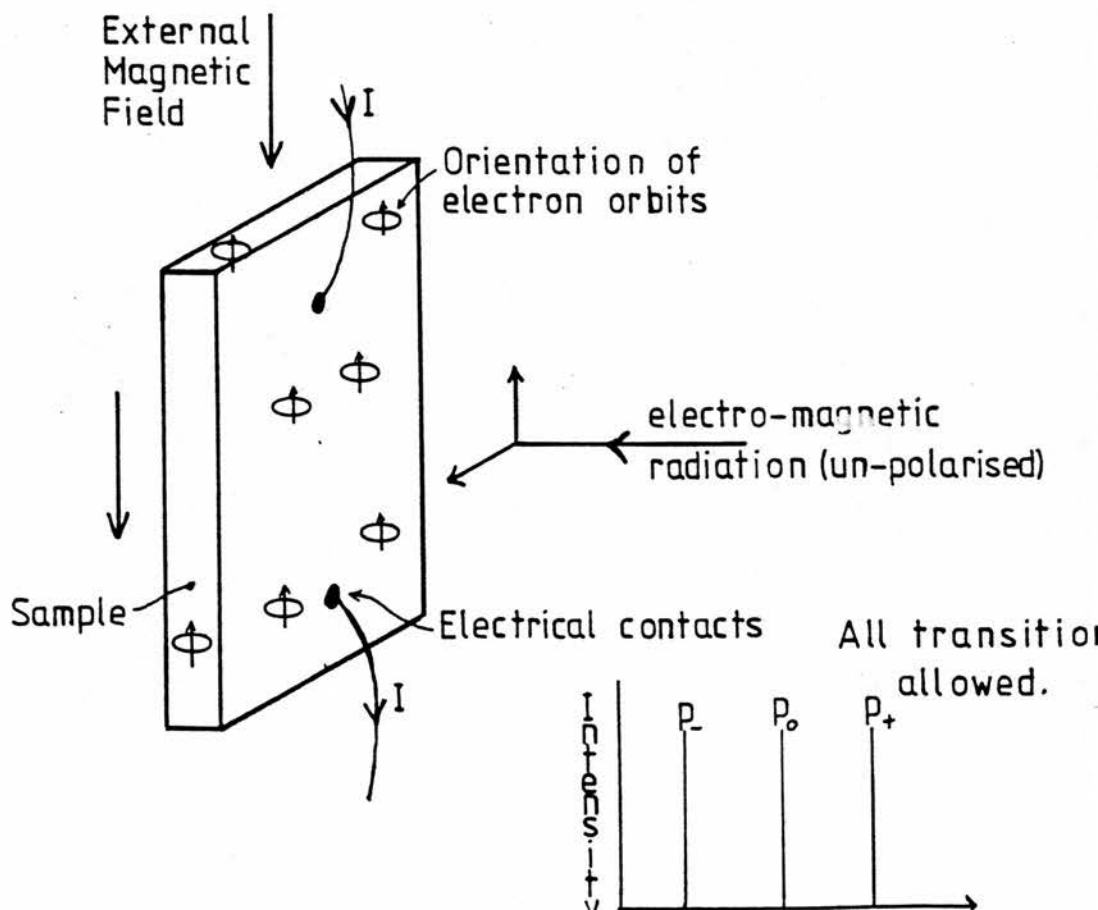


FIGURE 63 VOIGT ORIENTATION



EXPERIMENTAL METHODS - LEVEL CROSSINGSTechnique (Figure 64)

An evacuated Beckman Fourier transform spectrometer with a quartz mercury lamp provided the source of far-infrared radiation. This was modulated at 110 Hz by a tuning fork chopper. The ultra-violet, visible and near infrared radiation was blocked by a black polyethene filter. A 100 gauge beamsplitter (25  $\mu\text{m}$  thick) 'shaped' the far-infrared radiation to the spectral region 10 to 120  $\text{cm}^{-1}$  (Appendix B). The spectrometer output was guided by an evacuated, polished, brass light pipe through a TPX window into a superconducting magnet. Inside the magnet the radiation was guided by a brass light pipe in a helium atmosphere, to a polished copper cone.

The geometry inside the magnet allowed the sample to be placed either parallel or perpendicular to the magnetic field, (Voigt or Faraday orientation). The incident radiation was focused using the light cone and the sample placed in an integrating cavity.

A constant current was passed through the sample and the voltage drop, modulated by the chopped radiation, amplified using a Brookdeal type 450 amplifier, with filters set to 100 Hz and 1000 Hz, followed by a Brookdeal type 411 phase sensitive detector. The interferogram, obtained by sweeping the spectrometer mirror, was stored on an x-t recorder as well as being output digitally to the St. Andrews University's VAX 11/780 computer. The computer performed a digital Fourier transform and the resultant spectra were plotted and displayed as photoconductive intensity vs. wavenumber. The maximum intensity normalised to 100, i.e. absolute intensity information, allowing the direct comparison between samples, is lost in the process of performing the experiment and analysing the results.

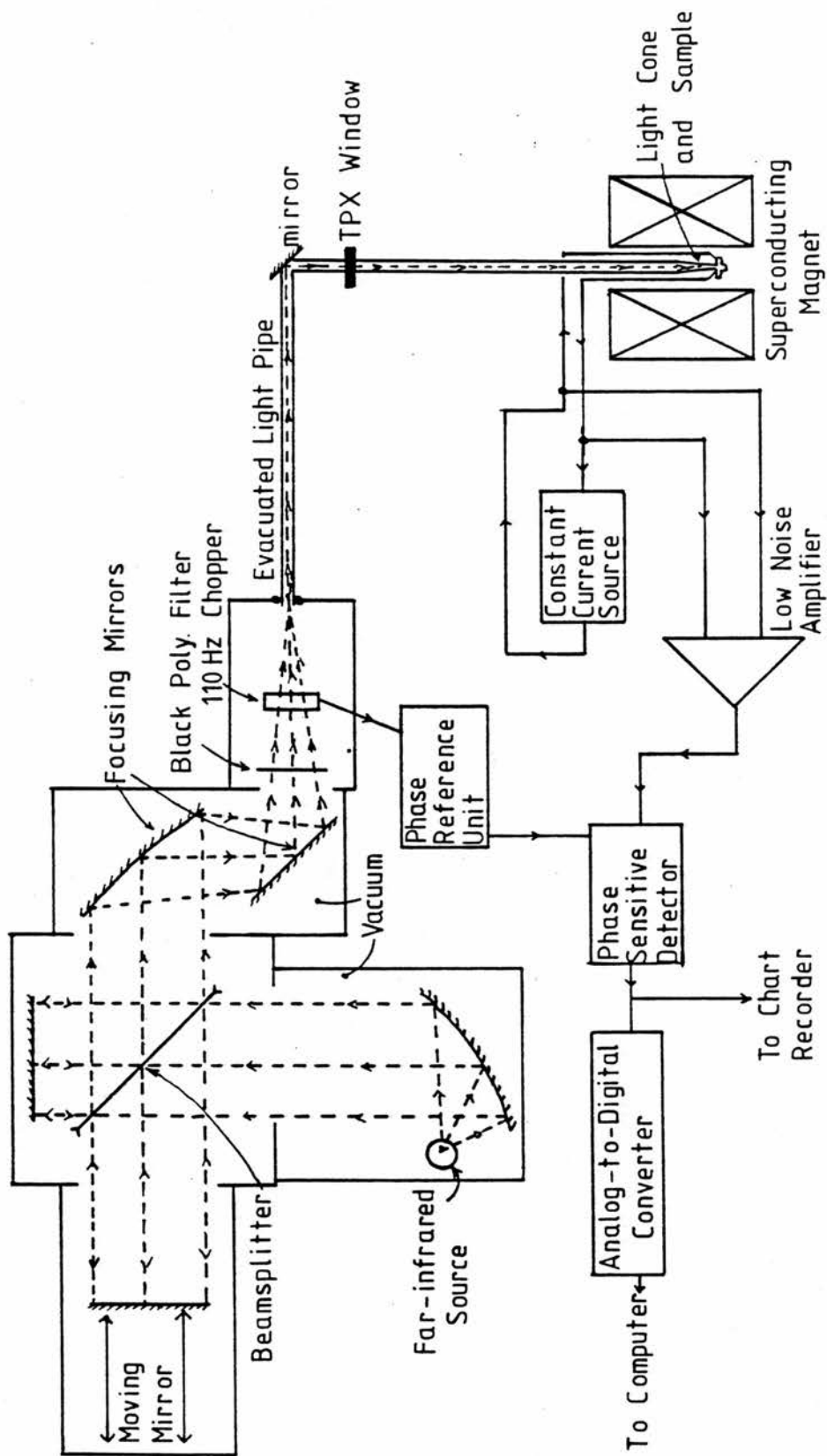


FIGURE 64 Experimental Arrangement For the Study of Level Crossings in GaAs

Experimental Objectives

In n-type GaAs at 4.2 K and 1.45 Tesla the Aldrich-Greene calculations [30] give the  $1s \rightarrow 2p_0$  transition as having the same energy as the  $1s \rightarrow 3d_{-2}$  energy difference and the  $1s \rightarrow 2p_{+1}$  transition matches the  $1s \rightarrow 3s$  energy difference. At 1.85 Tesla the  $1s \rightarrow 2p_{+1}$  transition energy is equal to the energy of the  $N = 0$  Landau level. Figure 53 (following page 65) graphically illustrates these level crossings.

By studying the photoconductive spectra of n-GaAs around 1.45 and 1.85 Tesla, any coupling between the  $2p_0$  and  $3d_{-2}$  or  $2p_{+1}$  and  $3s$  states might manifest itself as a variation in the photoconductive intensity of the observed transitions, or if the coupling is large enough become manifest as a splitting of the transition energy. This would experimentally verify the predicted transition energies, some of which could otherwise not be observed due to selection rules governing such transitions.

Method

As stated previously, all absolute intensity information is lost using the above experimental arrangement. The method chosen to allow comparison between photoconductive intensities involves using the  $1s \rightarrow 2p_{-1}$  transition. As figure 53 shows, the  $1s \rightarrow 2p_{-1}$  transition energy remains fairly constant over the 1 to 4 Tesla region, so its intensity should be unaffected by any beamsplitter or window material absorptions. In addition, the  $1s \rightarrow 2p_{-1}$  transition is not crossed by any other transitions and so should exhibit no level crossing intensity changes.

By using the  $1s \rightarrow 2p_{-1}$  intensity to ratio the  $1s \rightarrow 2p_0$  and  $2p_{+1}$  transition intensities, a direct comparison of the photoconductive intensity between spectra taken at different magnetic fields is possible.

All of the spectra were taken at a drive speed of 100 and a sampling interval of 32  $\mu\text{m}$  with over 2048 points taken or at

## CHAPTER 8

a drive speed of 50 and a sampling interval of  $16 \mu\text{m}$  with over 4096 points taken. This gives a spectral resolution of  $0.08 \text{ cm}^{-1}$  (Appendix B).

### Results

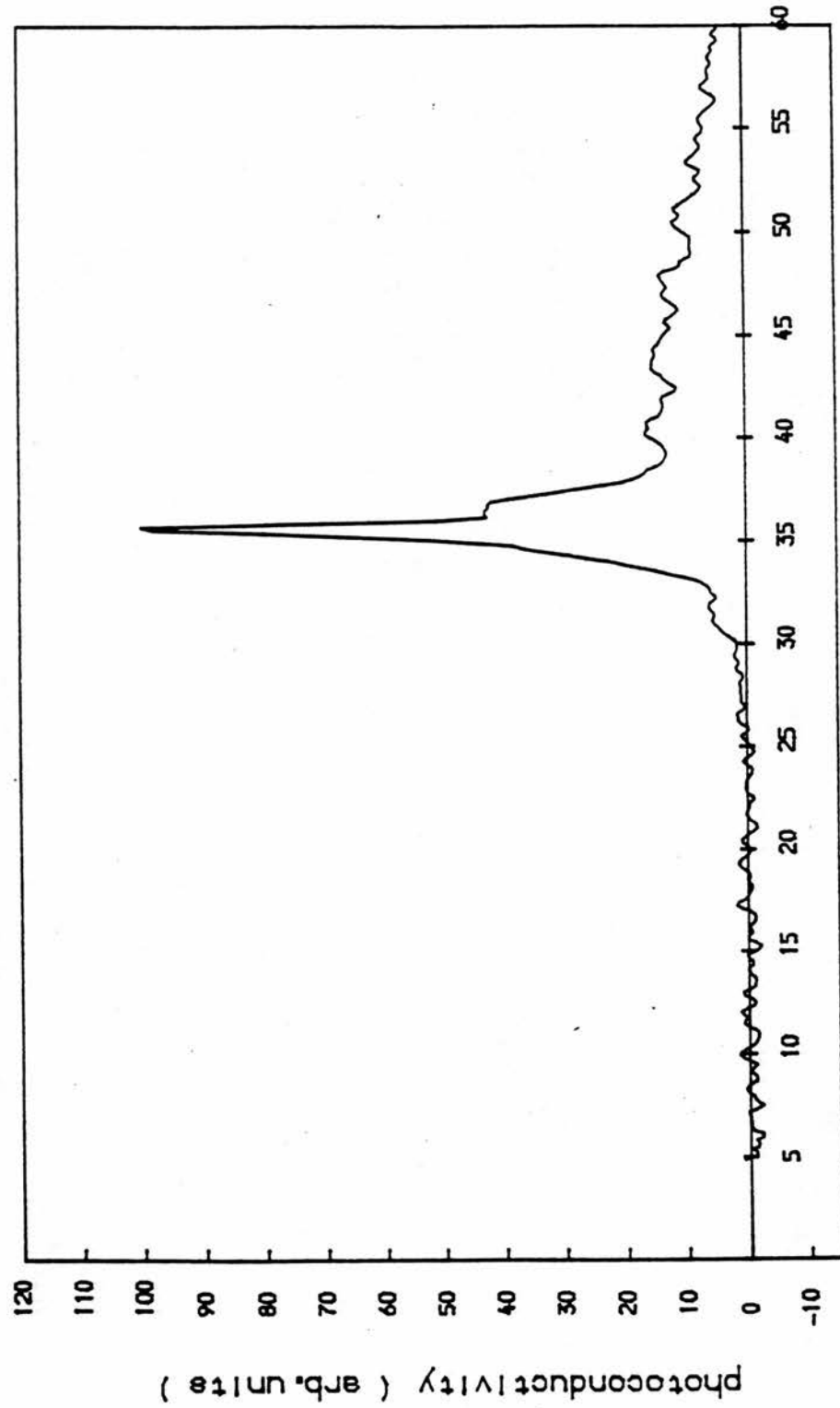
All the sample data relevant to the three samples used in the following experiments is presented in appendix D.

Sample R-137 of n-GaAs was analysed, first at zero Tesla. This would show any interference fringe effects, caused by a parallel sided sample acting as a Fabry-Pérot cavity (Figure 65 shows the zero field spectra of R-137 and some interference fringe effects are visible). The sample was then analysed at magnetic field strengths from 1.0 to 1.6 Tesla in 0.1 Tesla steps, arranged in a predominately Voigt orientation, i.e. the sample electric field perpendicular to the magnetic field. A typical spectrum is shown in Figure 66 whilst the ratioed results are shown in figures 67 a) and 68.

The Fourier transform spectrometer outputs a continuous interferogram; this is sampled discretely, and the spectra formed by the digital Fourier transform of the sampled interferogram is itself discrete. If a photoconductive intensity peak, corresponding to a transition energy, occurs between two points, the peak height will be poorly approximated. Figure 69 a) shows the  $1s \rightarrow 2p_{+1}$  transition in n-GaAs at 1.6 Tesla where the peak lies in-between two sampling points. Figure 69 b) shows the same transition in the same sample but at 1.5 Tesla: here the peak has been sampled at its maximum.

The apparent variation in peak height caused by sampling introduces large errors (over 2.5%) into the ratio based comparison technique. To overcome this problem a parabola was fitted to the maximum three points on every peak and the maximum value of this used as the peak height. This was a

FIGURE 65  
RUN 402 R137 n-GaAs 0 tesla 4.2 K 100 G B/S



frequency ( cm-1 )

FIGURE 66

RUN540 n-GaAs R-137 1.3Tesla 4.2K

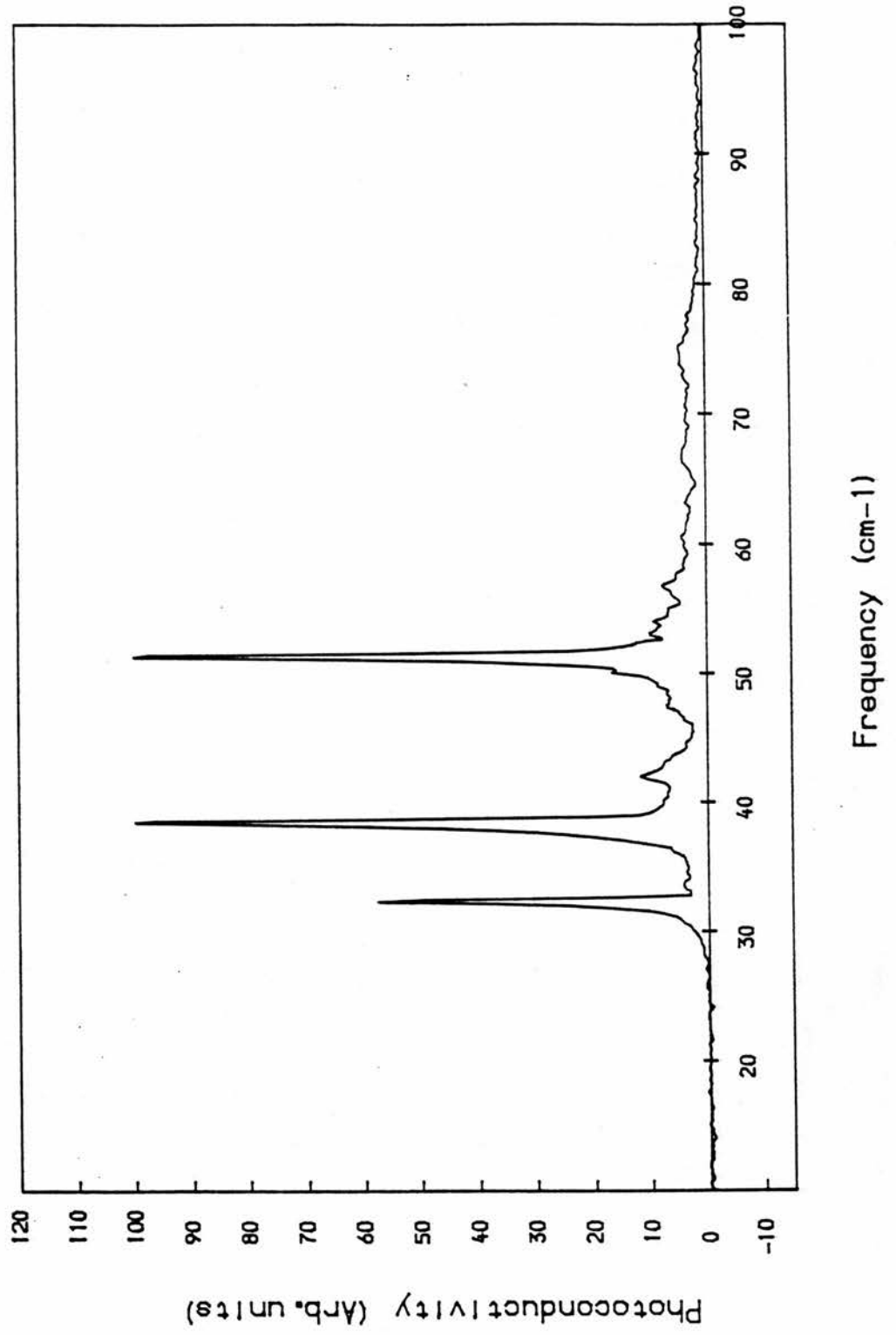






FIGURE 69 a

RUN566 n-GaAs R-137 1.6 Tesla 4.2K

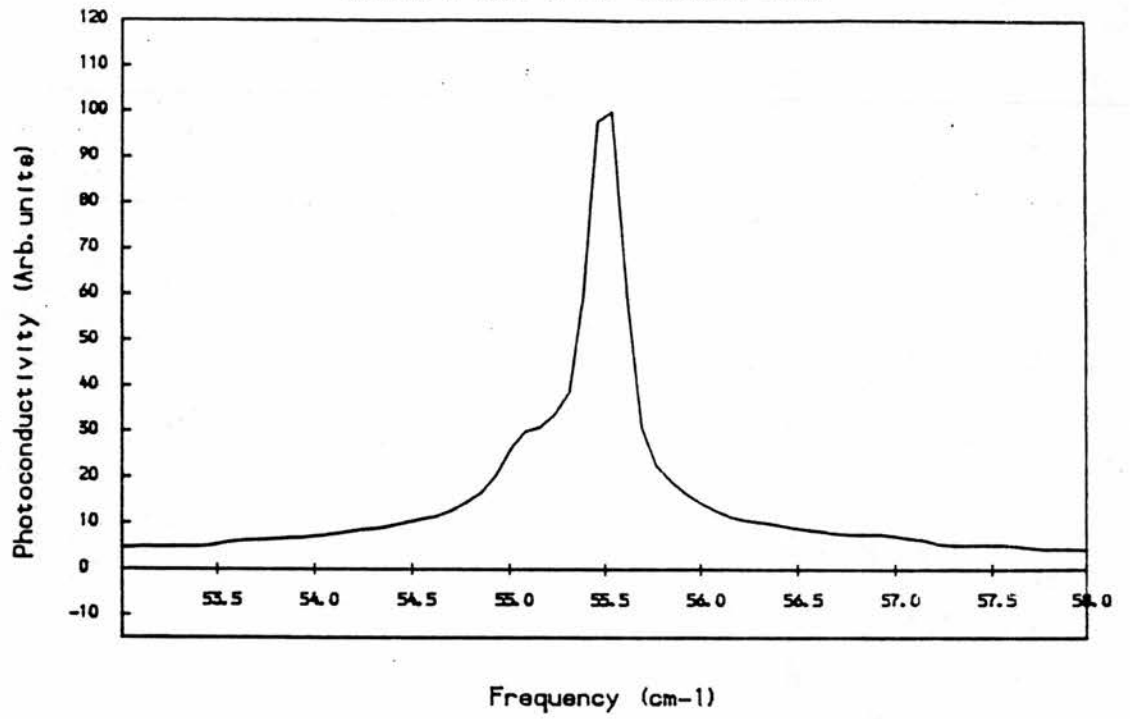
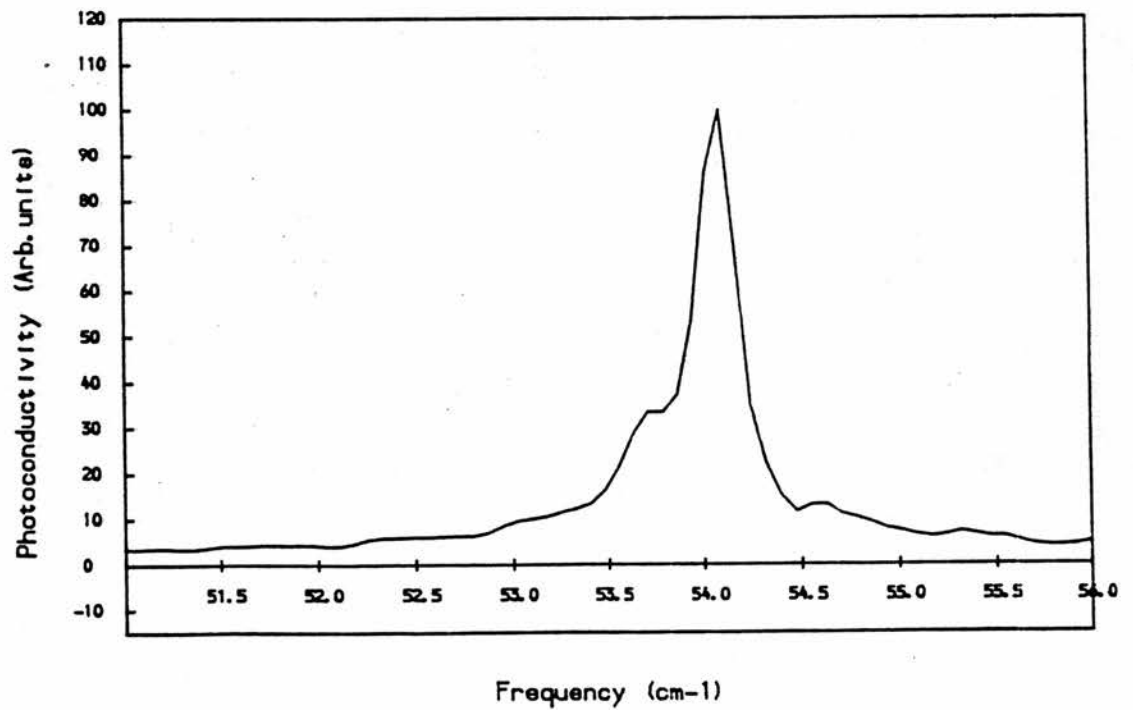


FIGURE 69 b

RUN565 n-GaAs R-137 1.5 Tesla 4.2K



## CHAPTER 8

relatively simple operation because the sampled points are evenly spaced. All the results presented were treated this way including those previously mentioned.

A further set of results from 1.3 Tesla to 2.0 Tesla in 0.1 Tesla steps were then taken. In this experiment the sample was in a predominantly Faraday orientation (sample electric field parallel to the magnetic field). In this orientation the  $1s \rightarrow 2p_0$  transition is forbidden, but sample mis-alignment and the integrating cavity breaks this restriction. Figure 70 shows a typical spectra, with the much reduced  $1s \rightarrow 2p_0$  transition intensity as compared to figure 66. Figures 67 b) and 68 show the ratioed results.

These results show a possible dip in the  $1s \rightarrow 2p_0$  transition around 1.45 Tesla and dips in the  $1s \rightarrow 2p_{+1}$  transition around 1.45 and 1.85 Tesla. To investigate these further, a series of spectra were taken in 0.01 Tesla steps from 1.41 to 1.49 Tesla and 1.81 to 1.89 Tesla, this time with the sample in the Faraday orientation.

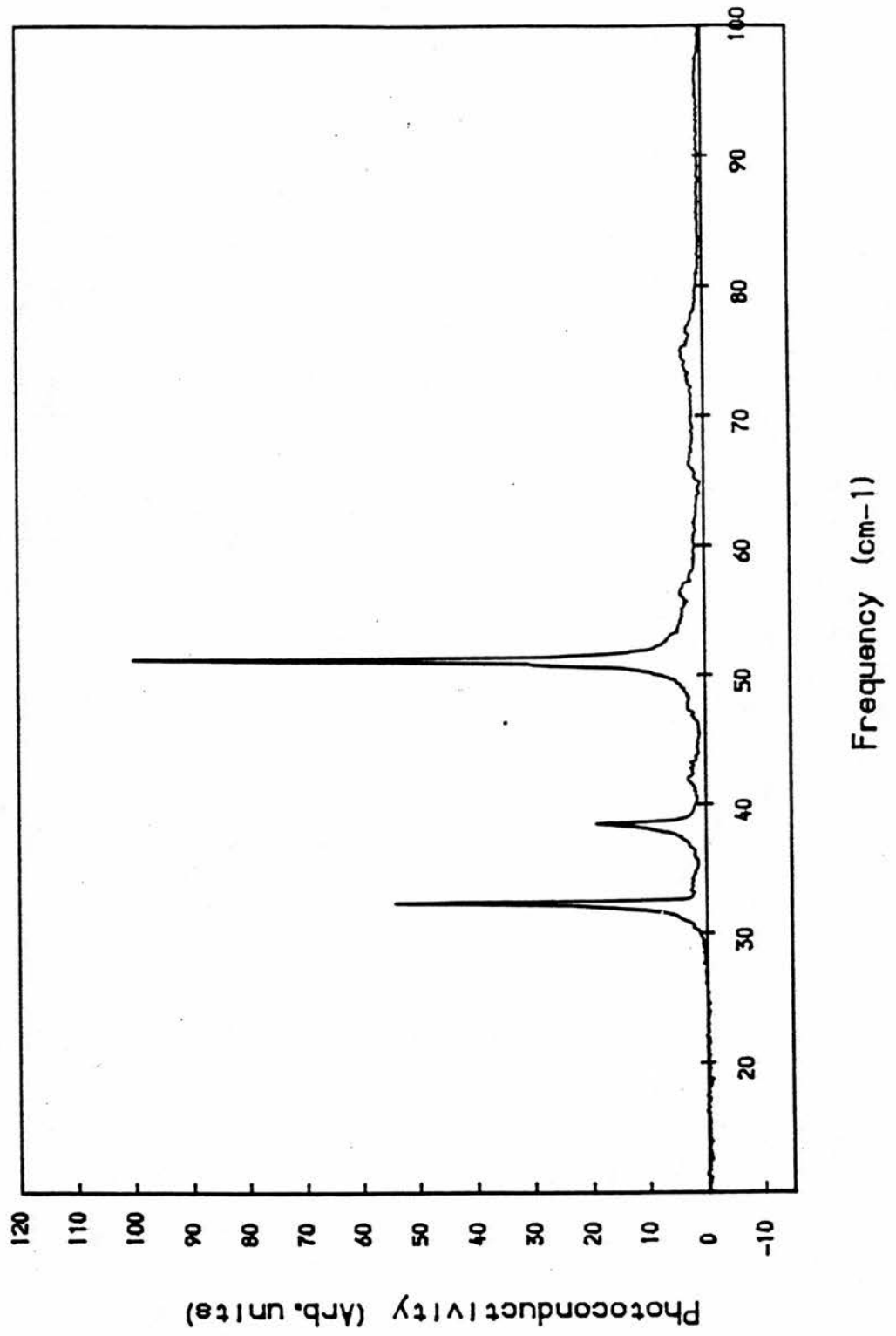
The  $1s \rightarrow 2p_0$  transition results around 1.45 and 1.85 Tesla and the  $1s \rightarrow 2p_{+1}$  transition around 1.85 Tesla are relatively flat and the absolute values lie close to the previous results at 1.4 and 1.8 Tesla.

The  $1s \rightarrow 2p_{+1}$  transition results around 1.45 Tesla do show indications of a rise and this fits the 1.4 and 1.5 Tesla points presented in figure 68.

The above sample, R-137, has only one dominant donor and so shows only one set of transitions. If another sample with two or more shallow donors of roughly equal concentration could be found, then the discrete peaks, seen above, would be split by the central cell effects. Since the central cell effects predominantly perturb the ground state, none of the excited states are significantly split or perturbed by chemical shifts. Therefore any change in photoconductive

FIGURE 70

RUN563 n-GaAs R-137 1.3Tesla 4.2K



## CHAPTER 8

intensity caused by level crossings should affect each of the split peaks at the same magnetic field and comparison of the results should allow the removal of any sharp structure in the background (Figure 59).

Sample RR98B of n-GaAs had suitable central cell structure. Figure 71 shows a spectra taken at 2.0 Tesla. Each transition is split into three peaks corresponding to three donors. Spectra were taken from 1.0 to 2.0 Tesla in 0.1 Tesla steps. The  $1s \rightarrow 2p_0$  transition results show rises of about 50% from 1.0 to 1.5 Tesla, then no further change. Only the two largest central cell peaks were used as the highest energy peak is too close to the background noise to be of use for ratio calculations. The results for each donor are equivalent. The  $1s \rightarrow 2p_{+1}$  transition oscillates by 20% over the magnetic field range of 1.0 to 2.0 Tesla.

No definitive drop in photoconductive intensity occurs around 1.45 or 1.85 Tesla for either of the transitions. Looking at the zero field spectra of sample RR98B, figure 72, shows periodic oscillations of up to 50% which are characteristic of interference fringes caused by a parallel sided sample. As the magnetic field increases causing the  $1s \rightarrow 2p_0$  and  $2p_{+1}$  transitions to move up in energy and so frequency, the interference effects will periodically vary the photoconductive intensities. This is the cause of the transition intensity variations seen in sample RR98B.

Another sample with multiple donors was then tried. The Stillman No. 1 sample has the same three contributing donors as RR98B and figure 73 shows a typical spectra at 2.0 Tesla. Only the two most intense peaks are ratioed. Spectra were again taken from 1.0 to 2.0 Tesla in 0.1 Tesla steps with the sample in the Faraday orientation. No obvious minima were observed in the ratioed results. The  $1s \rightarrow 2p_0$  transition intensity shows a 25% increase over the 1.0 to 2.0 Tesla range

FIGURE 71

RUN844 n-GaAs RR98B 2.0 Tesla

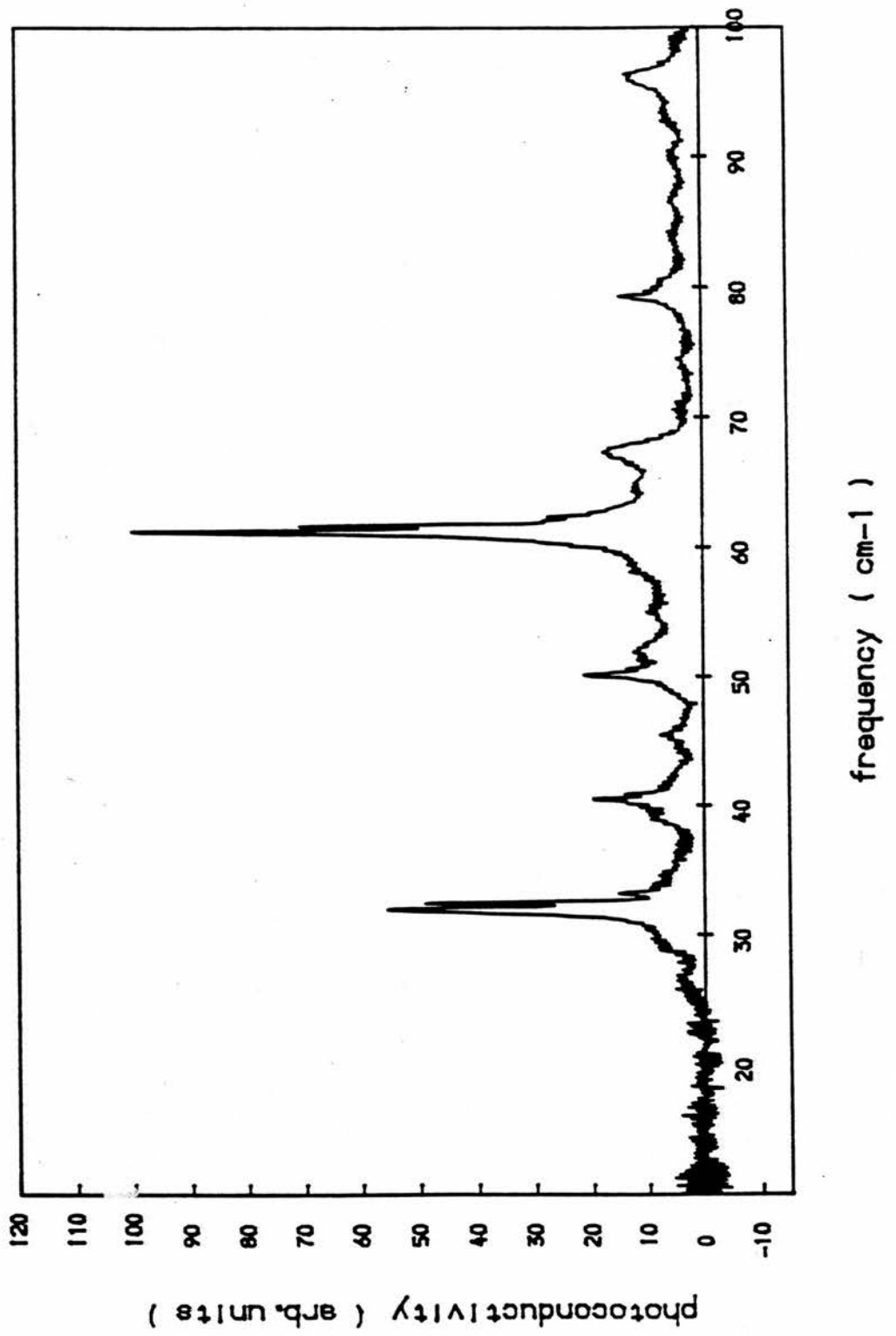
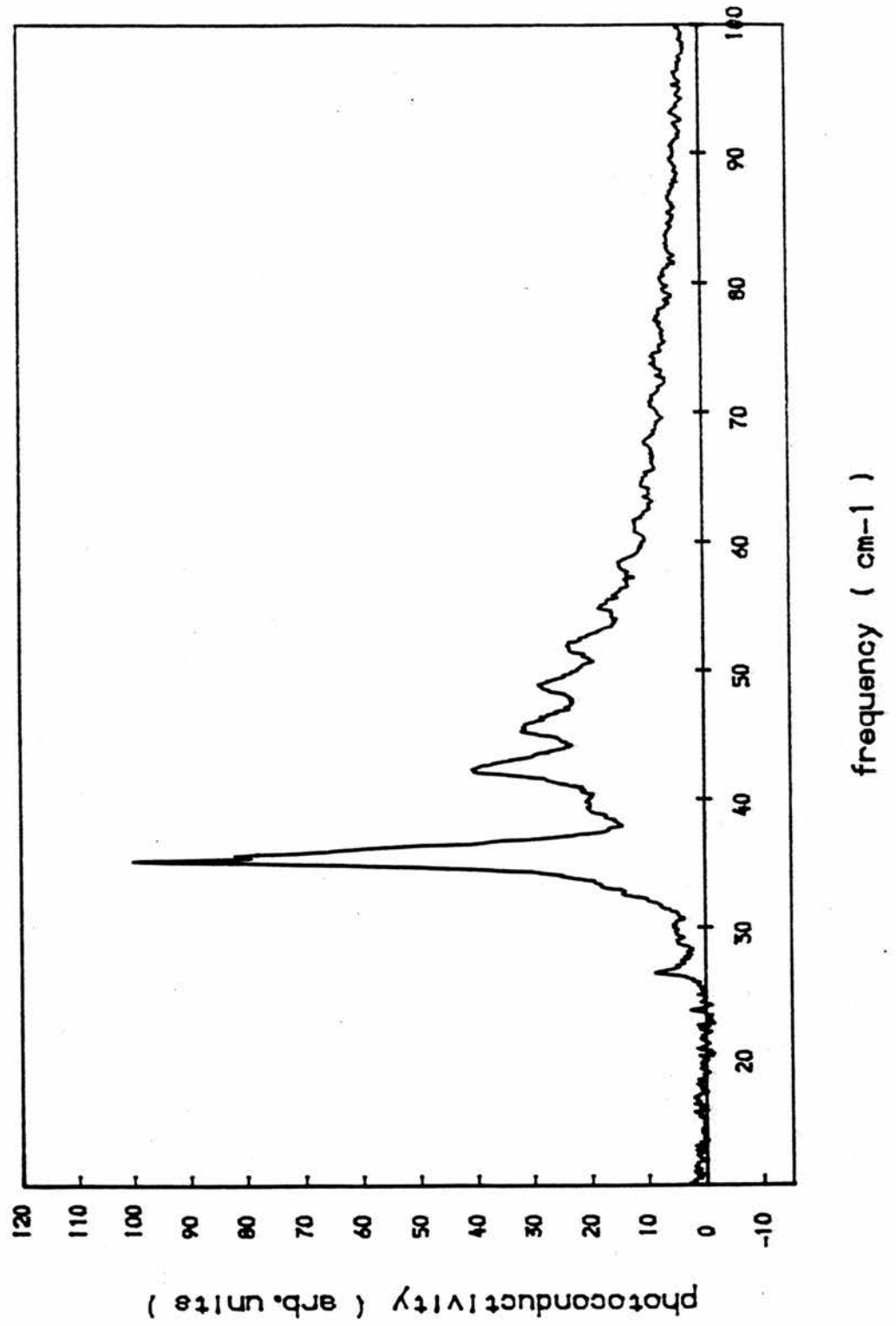
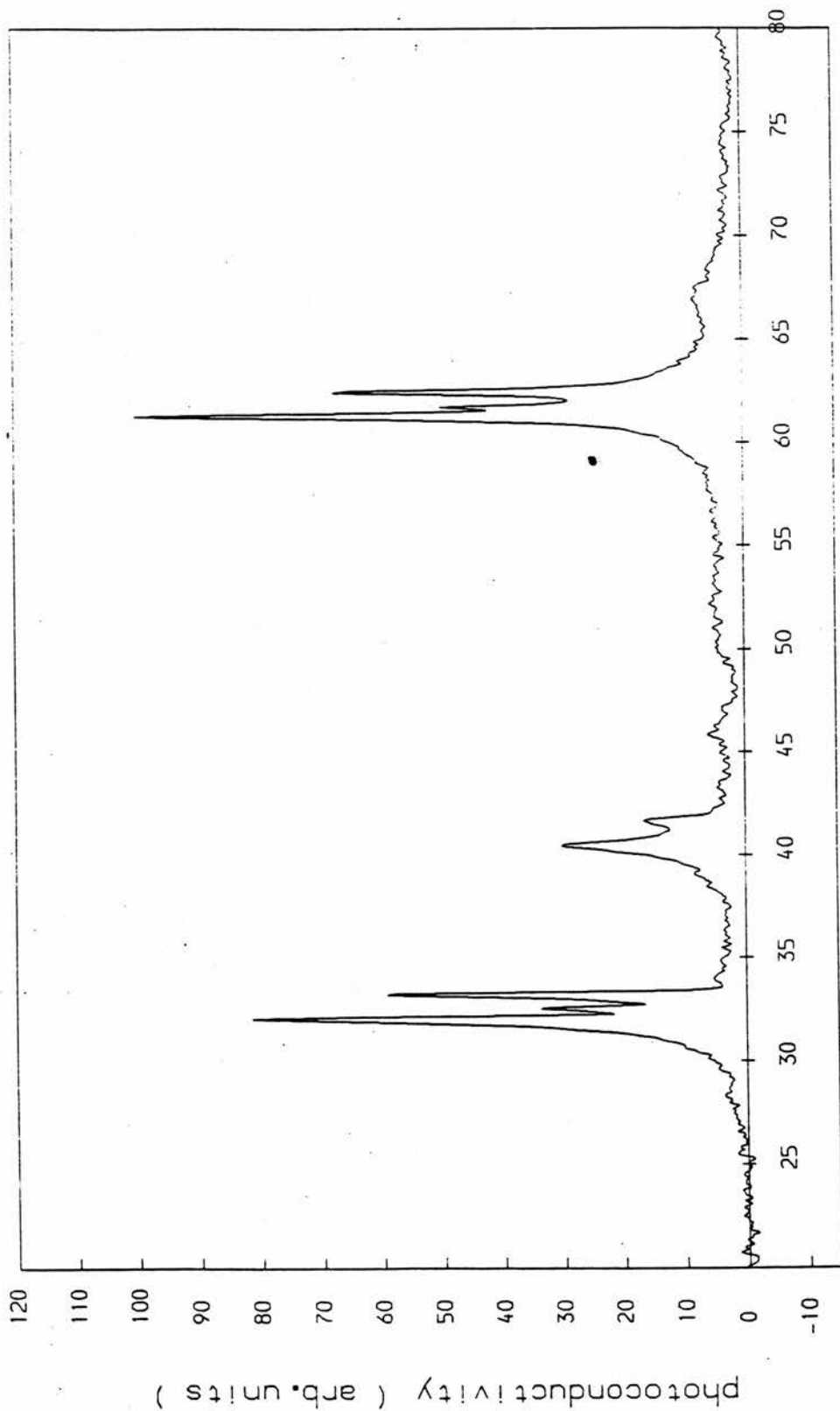


FIGURE 72

RUN846 n-GaAs RR98B 0.0 Tesla



**FIGURE 73**  
run1044 Photocon. n-GaAs Stillman wedged 2.0 T 4.2 K 100G b/s



frequency ( cm-1 )

whilst the  $1s \rightarrow 2p_{+1}$  transition intensity has a 50% reduction with small oscillations (about 5%) over the same range.

The sample was finally analysed in the Voigt orientation at the same magnetic fields and these results reproduce the Faraday orientation results but with the reduced  $1s \rightarrow 2p_0$  transition intensity.

### Discussion

Several possible reasons exist for the variation in photoconductive intensity of the  $1s \rightarrow 2p_0$  and  $1s \rightarrow 2p_{+1}$  transitions other than level crossing effects. As seen in the results already, interference fringes caused by the samples parallel sides leads to frequency dependent absorption and this explains the oscillatory variations.

Any source, beamsplitter or window absorptions together with any absorptions of the remaining atmosphere in the spectrometer, would lead to reduced illumination intensity at the absorption wavelengths. As the magnetic field is increased, the energy of the ground to excited state transitions increases, the associated frequency passes through these absorptions and thus their photoconductive intensities are diminished.

To determine the system response a spectrum was taken with the same arrangement as used for the level crossing experiments but using a bolometer as the detecting element. The bolometer consisted of an Alan-Bradley carbon resistor polished to leave a thin slice of carbon connected at both ends. Variations in temperature caused by the incident radiation, resulted in resistivity variations which were detected in the same way as for the photoconductivity experiments.

The spectrum obtained (figure 74), shows that the spectrometer background does have fine structure (run

## CHAPTER 8

resolution  $0.08 \text{ cm}^{-1}$ ). This structure in the region of interest,  $35 \text{ cm}^{-1} \rightarrow 63 \text{ cm}^{-1}$ , can vary from a smooth sine function of the perfect beamsplitter by up to 20%.

Taking into account the variation of light intensity falling on the samples as a result of the system absorptions (figure 74), together with the oscillatory absorption caused by the sample acting as a Fabry-Pérot cavity the experimental results show only one unusual feature which could be taken as being caused by level crossing effects. This is shown in figure 68 where the results for runs 533-540 show a much larger drop at 1.6 Tesla for the  $1s \rightarrow 2p_{+1}$  transition than can be explained by the above effects. This result was not verified by runs 563 to 570 (figure 68) using the same sample, nor did any of the other samples show a large fall in the  $1s \rightarrow 2p_{+1}$  transition intensity at 1.6 Tesla and this suggests that it is an experimental error.

### Conclusions

All the evidence indicates that within the experimental accuracy no interactions between the excited donor states occurs in GaAs for low level, far-infrared illumination. Any structure in the transition energy photoconductive intensity vs. magnetic field was due to beamsplitter transmission variations and interference from multiple internal reflections.

The experimental accuracy is difficult to estimate because of the large variation in background and sample shape related effects (up to 50%). Also the difference between the maximum sampled peak height and the parabolically fitted height, was up to 2.5%. The only feature which stood out (but was not reproducible) was around 10% greater than any explainable variations. Thus any level crossing effects would

## CHAPTER 8

have to be less than 10% of the transition intensity to remain unnoticed.

Any future work into level crossings will have to find a way to remove the effect of equipment absorptions, possibly by using a reference detector such as an Alan-Bradley carbon resistor alongside the sample under test to monitor the incident radiation level in real time. As well as using wedged samples to remove interference fringe effects.

## REFERENCES

### References

#### CHAPTER 1

- [1] W.G.Spitzer and H.Y.Fan, Physical Review, Vol.106, N° 5, p882, Jun.1957
- [2] David F.Edwards and Paul D.Maker, J.Appl.Phys. Vol. 33, N° 8, p2466, Aug.1962
- [3] L.E.Howarth and J.F.Gilbert, S.S.Comm. p236, 1962
- [4] L.A.Murray, J.J.Rivera and P.A.Hoss, J.Appl.Phys. Vol.37 N° 13, p4743, Dec.1966
- [5] E.E.Gardener, W.Kappallo and C.R.Gordon, App.Phys.Lett., Vol.9, N° 12, p432, Dec.1966
- [6] V.K.Subashiev and A.A.Kukharskii, Phys.Stat.Sol. Vol. 23, p447, (1967)
- [7] P.A.Schuman, Jr. Solid State Tech. p50, Jan.1970
- [8] E.D.Palik, R.T.Holm and J.W.Gibson, Thin Solid Films, Vol. 47(1977), p167
- [9] Hans H.Wagner and Rolf R.Schaefer, J.Appl.Phys. Vol. 50 N° 4, p2697, Apr.1979
- [10] E.D.Palik and R.T.Holm, Chapter 6 "Non Destructive Evaluation of Semiconductor Materials and Devices", NATO Advanced Study Institute Series. Vol.B46, (Plenum 1979)
- [11] Herbert Engstrom, J.Appl.Phys. Vol. 51 N° 10, p5245, Oct.1980
- [12] Hans H.Wagner, Rolf R.Schaefer and Juergen E.Kempf, J.Appl.Phys. Vol.52 N° 10, p6173, Oct.1981
- [13] C.Pickering, R.S.R.E.Malvern, Non-destructive characterisation of n-type InP epitaxial layers by infrared reflectivity measurements.
- [14] Marek Pawlik, Laser and Electron Beam Interactions with Solids. p293,1982
- [15] E.Barta and G.Lux, J.Phys.D: Applied Physics 16. p1543, 1983
- [16] Y.Demakopoulou, D.Siapkas, N.N.Zheleva and D.B.Kushev, Infrared Physics, Vol.26, N° 2, pp105-109, 1986

## REFERENCES

- [17] D.B.Kushev, N.N.Zheleva, Y.Demakopoulou and D.Siapkas  
Infrared Physics, Vol.26, N° 6, pp385-393, 1986
- [18] S.U.Campisano, E.Rimini, A.Borghesi, G.Guizzetti,  
L.Nosenzo and A.Stella, Physica Scripta, Vol.T19.  
pp544-547.1987
- [19] H.Ryssel and I.Ruge, Ion Implantation, Wiley
- [20] F.A.Trumbore, Bell System Technical Journal, Jan. 1960,  
p205
- [21] J.W.Maver, L.Eriksson and J.A.Davis. Ion Implantation in  
semiconductors - Silicon and Germanium, Academic Press  
1970

## CHAPTER 2

- [22] H.A.Macleod, Thin Film Optical Filters
- [23] J.W.Allen, Post-graduate lectures on Optical Properties  
of Solids, St.Andrews Physical Sciences Dept. 1982
- [24] I.S.Grant and W.R.Phillips, Electromagnetism
- [25] H.I.Ralph, G.Simpson and R.J.Elliot, Phys.Rev.B, Vol.11,  
N° 8, p2948, Apr.1974
- [26] R.A.Stradling and V.V.Zhukov, Proceedings of the Physical  
Society, Vol.87, pp263-271, 1966.

## CHAPTER 3

- [27] Runge, Phosphorous ranges in Silicon, Landholt-Börnstein,  
Vol. 17 part C.

## REFERENCES

### CHAPTER 7

- [28] Madelung, Physics of III-V Compounds, p35
- [29] W.Kohn, J.M.Luttinger, Phys.Rev. 98,915 (1955)
- [30] C.Aldrich, R.J.Greene, Phys.stats.sol (b), 93, 343 (1979)
- [31] R.J.Elliott, A.F.Gibson, An introduction to Solid State Physics and its Applications, MacMillian Press, 118 (1976)
- [32] C.Kittel, Introduction to Solid State Physics 5th Edition John Wiley & Sons, Inc.
- [33] A.Haug, Theoretical and Solid State Physics, Vol.2
- [34] R.M.Eisberg, Fundamentals of Modern Physics, John Wiley & Sons, Inc.
- [35] G.W.Chantry, H.M.Evans, J.W.Fleming and H.A.Gebbie, Infrared Physics, Vol.9, pp31-33, 1969

APPENDIX A

10000 '   
10010 ' APPENDIX A   
10020 '   
10030 '   
10040 ' This programme is written in Basic and covers the   
10050 ' calculation of Reflectivity, Transmission and   
10060 ' Absorption of an ion-implanted silicon wafer. See   
10065 ' chapters two and three for the theory.   
10070 '   
10080 ' The programme is not written to allow the radiation   
10090 ' angle of incidence to be changed. This saves time in   
10100 ' the calculations and if it is required the relevant   
10105 ' theory in chapter two covers this.   
10110 '   
10120 ' The first part of the programme sets up the initial   
10130 ' values and is followed by three menus which allow the   
10135 ' values to be changed.   
10140 '   
10150 DIM np(20),reflect(100),transmit(100),absorb(100)   
10160 '   
10170 ' Constants set-up   
10180 '   
10190 ' Cutoff concentration, electrons / m<sup>3</sup>   
10200 nc = 1.4E+26   
10210 '   
10220 ' Implant dose, ions / m<sup>2</sup>   
10230 ic = 5E+19   
10240 '   
10250 ' Background concentration, electrons / m<sup>3</sup>   
10260 bc = 1E+20   
10270 '   
10280 ' Maximum implant depth, meters   
10290 depth = 0.0000003   
10300 '   
10310 ' Wafer thickness, meters   
10320 thick = 0.000365

APPENDIX A

10330 '
   
10340 ' Radiation incident angle, degrees, 0 ⇒ normal to wafer
   
10350     angle = 0
   
10360 '
   
10370 ' Number of layers
   
10380     nolay = 10
   
10390 '
   
10400 ' Mean position
   
10410     x = 3
   
10420     mean = depth / x
   
10430 '
   
10440 ' Standard deviation
   
10450     y = 2
   
10460     sigma = depth / y
   
10470 '
   
10480 ' Number of points
   
10490     res = 50
   
10500 '
   
10510 ' Scattering time, seconds, 0 ⇒ use equations 45 & 46.
   
10520     scatt = 0
   
10530 '
   
10540 ' Gaussian constants
   
10550     bq1 = 0.31938153
   
10560     bq2 = -0.356563782
   
10570     bq3 = 1.781477937
   
10580     bq4 = -1.821255978
   
10590     bq5 = 1.330274429
   
10600 '
   
10610 ' Minimum wavelength, meters
   
10620     wmin = 0.000001
   
10630 '
   
10640 ' Maximum wavelength, meters
   
10650     wmax = 0.00001
   
10660 '
   
10670 ' wave\$ =Yes implies linear in wavelength, = No implies
   
       linear in frequency

APPENDIX A

```

10680     wave$ = "Yes" : freq$ = " No"
10690 '
10700 ' rear$ = No implies no interference fringes. = Yes
        implies interference fringes.
10710 '   rear$ = " No"
10720 '
10730 PRINT "
10740 PRINT "           Menu One"
10750 PRINT ""
10760 PRINT "0 Start calculation"
10770 PRINT "1 Implant dose (ions / m2)           ";ic
10780 PRINT "2 Background dose (electrons / m3) ";bc
10790 PRINT "3 Cutoff concentration (ions / m3) ";nc
10800 PRINT "4 Implant depth (meters)           ";depth
10810 PRINT "5 Incident Angle (degrees)           ";angle
10820 PRINT "6 Waer thickness (meters)           ";thick
10830 PRINT "7 Menu 2"
10840 PRINT "8 Menu 3"
10850 PRINT "9 End"
10860 PRINT ""
10870 PRINT "Input your choice 0 to 9"
10880 INPUT choice
10890 IF choice < 0 OR choice > 9 THEN GOTO 10730
10900 IF choice = 0 THEN GOTO 11710
10910 IF choice = 1 THEN PRINT "Input new implant dose
        ions / m2" : INPUT ic
10920 IF choice = 2 THEN PRINT "Input new background dose
        electrons / m3" : INPUT bc
10930 IF choice = 3 THEN PRINT "Input new cutoff concentration
        electrons / m3" : INPUT nc
10940 IF choice = 4 THEN PRINT "Input new depth meters" :
        INPUT depth : mean = depth/x : sigma = depth/y
10950 IF choice = 5 THEN PRINT "This option not available."
10960 IF choice = 6 THEN PRINT "Input new wafer thickness
        meters." : INPUT thick
10970 IF choice = 7 THEN GOTO 11030

```

APPENDIX A

```

10980 IF choice = 8 THEN GOTO 11330
10990 IF choice = 9 THEN END
11000 GOTO 10730
11010 '
11020 '
11030 PRINT ""
11040 PRINT "          Menu Two"
11050 PRINT ""
11060 PRINT "0 Start calculation"
11070 PRINT "1 Number of layers           ";nolay
11080 PRINT "2 Number of points (resolution)   ";res
11090 PRINT "3 Mean of implant (x = depth/mean)  ";x
11100 PRINT "4 Deviation of implant (y = depth/devi) ";y
11110 PRINT "5 Scattering time (secs 0 ⇒ use formula) ";scatt
11120 PRINT "6 Not used"
11130 PRINT "7 Menu 1"
11140 PRINT "8 Menu 2"
11150 PRINT "9 End"
11160 PRINT ""
11170 PRINT "Input your selection 0 to 9"
11180 INPUT choice
11190 IF choice < 0 OR choice > 9 THEN GOTO 11030
11200 IF choice = 0 THEN GOTO 11710
11210 IF choice = 1 THEN PRINT "Input new number of layers" :
      INPUT nolay
11220 IF choice = 2 THEN PRINT "Input new number of points" :
      INPUT res
11230 IF choice = 3 THEN PRINT "Input new x with mean =
      depth/x" : INPUT x : mean = depth/x
11240 IF choice = 4 THEN PRINT "Input new y with deviation =
      depth/y" : INPUT y : sigma = depth/y
11250 IF choice = 5 THEN PRINT "Input new scattering time in
      seconds. 0 implies use formula." : INPUT scatt
11260 IF choice = 6 THEN PRINT "This option not used."
11270 IF choice = 7 THEN GOTO 10730
11280 IF choice = 8 THEN GOTO 11330

```

APPENDIX A

```

11290 IF choice = 9 THEN END
11300 GOTO 11030
11310 '
11320 '
11330 PRINT ""
11340 PRINT "          Menu Three"
11350 PRINT ""
11360 PRINT "0 Start calculation"
11370 PRINT "1 Minimum wavelength (meters) ";wmin,"cm-1 ";
                                0.01/wmin
11380 PRINT "2 Maximum wavelength (meters) ";wmax,"cm-1 ";
                                0.01/wmax
11390 PRINT "3 Linear wavelength scale ";wave$
11400 PRINT "4 Linear frequency scale ";freq$
11410 PRINT "5 Rear surface ";rear$
11420 PRINT "6 Not used"
11430 PRINT "7 Menu 1"
11440 PRINT "8 Menu 2"
11450 PRINT "9 End"
11460 PRINT ""
11470 PRINT "Input your selection 0 to 9"
11480 INPUT choice
11490 IF choice < 0 OR choice > 9 THEN GOTO 11330
11500 IF choice = 0 THEN GOTO 11710
11510 IF choice = 1 THEN PRINT "Input new minimum wavelength
in meters" : INPUT wmin
11520 IF choice = 2 THEN PRINT "Input new maximum wavelength
in meters" : INPUT wmax
11530 IF choice = 3 THEN wave$ = "Yes" : freq$ = " No"
11540 IF choice = 4 THEN wave$ = " No" : freq$ = "Yes"
11550 IF choice = 5 AND rear$ = "Yes" THEN rear$ = " No" :
GOTO 11330
11560 IF choice = 5 AND rear$ = " No" THEN rear$ = "Yes"
11570 IF choice = 6 THEN PRINT "This option not used."
11580 IF choice = 7 THEN GOTO 10730
11590 IF choice = 8 THEN GOTO 11030

```

APPENDIX A

```

11600 IF choice = 9 THEN END
11610 GOTO 11330
11620 '
11630 ' This next DO loop calculates the electron concentra-
11640 ' tion for each layer. Assuming a Gaussian distribution
11650 ' of ions with depth, where the mean and standard
11660 ' deviation are given in the second menu, allows the
11670 ' number of ions for each layer to be found. The number
11680 ' of ions, assuming 100% activation, is equal to the
11690 ' number of electrons, dividing by the layer thickness
11695 ' gives the electron density.
11700 '
11710 PRINT "Layer", "LOG(electron conc.)"
11720 '
11730 FOR i = 1 TO nlay
11740 x1 = depth * (i-1) / nlay
11750 x2 = depth * i / nlay
11755 '
11760 GOSUB 13910 : ' Gaussian
11765 '
11770 np(i) = n
11780 PRINT i, LOG10(np(i)/1000000)
11790 NEXT
11800 '
11810 ' The next section initialises the Q matrix which is 2x2
11820 ' and complex.
11825 '
11830 '      |1+0i 0+0i| |qr(1,1)+qi(1,1) qr(2,1)+qi(2,1)|
11840 '  Q = |          | = |
11850 '      |0+0i 1+0i| |qr(1,2)+qi(1,2) qr(2,2)+qi(2,2)|
11860 '
11870 ' The Q matrix is used to store the products of the
11880 ' characteristic matrices of each layer as these are
11885 ' built up.
11890 '
11900 ' The DO loop is the start of the calculation proper, it

```

## APPENDIX A

```

11910 ' steps through each wavelength calculating the step
11920 ' size to give linear plots in wavelength or frequency.
11930 ' For each wavelength the characteristic matrix of the
11935 ' assembly of layers is found and from that the optical
11940 ' properties of the implanted wafer at one wavelength
11945 ' evaluated.
11950 '
11960 ' The PRINT statement places titles over the columns
11970 ' which will display the calculation results for each
11975 ' wavelength.
11980 ' Finally line 12150 converts from wavelength to
11985 ' frequency.
11990 '
12000 PRINT ""
12010 PRINT "Point","      Lambda"," cm-1","      R","      T",
        "      A"
12020 '
12030 FOR i = 0 TO res
12040 '
12050 IF wave$ = "Yes" THEN wav = wmin + (wmax-wmin) / res*i
        ELSE wav = 1 / (1/wmax + (1/wmin - 1/wmax) / res*i)
12060 qr(1,1) = 1
12070 qr(1,2) = 0
12080 qr(2,1) = 0
12090 qr(2,2) = 1
12100 qi(1,1) = 0
12110 qi(1,2) = 0
12120 qi(2,1) = 0
12130 qi(2,2) = 0
12140 '
12150 w = 1.885E+09 / wav
12160 '
12170 ' From here another nested DO loop takes the electron
12175 ' concentration for each layer and uses the nk
12180 ' subroutine to find the complex refractive index for
12190 ' that layer  $N = n - ik$ . From this the elements of the

```

APPENDIX A

```

12200 ' characteristic matrix for the layer, M, can be found:-
12210 '
12220 '      |      cos(delta)      i.sin(delta)/neta |
12230 ' M = |
12240 '      | i.sin(delta).neta      cos(delta)      |
12250 '
12260 ' delta = 2.pi.N.d.cos(theta) / wavelength
12270 '      d = layer thickness
12280 '      neta = N.cos(theta) s-waves
12290 '           = N/cos(theta) p-waves
12300 ' theta from Snell's law
12310 '
12320 ' Since this programme is written for constant theta = 0
12330 ' degrees cos(0) = 1 and neta = N the complex refractive
12340 ' index = n - ik.
12350 '
12360 ' The product of all the M's at one wavelength give P.
12370 '
12380 FOR l = 1 TO nolay
12390   ntemp = np(l)
12400 '
12410   GOSUB 14170           : ' Complex Refractive Index n - ik
12420 '
12430   deltar = 6.283 * nr * depth / nolay / wav
12440   deltai = 6.283 * ni * depth / nolay / wav
12450   netar = nr
12460   netai = ni
12470   a = deltar
12480   b = deltai
12490 '
12500   GOSUB 14330           : ' Complex Cosine
12510 '
12520   mr(1,1) = a
12530   mr(2,2) = a
12540   mi(1,1) = b
12550   mi(2,2) = b

```

APPENDIX A

```

12560 a = deltar
12570 b = deltai
12580 '
12590 GOSUB 14520 : ' Complex Sine
12600 '
12610 g = -b
12620 h = a
12630 c = netar
12640 d = netai
12650 a = g
12660 b = h
12670 '
12680 GOSUB 14720 : ' Complex Multiply
12690 '
12700 mr(1,2) = e
12710 mi(1,2) = f
12720 '
12730 GOSUB 14800 : ' Complex Divide
12740 '
12750 mr(2,1) = e
12760 mi(2,1) = f
12765 '
12770 pr(1,1) = qr(1,1)*mr(1,1) - qi(1,1)*mi(1,1) +
           qr(2,1)*mr(1,2) - qi(2,1)*mi(1,2)
12780 pi(1,1) = qr(1,1)*mi(1,1) + qi(1,1)*mr(1,1) +
           qr(2,1)*mi(1,2) + qi(2,1)*mr(1,2)
12790 pr(1,2) = qr(1,2)*mr(1,1) - qi(1,2)*mi(1,1) +
           qr(2,2)*mr(1,2) - qi(2,2)*mi(1,2)
12800 pi(1,2) = qr(1,2)*mi(1,1) + qi(1,2)*mr(1,1) +
           qr(2,2)*mi(1,2) + qi(2,2)*mr(1,2)
12810 pr(2,1) = qr(1,1)*mr(2,1) - qi(1,1)*mi(2,1) +
           qr(2,1)*mr(2,2) - qi(2,1)*mi(2,2)
12820 pi(2,1) = qr(1,1)*mi(2,1) + qi(1,1)*mr(2,1) +
           qr(2,1)*mi(2,2) + qi(2,1)*mr(2,2)
12830 pr(2,2) = qr(1,2)*mr(2,1) - qi(1,2)*mi(2,1) +
           qr(2,2)*mr(2,2) - qi(2,2)*mi(2,2)

```

## APPENDIX A

```

12840   pi(2,2) = qr(1,2)*mii(2,1) + qi(1,2)*mr(2,1) +
          qr(2,2)*mii(2,2) + qi(2,2)*mr(2,2)
12850   qr(1,1) = pr(1,1)
12860   qi(1,1) = pi(1,1)
12870   qr(1,2) = pr(1,2)
12880   qi(1,2) = pi(1,2)
12890   qr(2,1) = pr(2,1)
12900   qi(2,1) = pi(2,1)
12910   qr(2,2) = pr(2,2)
12920   qi(2,2) = pi(2,2)
12930   NEXT
12940   '
12950   ' Having calculated the characteristic matrix for the
12960   ' ion-implanted layer the next step is to include the
12970   ' effects of the substrate. The choice in menu 3 number
12980   ' 5 determines whether the substrate is treated as a
12990   ' final thick layer leading to interference fringes or
13000   ' as an infinite substrate. The second option acts to
13010   ' model a wafer at short wavelengths when the substrate
13015   ' is a source of diffuse incoherent backscatter.
13020   '
13030   ntemp = bc
13040   '
13050   GOSUB 14170           : ' Complex Refractive Index n - ik
13060   '
13070   netaor = nr
13080   netaoi = ni
13090   '
13100   ' Rear surface or not
13110   '
13120   IF rear$ = "Yes" THEN GOSUB 14980 : ' Rear Surface Calc
13130   '
13140   ' The P matrix is complete and the next step is to turn
13150   ' this into an effective refractive index for the layer
13160   ' at that wavelength and to calculate the reflectivity,
13170   ' transmission and absorption from that. This is

```

APPENDIX A

```

13175 ' performed as follows:-
13180 '
13190 ' |B| | | | 1 |
13200 ' | | = | P | . | | Y = C / B
13210 ' |C| | | |neta0|
13220 '
13230 ' r = (neta0 - Y) / (neta0 + Y)
13240 '
13250 ' Reflectivity = R = r . r*
13260 '
13270 ' Transmission = T = [neta . (1 - R)] / REAL(B.C*)
13280 '
13290 ' Absorption = A = 1 - R - T
13300 '
13310 a = pr(1,2) + pr(2,2)*netaor - pi(2,2)*netaoi
13320 b = pi(1,2) + pr(2,2)*netaoi + pi(2,2)*netaor
13330 c = pr(1,1) + pr(2,1)*netaor - pi(2,1)*netaoi
13340 d = pi(1,1) + pr(2,1)*netaoi + pi(2,1)*netaor
13350 b = -b
13360 '
13370 GOSUB 14720 : ' Complex Multiply
13380 '
13390 divi = e
13400 b = -b
13410 '
13420 ' Calculate Y
13430 '
13440 GOSUB 14800 : ' Complex Divide
13450 '
13460 a = 1 - e
13470 b = 0 - f
13480 c = 1 + e
13490 d = 0 + f
13500 '
13510 ' Calculate r
13520 '

```

APPENDIX A

```

13530 GOSUB 14800           : ' Complex Divide
13540 '
13550 a = e
13560 b = f
13570 c = e
13580 d = -f
13590 '
13600 ' Calculate R
13610 '
13620 GOSUB 14720           : ' Complex Multiply
13630 '
13640 reflect(i) = e
13650 transmit(i) = netaor*(1 - e)/divi
13660 absorb(i) = 1 - transmit(i) - e
13670 '
13680 ' As well as displaying the results the programme stores
13690 ' the calculated values in three memories given below.
13700 '
13710 PRINT i,wav,0.01/wav,reflect(i),transmit(i),absorb(i)
13720 '
13730 NEXT i
13740 '
13750 GOTO 10730
13760 '
13770 '           S U B R O U T I N E S
13780 '
13790 ' Gaussian
13800 ' This subroutine takes two values plus a mean and
13810 ' standard deviation and calculates the area under a
13820 ' Gaussian curve between the two points. Since the use
13830 ' of a mean and standard deviation normalises the area
13840 ' then the answer is always less than one. This area is
13845 ' then multiplied by the total number of implanted ions
13850 ' and onto this is added the background electron
13860 ' concentration which would lie in that layer. Dividing
13870 ' by the layer thickness gives the electron concentra-

```

## APPENDIX A

```

13875 ' tion and if this is above the cutoff concentration
13880 ' then it is reduced to the cutoff value. Thus this
13890 ' subroutine returns the electron concentration for each
13895 ' input layer.
13900 '
13910 xq = ABS((x1 - mean) / sigma)
13920 tq = 1 / (1 + 0.2316419 * xq)
13930 '
13940 GOSUB 14070
13950 '
13960 q3 = q
13970 xq = ABS((x2 - mean) / sigma)
13980 tq = 1 / (1 + 0.2316419 * xq)
13990 '
14000 GOSUB 14070
14010 '
14020 n = q3 - q
14030 IF x1 - mean < 0 AND x2 - mean > 0
      THEN n = ABS(1 - q3 - q) * ic ELSE n = ABS(n) * ic
14040 n = n / ABS(x2 - x1) + bc
14050 IF n > nc THEN n = nc
14060 RETURN
14070 q = 1 / 2.506628 * EXP(-xq*xq/2)
14080 q = q*tq*(bq1 + tq*(bq2 + tq*(bq3 + tq*(bq4 + tq*bq5))))
14090 RETURN
14100 '
14110 ' Complex Refractive Index n - ik
14120 ' This subroutine takes a value of electron concentra-
14130 ' tion and first calculates the electron mobility and
14135 ' from this the scattering time (theory chapter 2).
14140 ' From this the complex refractive index can be found
14150 ' (theory chapter 2).
14160 '
14170 IF ntemp < 1E+26 THEN mu=(1268/(1+(ntemp/1.3E+23)+0.91))
      +86.5-1.4E-25*ntemp ELSE mu=7.5E+11/SQR(ntemp/1000000)
14180 t = mu * 0.3 * 9.1E-31 / 1.602E-15

```

## APPENDIX A

```
14190 IF scatt <> 0 THEN t = scatt
14200 wp2 = ntemp * 898
14210 wt2 = (w * t)2 + 1
14220 wpt2 = wp2 * t * t
14230 e1 = 11.8 * (1 - wpt2/wt2)
14240 e2 = 11.8 * wp2 * t / w / wt2
14250 e12e22 = SQR(e1*e1 + e2*e2)
14260 nr = SQR((e1 + e12e22)/2)
14270 ni = -SQR(ABS((e12e22 - e1)/2))
14280 RETURN
14290 '
14300 ' Complex Cosine
14310 ' This subroutine takes a complex angle a + ib and
14315 ' returns its cosine.
14320 '
14330 dd = -b
14340 ee = a
14350 '
14360 GOSUB 14840
14370 '
14380 ff = dd
14390 gg = ee
14400 dd = b
14410 ee = -a
14420 '
14430 GOSUB 14840
14440 '
14450 a = (ff + dd) / 2
14460 b = (gg + ee) / 2
14470 RETURN
14480 '
14490 ' Complex Sine
14500 ' This subroutine takes a complex angle a + ib and
14505 ' returns its sine.
14510 '
14520 dd = -b
```

APPENDIX A

```

14530 ee = a
14540 '
14550 GOSUB 14840
14560 '
14570 ff = dd
14580 gg = ee
14590 dd = b
14600 ee = -a
14610 '
14620 GOSUB 14840
14630 '
14640 a = (gg - ee) / 2
14650 b = (dd - ff) / 2
14660 RETURN
14670 '
14680 ' Complex Multiply
14690 ' This subroutine returns the product of two complex
14700 ' numbers. e + if = (a + ib) x (c + id)
14710 '
14720 e = a * c - b * d
14730 f = a * d + b * c
14740 RETURN
14750 '
14760 ' Complex Divide
14770 ' This subroutine returns the quotient of two complex
14780 ' numbers. e + if = (a + ib) / (c + id)
14790 '
14800 e = (a * c + b * d) / (c * c + d * d)
14810 f = (b * c - a * d) / (c * c + d * d)
14820 RETURN
14830 '
14840 cc = EXP(dd) * COS(ee)
14850 ee = EXP(dd) * SIN(ee)
14860 dd = cc
14870 RETURN
14880 '

```

APPENDIX A

```

14890 ' Rear Surface Calculation
14900 ' If the substrate is treated as a final thick film
14910 ' as opposed to an infinite substrate this subroutine
14915 ' calculates the final layer characteristic matrix and
14920 ' then updates the P matrix before setting the
14930 ' refractive index of the infinite substrate to the
14940 ' value for air (if the substrate rear surface is not
14950 ' then the final refractive index is set to that found
14960 ' using the background carrier concentration).
14970 '
14980 deltar = 6.283 * nr * (thick - depth) / wav
14990 deltai = 6.283 * ni * (thick - depth) / wav
15000 netar = nr
15010 netai = ni
15020 a = deltar
15030 b = deltai
15040 '
15050 GOSUB 14330                                : ' Complex Cosine
15060 '
15070 mr(1,1) = a
15080 mr(2,2) = a
15090 mi(1,1) = b
15100 mi(2,2) = b
15110 a = deltar
15120 b = deltai
15130 '
15140 GOSUB 14520                                : ' Complex Sine
15150 '
15160 g = -b
15170 h = a
15180 c = netar
15190 d = netai
15200 a = g
15210 b = h
15220 '
15230 GOSUB 14720                                : ' Complex Multiply

```

## APPENDIX A

```

15240 '
15250 mr(1,2) = e
15260 mi(1,2) = f
15270 '
15280 GOSUB 14800                                : ' Complex Divide
15290 '
15300 mr(2,1) = e
15310 mi(2,1) = f
15315 '
15320 pr(1,1) = qr(1,1)*mr(1,1) - qi(1,1)*mi(1,1) +
           qr(2,1)*mr(1,2) - qi(2,1)*mi(1,2)
15330 pi(1,1) = qr(1,1)*mi(1,1) + qi(1,1)*mr(1,1) +
           qr(2,1)*mi(1,2) + qi(2,1)*mr(1,2)
15340 pr(1,2) = qr(1,2)*mr(1,1) - qi(1,2)*mi(1,1) +
           qr(2,2)*mr(1,2) - qi(2,2)*mi(1,2)
15350 pi(1,2) = qr(1,2)*mi(1,1) + qi(1,2)*mr(1,1) +
           qr(2,2)*mi(1,2) + qi(2,2)*mr(1,2)
15360 pr(2,1) = qr(1,1)*mr(2,1) - qi(1,1)*mi(2,1) +
           qr(2,1)*mr(2,2) - qi(2,1)*mi(2,2)
15370 pi(2,1) = qr(1,1)*mi(2,1) + qi(1,1)*mr(2,1) +
           qr(2,1)*mi(2,2) + qi(2,1)*mr(2,2)
15380 pr(2,2) = qr(1,2)*mr(2,1) - qi(1,2)*mi(2,1) +
           qr(2,2)*mr(2,2) - qi(2,2)*mi(2,2)
15390 pi(2,2) = qr(1,2)*mi(2,1) + qi(1,2)*mr(2,1) +
           qr(2,2)*mi(2,2) + qi(2,2)*mr(2,2)
15400 qr(1,1) = pr(1,1)
15410 qi(1,1) = pi(1,1)
15420 qr(1,2) = pr(1,2)
15430 qi(1,2) = pi(1,2)
15440 qr(2,1) = pr(2,1)
15450 qi(2,1) = pi(2,1)
15460 qr(2,2) = pr(2,2)
15470 qi(2,2) = pi(2,2)
15480 netaor = 1
15490 netaoi = 0
15500 RETURN

```

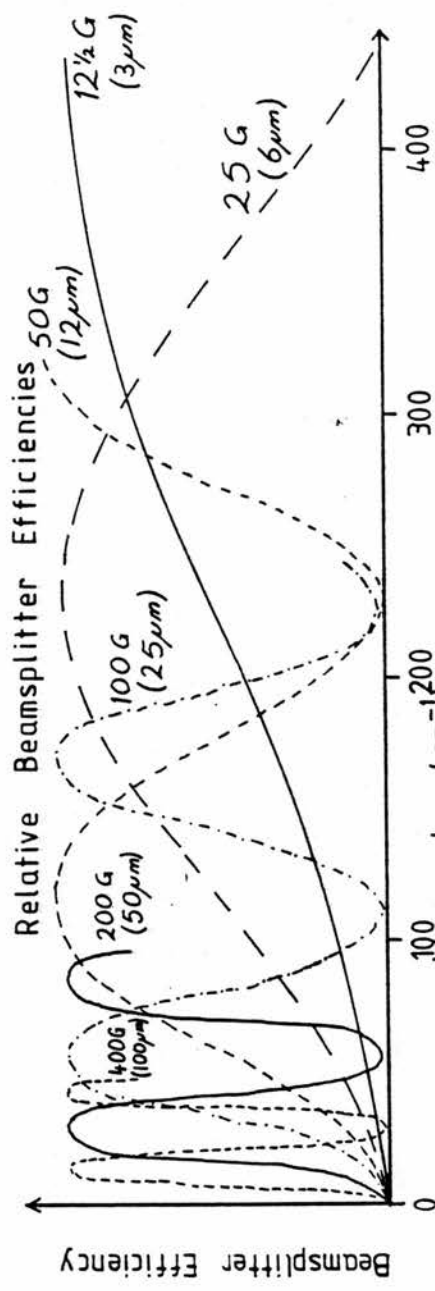
## APPENDIX B

Appendix B

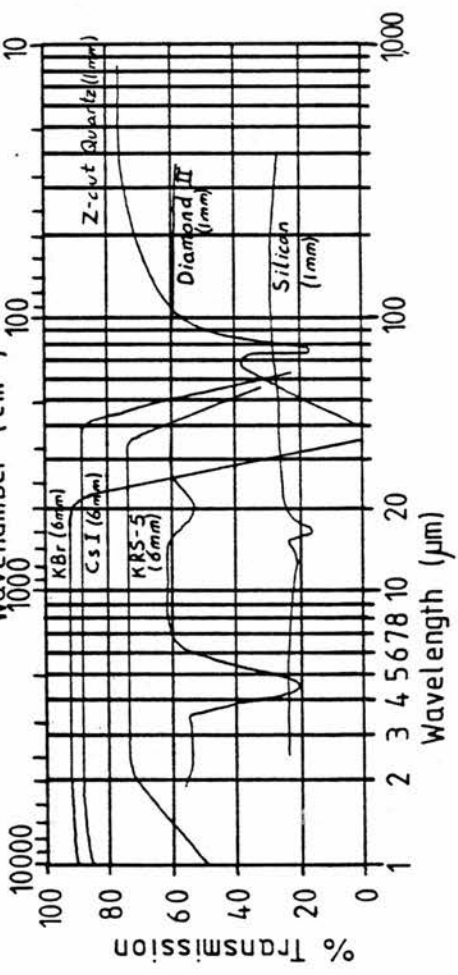
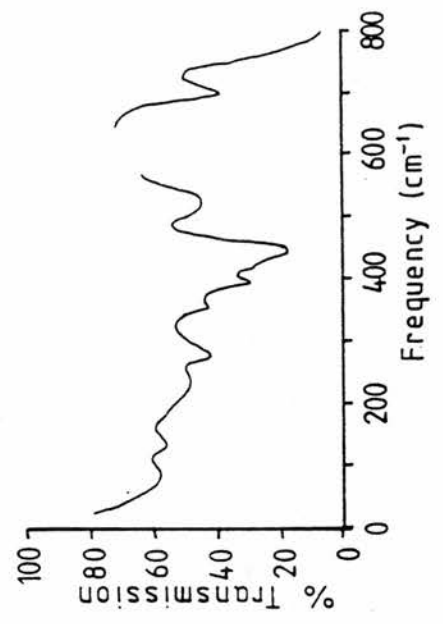
Fourier Transform Spectrometer - The trade offs between Resolution, Mirror Drive Speed, Run Time and system time constant.

Sampling Interval ( $\mu\text{m}$ )	4	8	16	32
Maximum Frequency ( $\text{cm}^{-1}$ )	1250	625	312	156
Resolution ( $\text{cm}^{-1}$ )	2.4	1.2	0.61	0.3
time constant (seconds)	3	3   1	3   1   0.3	3   1   0.3   0.1
512 points run time (minutes)	7.5	15   7.5	30   15   6	60   30   12   6
Drive Speed (In $27.3\mu\text{m}/\text{min}$ )	10	10   20	10   20   50	10   20   50   100
Resolution ( $\text{cm}^{-1}$ )	1.2	0.61	0.3	0.15
time constant (seconds)	3	3   1	3   1   0.3	3   1   0.3   0.1
1024 points run time (minutes)	15	30   15	60   30   12	120   60   24   12
Drive Speed (In $27.3\mu\text{m}/\text{min}$ )	10	10   20	10   20   50	10   20   50   100
Resolution ( $\text{cm}^{-1}$ )	0.61	0.3	0.15	0.08
time constant (seconds)	3	3   1	3   1   0.3	3   1   0.3   0.1
2048 points run time (minutes)	30	60   30	120   60   24	240   120   60   24
Drive Speed (In $27.3\mu\text{m}/\text{min}$ )	10	10   20	10   20   50	10   20   50   100
Resolution ( $\text{cm}^{-1}$ )	0.3	0.15	0.08	0.04
time constant (seconds)	3	3   1	3   1   0.3	3   1   0.3   0.1
4096 points run time (minutes)	60	120   60	240   120   48	480   240   96   48
Drive Speed (In $27.3\mu\text{m}/\text{min}$ )	10	10   20	10   20   50	10   20   50   100

# APPENDIX B

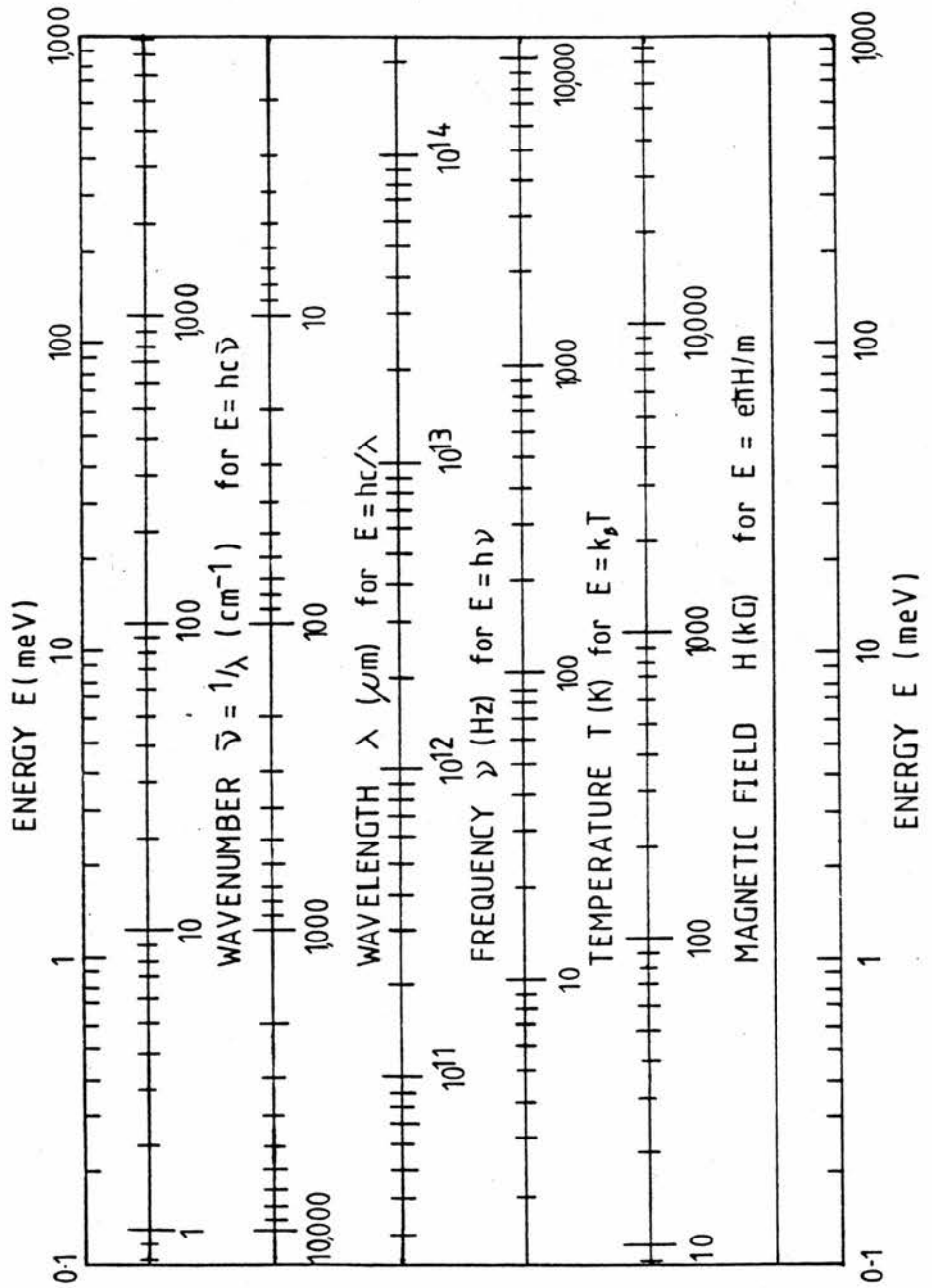


Far-infrared Absorption Spectrum of TPX. [34]



Window Transmission Characteristics

APPENDIX C — Conversions



## APPENDIX D

Appendix DLevel Crossing Section - Sample Data

Sample	Source	$N_D - N_A$ (77K) $\text{cm}^{-3}$	Mobility (77K) $\text{cm} / \text{Vsec}$	$N_A/N$
	Wright-			
R-137	Patterson (VPE)	$1 \times 10^{13}$	160,000	--
	Wright-			
RR98B	Patterson (VPE)	$2 \times 10^{14}$	163,000	0.05
	Motorola			
S1	(VPE)	$5 \times 10^{13}$	160,000	--